1290

UNIVERSIDADE DE
COIMBRA

Fátima Sofia Monteiro Alcaso

Optimisation of a Xenon Time Projection Chamber for Studies of Neutrinoless Double Beta Decay in ^{136}Xe

Dissertação no âmbito do Mestrado Integrado em Engenharia Física,
no Ramo de Instrumentação, orientada pelo Professor Doutor Alexandre Miguel
Ferreira Lindote e pelo Professor Doutor Francisco Filipe Bento Neves e
apresentada ao Departamento de Física da Faculdade de Ciências e Tecnologia
da Universidade de Coimbra.

Setembro de 2022

FACULDADE DE
CIÊNCIAS E TECNOLOGIA
UNIVERSIDADE DE
COIMBRA

Engineering Physics Masters in Instrumentation

Optimisation of a Xenon Time Projection Chamber for Studies of Neutrinoless Double Beta Decay in ^{136}Xe

Fátima Sofia Monteiro Alcaso

Supervisor
Alexandre Miguel Ferreira Lindote (LIP-Coimbra)

Supervisor
Francisco Filipe Bento Neves (LIP-Coimbra)

This work was developed in collaboration with:

Faculdade de Ciências e Tecnologia da Universidade de Coimbra

Laboratório de Instrumentação e Física Experimental de Partículas

Imperial College of London

Esta versão inclui as revisões e sugestões feitas pelo Júri.
This version includes the reviews and suggestions done by the Jury.

Dedication

To my mum, dad and brother, my biggest supporters.

Acknowledgments

A huge thank you to my supervisors, the Doctors Alexandre Lindote and Francisco Neves, for guiding me through the highs and lows of this work and for your patience. It has been a pleasure to be your student ever since my first internship up to this moment, you inspire me to grow as a scientist.

To all the members of the LIP Dark Matter Group, thank you for welcoming me so warmly. I appreciate all the conversations we shared in the office about science, as well as the laughs and stories told over a couple of drinks. A special thanks to Doctor Isabel Lopes, for giving me the opportunity to work and learn with the group in my first year of university, for the encouragement on my academic endeavours and for the valuable advices.

I would also like to extend my thanks to Researchers Andrey Morozov and Vladimir Solovov for all the help you provided while working with ANTS2. A big thanks to Doctor Henrique Araújo and the members of the Imperial group for allowing me to contribute to the Xenia project.

To my oldest friends, Pedro, Raquel and Daniela, my life would not be as rich and colourful without you, the long years of our friendship mean the world to me. To my university family, especially Shea, Ricardo and Catarina, I did not expect to create such beautiful bonds in a short amount of time, thank you for the fun adventures. A very special thank you to Manuel, for your love and unwavering support.

To my buddy Joando for the long study sessions filled with humour, as well as Paulo and Sandro, for the insightful conversations and all the jokes.

The biggest and most sincere gratitude goes out to my closest family members for pushing me forward during my academic journey, for believing in me even when I struggled to believe in myself. To my parents, who will always inspire me and to whom I am forever grateful for my upbringing. To my brother, who I love growing up with. And finally, to my grandparents, from high above the stars or from Earth, I love and miss your hugs accompanied by pastéis de nata.

Per aspera ad astra!

Sumário

As propriedades e natureza dos neutrinos têm alimentado a curiosidade científica durante anos, especialmente desde a observação do fenómeno de oscilação de neutrinos que provou que estes possuem massa. Esta descoberta, em conjunto com outras, motivou o aprofundamento da investigação sobre este tema e a possibilidade de os neutrinos serem fermiões do tipo Majorana. O decaimento duplo beta sem neutrinos é um dos processos hipotéticos através dos quais é possível explorar este problema, já que a observação deste decaimento significaria que existe violação da conservação de de leis fundamentais da física de partículas.
À medida que as experiências de matéria escura que utilizam Xénon líquido evoluem e se tornam mais sensíveis, surge a oportunidade de estudar outros fenómenos físicos raros. A experiência LUX-ZEPLIN é a maior câmara de projeção temporal alguma vez construída, contendo 10 toneladas de Xénon natural, tornando-a uma excelente candidata para o estudo do decaimento beta duplo sem neutrinos no ^{136}Xe. No entanto, as experiências de Xénon líquido atualmente em curso não foram otimizadas para detetar estes decaimentos, visto que estas são desenhadas para procurar candidatos à matéria escura como os WIMPs (partículas massivas de interação fraca), os quais se espera que produzam interações de baixa energia, ao contrário da energia da ordem dos MeV esperados para o decaimento sem neutrinos.

Durante esta tese foram estudadas as propriedades dos neutrinos, a física e a importância inerente ao decaimento duplo beta sem neutrinos, bem como os requisitos experimentais para diferentes formas de deteção. Aprofundaram-se os conhecimentos sobre a especificidade das câmaras de projeção temporal, o seu princípio de funcionamento e como o seu design e tecnologia pode ser melhorado para reconstruir a energia e a posição de decaimentos raros. O decaímento sem neutrinos deixa um rastro de aproximadamente 1.5 mm de comprimento no ^{136}Xe com duas zonas de alta densidade de deposição energética em cada extremidade do trajeto, e de forma a ser possível distinguir um sinal de um evento de fundo, um requerimento chave é atingir uma resolução espacial próxima de 100 μm. Um novo protótipo desenvolvido para detetores futuros é apresentado sob o nome de Xenia, e demonstramos a optimização do seu design de modo a atingir $\sim$124 μm de resolução espacial para uma energia de Q = 2.458 MeV, correspondente ao decaimento duplo beta sem neutrinos no ^{136}Xe. Finalmente, descrevemos o funcionamento de uma ferramenta de simulação desenvolvida para estudar a resposta do detetor Xenia a interações, e demonstramos a sua viabilidade com exemplos de eventos simulados.

Palavras-Chave: Câmara de Projeção Temporal, Xénon, Decaimento Beta Duplo Sem Neutrinos, Eventos Raros, Fotomultiplicadores de Silício

Abstract

The properties and nature of neutrinos have fueled scientific curiosity for years, especially since the observation of neutrino oscillations proved that neutrinos have mass. This discovery, along with others, motivated further research on this subject and the possibility that neutrinos could be Majorana fermions. Neutrinoless double beta decay is one hypothetical process by which it is possible to explore this problem since its observation would signify the non-conservation of fundamental laws in particle physics.
As liquid Xenon (LXe) experiments for dark matter searches evolve and become more sensitive, with it comes the opportunity to study other rare physics phenomena. The LUX-ZEPLIN experiment is the largest time projection chamber (TPC) ever built, housing 10 tonnes of natural Xenon, hence making it a great candidate to study neutrinoless double beta decay in ^{136}Xe. However, current LXe experiments are not optimised to detect such decays as they are designed to search for dark matter candidates such as WIMPs (weakly interacting massive particles), which are expected to produce low energy interactions, contrasted by the MeV energy range of the neutrinoless decay.

In the work presented in this dissertation, neutrino properties, the physics and importance behind neutrinoless double beta decay were studied, along with the experimental requirements for different detection options. We delve into the specifics of LXe TPCs, their working principle and how its design and technology can be elevated to reconstruct energy and position of rare decays. The neutrinoless decay leaves a track of approximately 1.5 mm in length in ^{136}Xe with two high density energy deposition spots at each end of the path, and in order to distinguish a signal from a background event, a key requirement is to achieve a spatial resolution close to 100 μm. A newly developed prototype for future detectors is presented under the name of Xenia, and we demonstrate the optimisation of its design to reach $\sim$124 μm spatial resolution at a Q-value = 2.458 MeV for the neutrinoless double beta decay in ^{136}Xe. Finally, we describe the operation of a simulation tool developed to study the detector response of Xenia to interactions, and demonstrate its feasibility with examples of simulated events.

Keywords: Time Projection Chamber, Xenon, Neutrinoless Double Beta Decay, Rare Events, Silicon Photomultipliers

Acronyms

CKM Cabibbo–Kobayashi–Maskawa

CMB Cosmic Microwave Background

DBD Double Beta Decay

DR Drift Region

ER Electron Recoils

IH Inverted Hierarchy

LCE Light Collection Efficiency

LXe Liquid Xenon

MWPC Multi-Wire Proportional Counter

NH Normal Hierarchy

NR Nuclear Recoils

PMNS Pontecorvo-Maki-Nakagawa-Sakata

PSP Phase-Space Factor

SiPM Silicon Photomultiplier

TPC Time Projection Chamber

WIMP Weakly Interacting Massive Particle

CL Confidence Level

CνB Cosmic Neutrino Background

DM Dark Matter

ELR Electroluminescence Region

GXe Gaseous Xenon

ISW Integrated Sachs-Wolfe

LS Liquid Scintillator

LZ LUX-ZEPLIN

NDBD Neutrinoless Double Beta Decay

NME Nuclear Matrix Element

PDE Photon Detection Efficiency

PM Photomultiplier

ROI Region of Interest

SM Standard Model

V-A Vector minus Axial vector

LET Linear Energy Transfer

Contents

“Science makes people reach selflessly for truth and objectivity; it teaches people to accept reality, with wonder and admiration, not to mention the deep awe and joy that the natural order of things brings to the true scientist.”

- ELISE MEITNER (NOVEMBER 7, 1878 – OCTOBER 27, 1968)

Chapter 1

Introduction

1.1 Motivation and Objectives

This work is part of a wider R&D study for the next generation of dark matter detectors which plan to become competitive in the study of other rare physics processes. The 3^{rd} generation of detectors will join several current experiments such as LUX-ZEPLIN, DARWIN and XENONnT in a larger collaboration with the aim to improve the technology currently being used in two-phase xenon (liquid-LXe and gas-GXe) time projection chambers (TPCs) and possibly implement these changes in future detectors to improve their sensitivity to study neutrino properties and rare decays such as neutrinoless double beta decay ($0\nu\beta\beta$).

Double beta decay ($2\nu\beta\beta$) is a process that has been observed in various isotopes (including ^{136}Xe) and by which the nucleus emits two electrons and two electron antineutrinos. This is distinct from the neutrinoless decay which is an hypothesised process by which a nucleus emits two electrons but no neutrinos; this would only be possible if the neutrino is revealed to be its own antiparticle (Majorana particle) and its observation would break the conservation of baryonic and leptonic number symmetry, implying new physics beyond the Standard Model. The study of neutrinoless double beta decay can be used to delve into the fundamental nature of neutrinos, their mass scale and mass hierarchy. Moreover, the observation of this decay could help explain the matter-antimatter asymmetry observed in the Universe, which would change our understanding of the subatomic world.

In order to study these rare processes, we need to improve the performance of this type of detectors at MeV energies, namely the spatial resolution which is crucial to resolve two electron events. This can be done by exploring some new techniques with a prototype detector, such as: introducing a new chamber with H_2-doped xenon, installation of a VUV SiPM (silicon photomultipliers for detection of visible ultra-violet light) array with with the frontend electronics installed inside the TPC, installation of a collimator for better positional resolution and development of a tailored data acquisition system.

The main goal of this thesis is to design, simulate and optimise a prototype LXe TPC to be used in R&D studies intended to maximise the sensitivity to $0\nu\beta\beta$ in ^{136}Xe for this type of detectors. The chamber design is required to be optimised for an energy of $Q_{\beta\beta} = 2.458$ MeV, position resolution of ~ 100 μm and low radioactivity levels per unit readout area ($\sim$ mBq). This encompasses characterisation of the prototype through simulations, evaluation of VUV SiPM behaviour, using digitised time resolved signals from photosensors to obtain light maps and perform energy and position reconstruction of events in the region of interest. These studies should be supported by Geant4 and ANTS2 for simulation and calibrations.

Outside the scope of this work, but still included in the long term goals for this project are event topology studies, exploring Machine Learning techniques for position reconstruction and to discriminate signal/background events and simulation of internal and external calibration sources. After the prototype is ready to begin acquiring data, it will also be necessary to analyse the behaviour of electrical components under cryostatic conditions, study correlated noise in SiPM (afterpulsing, optical cross talk, cryogenic noise) and there are also plans for detecting the fast Cherenkov ring in LXe for additional discrimination power.

This project is being developed within the Laboratory of Instrumentation and Experimental Particle Physics (LIP) research group in the University of Coimbra, in collaboration with the Imperial College of London. The design and simulations for the prototype were done in LIP-Coimbra and the construction and operation will take place in the laboratories at Imperial.

1.2 Structure of this document

This dissertation is organised as follows.

Chapter 2 begins with a brief history of neutrinos since their discovery until the present day, followed by a breakdown of different neutrino sources and description of neutrino properties such as helicity, chirality, symmetries, flavour oscillations and mass hierarchy. Double beta decay and the neutrinoless decay possibility are discussed in detail as well as the importance and implications of its discovery in the Standard Model.

Chapter 3 delves into the main characteristics to consider when designing an experiment to detect NDBD, namely the signature of the event, sensitivity parameters and detection techniques, followed by an overview of several state of the art experiments on this subject.

Chapter 4 opens with a summary of time projection chambers and the remainder of the chapter focuses on the characteristics of the prototype dual-phase liquid xenon TPC that is being developed and constructed at Imperial. An overview of the detector components is given, along with a description of xenon properties and an explanation of the working principle and relevant physical variables.

Chapter 5 introduces the Xenia prototype in the context of the next generation of detectors, by identifying its key features (silicon photomultipliers, collimator and xenon-doping) and portraying how this was implemented in the simulation. The overall simulation strategy and software tools used are also introduced here.

The details of the optical optimisation simulation for improved position reconstruction are given in Chapter 6 along with the results and discussion.

The inner workings of the end-to-end tool developed to simulate events of interest in Xenia are explained in detail in Chapter 7, along with some examples of simulated waveforms.

Final conclusions are presented in Chapter 8.

Chapter 2

Neutrinos

> "The neutrino – if there was one particle that was going to break the rules it was this one."
>
> *Professor Marcus du Sautoy*

For several years, studies on beta decay suggested that the sum of the energy of the recoiling nucleus and the emitted electron was lower than the one of the initial nucleus, implying that this radioactive decay violated the principle of conservation of energy. This gave rise to many queries among physicists; it could either mean that the theory was flawed and adjustments had to be made to account for these findings, or that there could be something missing experimentally to align with the theory. While Niels Bohr proposed a statistical version of the conservation laws to justify the experimental data, in 1930 Wolfgang Pauli proposed the existence of the *neutrino*. This tiny, electrically neutral particle could carry the missing energy in the decay, restoring the conservation principle [Lan13].

The existence of the electron neutrino (ν_e) in beta decay[1] was experimentally confirmed in 1956 by Cowan and Reines [Cow+56] within the scope of Project Poltergeist. Since then, the discovery of the muon neutrino (ν_μ) followed in 1962 with the efforts of Lederman, Schwartz and Steinberger [Dan+62], which earned them the 1988 Nobel Prize. Later recognition was also given to Reines for the first neutrino detection when he was awarded the 1995 Nobel Prize[2]. Finally, the neutrino sector was completed when the tau neutrino (ν_τ) was detected by the DONUT collaboration in the year 2000 [Kod+01].

Today, the Standard Model of Particle Physics comprises six leptons, divided in three generations (Table 2.1). Neutrinos are part of this lepton family, and each neutrino flavour is named after the subatomic particle it is most likely to interact with: electron, muon or tau [AH02].

Table 2.1: Lepton sector of the SM, showing the division of the three generations and their respective electromagnetic charge (Q) and colour charge (C).

1^{st}	2^{nd}	3^{rd}	Q	C
e^-	μ^-	τ^-	-1	none
ν_e	ν_μ	ν_τ	0	none

---

[1] At this point in time, there was still no distinction between the neutrino and antineutrino.

[2] Unfortunately Cowan passed away years prior and so could not share the award.

Albeit exceptionally small, neutrinos were proven to have mass through the observation of their oscillations between flavours, having an upper mass limit of $m_\nu = \sum_i m_{\nu_i} < 0.120$ eV (with 95% C.L.)[3] [Mer16]. They are about six orders of magnitude lighter than the electron, the next lightest particle. They are also the only type of fermion to not possess electromagnetic charge (Q) or colour charge (C), meaning they do not participate in the electromagnetic and strong interactions, nor do they interact with the Higgs field (Table 2.1). Interaction through the weak force (and gravitational force as well - hypothetical *sterile neutrinos*), makes these fleeting particles notoriously difficult to detect[4], thus they have intrigued scientists for decades.

Unlike all other known particles, their characteristics hint at the possibility that neutrinos could be Majorana fermions. This refers to a fermion which is its own antiparticle, and such discovery would have a serious impact in our understanding of nature (see Figure 2.1).
One of the few ways scientists can test this Majorana hypothesis is by searching for processes which do not obey conservation laws. The most sensitive probe for this purpose is studying neutrinoless double beta decay ($0\nu\beta\beta$ or NDBD) - a decay in which two neutrons in a nucleus simultaneously transform into protons, releasing two electrons but without the emission of antineutrinos. This hypothetical process is forbidden by the formulations of the Standard Model (SM), as the difference between baryonic and leptonic number (B-L) is a known fundamental symmetry [Car18], and it is violated by two units in this decay. Observing lepton number violation could confirm the Majorana nature of neutrinos, and would imply their masses are possibly a consequence of a new fundamental energy scale in physics [Gou+13]. Although the neutrino mass scale is still unknown, establishing the absolute value of neutrino masses is a crucial step towards understanding their mass generation mechanism [Mer16].

The study of the nature and properties of neutrinos, such as their mass generation mechanism, mass hierarchy, magnetic moment and oscillation parameters, is a thriving field of study with many on-going dedicated experiments, as it presents an opportunity to study new physics beyond the SM. Current experiments are focused on testing the three-flavour paradigm with precision neutrino oscillation experiments, searching for neutrinoless double beta decay and finding the absolute values of the neutrino masses [Gou+13].

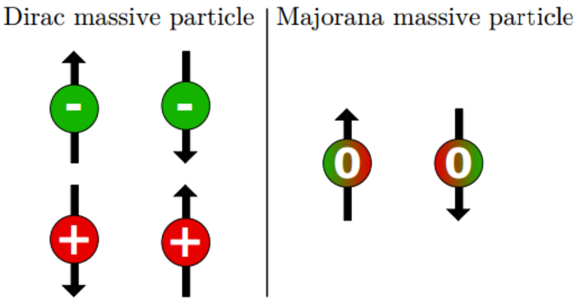

Figure 2.1: On the left, the 4 states of the Dirac massive field are represented: the arrows indicate the possible directions of spin and the charges distinguish particles from antiparticles. On the right, the 2 states of the Majorana massive field: there are two directions of spin and no electromagnetic charge, meaning particles and antiparticles coincide. Figure from [Del+16].

---

[3] This value was obtained from limits based on a combination of cosmological probes [Pal+15].

[4] It would take a lead wall with a thickness of about 2 light-years to stop a beam of neutrinos!

2.1 Neutrino Physics

2.1.1 Sources of neutrinos

Besides only being able to interact via the weak nuclear force and gravitational force, neutrinos have a small cross section, which makes their detection a difficult feat. These elusive particles haul important information on the astrophysical objects which produced them, and their study is possible thanks to sources that guarantee a high incoming flux of these particles. Figure 2.2 illustrates some of these sources which give off neutrinos with energies ranging over 20 orders of magnitude, including a list of experiments that aim to detect each of these neutrino types.

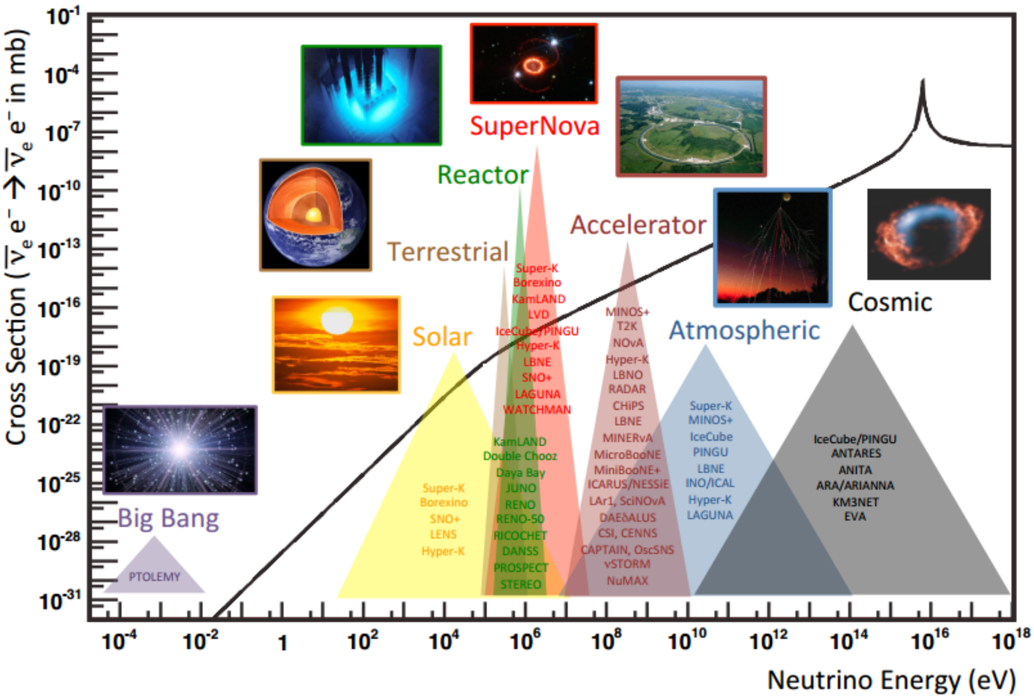

Figure 2.2: Neutrino-electron scatter cross section as a function of the neutrino energy. The graph also depicts various neutrino emitters and a number of experiments for each emitter which aim to study the neutrinos within a determined energy range. Figure from [Gou+13].

Big Bang

Cosmology models predict that neutrinos were created in abundance just after the Big Bang. Only one second afterward, the temperature had lowered enough for the weak force to lose strength and allow neutrinos to escape absorption by matter. The cosmic neutrino background ($C\nu B$) is the result of this decoupling of neutrinos from matter. They are also known as *relic neutrinos* because they act as a fingerprint: the remains of the first moments after the Big Bang which are still travelling through the cosmos today, just like the Cosmic Microwave Background (CMB) [Kut03] [Giu+14]. Figure 2.3 illustrates the timeline of appearance of these backgrounds.

These neutrinos are estimated to currently have a thermal energy of 1.7×10^{-5} eV ($T_\nu = 1.95$ K) as a result of the expansion and cooling of the Universe [Gou+13]. Although there is an abundance of them, detection of these thermal neutrinos is even more challenging than their higher energy counterparts (up to the PeV range). At the moment there is only indirect evidence from cosmological observables to support the theory behind relic neutrinos. Experiments that have performed precision measurements of the relic abundances of light elements indicate the

number of degrees of freedom should include not only photons, but also an additional three, consistent with the three neutrino species [Gou+13] [Aba+15].
Observation of $C\nu B$ would be a major milestone as it would give us a glimpse of the first second after the Big Bang, it could provide important information on primordial nucleosynthesis, anisotropies of the CMB[5] and on the nature of neutrinos themselves [Gou+13]. Several methods have been proposed to this end, but the most promising one is neutrino capture on a β-decaying nucleus. This is the strategy behind the PTOLEMY project (PonTecorvo Observatory for Light Early-universe Massive neutrino Yield), whose primary goal is the detection of relic neutrinos, as well as the direct search for neutrino masses [Bet+13] [Bar+18].

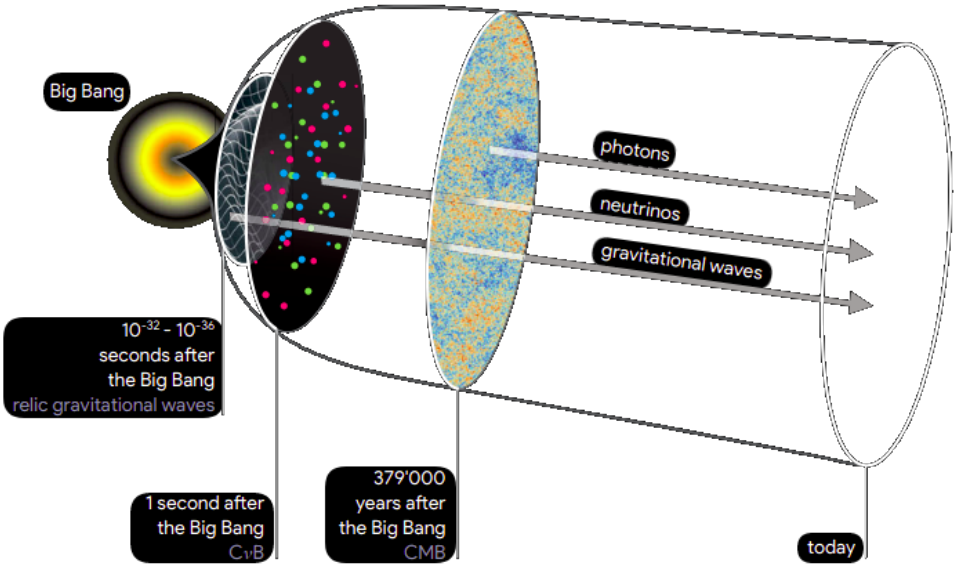

Figure 2.3: Representation of the first moments after the Big Bang. Around 10^{-32} - 10^{-36} seconds, relic gravitational waves spread through the cosmos, and 1 second after, neutrinos decouple from matter forming the CνB. About $\sim 380,000$ years later is the time of last scattering, when the temperature had decreased enough to allow the formation of hydrogen atoms, making the universe nearly transparent to radiation, known today as the CMB. Figure adapted from [Fis12].

Solar

For a detector placed on Earth, the most prominent and continuous source of neutrinos is our Sun. The integrity and structure of stars is maintained by the fusion reactions at its core, where 4 protons are converted into a ^4He nucleus through the proton-proton chain (*pp chain*) (for stars of mass $< 1.3\ M_{\odot}$[6]) or the Carbon-Nitrogen-Oxygen cycle (*CNO cycle*) (dominant in stars with $> 1.3\ M_{\odot}$), which are summarized in Table 2.2. Subsequently the fusion process continues to get increasingly more complex as the star fuses heavier elements. During these series of fusion reactions, positrons, gamma-rays and neutrinos carry away the energy produced. While the other particles are responsible for heating the gas, the photons suffer absorption and re-

---

[5] By considering neutrinos a component of cold dark matter, their mass would influence early structure formation. At the time of decoupling, neutrinos are relativistic hence repressing the formation of structures at small scales [Gou+13]. The biggest influence on the CMB caused by neutrino masses is due to the early Integrated Sachs-Wolfe effect (ISW) [Giu+14]. This is a process in which photons from the CMB interact with a gravitational field with density fluctuations, causing them to be redshifted, creating uneven areas in the spectrum [Wri07].

[6] $M_{\odot}$ represents the mass of the Sun.

emission repeatedly[7], and the neutrinos escape the star completely [Kut03].

Table 2.2: Solar fusion cycle according to the Standard Solar Model and typical neutrino energies for each reaction [Cle+98].

Reaction	Timescale	E_ν (MeV)
Proton-proton Chain:		
Phase I		
(pp) $p + p \to d + e^+ + \nu_e$	10^{10} years	≤ 0.42
(pep) $p + e^- + p \to d + \nu_e$	-	1.442
$p + d \to^3 He + \gamma$	1 second	-
$^3He +^3 He \to^4 He + 2p$	10^5 years	-
(hep) $^3He + p \to^4 He + e^+ + \nu_e$	-	≤ 18.8
Phase II		
$^3He +^4 He \to^7 Be + \gamma$	10^6 years	-
$^7Be + e^- \to^7 Li + \nu_e$	0.3 years	0.861
$^7Li + p \to^4 He +^4 He$	90 years	-
Phase III		
$^3He +^4 He \to^7 Be + \gamma$	10^6 years	-
$^7Be + p \to^8 B + \gamma$	90 years	-
$^8B \to^8 Be * +e^+ + \nu_e$	10^{-8} seconds	≤ 15
$^8Be^* \to^4 He +^4 He + \gamma$	10^{-16} seconds	-
Carbon-Nitrogen-Oxygen Cycle:		
$p +^{12} C \to^{13} N + \gamma$	-	-
$^{13}N \to^{13} C + e^+ + \nu_e$	-	≤ 1.20
$p +^{13} C \to^{14} N + \gamma$	-	-
$p +^{14} N \to^{15} O + \gamma$	-	-
$^{15}O \to^{15} N + e^+ + \nu_e$	-	≤ 1.73
$p +^{15} N \to^{12} C +^4 He$	-	-

Neutrinos are a gateway to look into the solar core as they are the only particles capable of traversing through all layers of the Sun, reaching us about 8.5 minutes after their creation. The proximity of the Earth relative to the Sun and the fact that neutrinos account for 2% of the total solar energy output, contribute to a high flux of these particles and offer a perfect opportunity to test the accuracy of stellar models. Figure 2.4 illustrates the energy spectrum of solar neutrinos.

The first solar neutrino experiment was carried out by R. Davis between 1967 and 1994 [Cle+98] with the goal of measuring the flux of neutrinos passing through Earth and comparing it to the theoretical rate predicted by solar models. This was achieved by shielding a tank underground at the Homestake Gold Mine, and filling it with 615 tonnes of tetrachloroethylene (C_2Cl_4). The neutrinos created from ^8B decay could be absorbed by the ^{37}Cl atoms present in the liquid, transforming some into radioactive isotopes of Argon, which would subsequently be collected [DP18]. The reaction is an inverse β-capture, given by Equation (2.1).

$$^{37}Cl + \nu_e \to^{37} Ar + e^- \tag{2.1}$$

This experiment, along with Kamiokande (1987)[Hir+87a], published identical results in regards to the rate of solar neutrino interactions, agreeing on 2.55 ± 0.25 SNU[8]. The predicted

---

[7] Their energy can take up to 10^7 years to reach the surface of the star.

[8] Solar Neutrino Units - one neutrino interaction per second for every 10^{36} atoms.

values by theorists were higher, pointing to 8.5 ± 1.8 SNU, which became known as the *solar neutrino problem* [Lan13]. This inconsistency was settled in 2001, after the SNO (Sudbury Neutrino Observatory) experiment showed strong evidence that neutrinos can change flavours [Ahm+02]. This is further explained in Subsection 2.1.5.

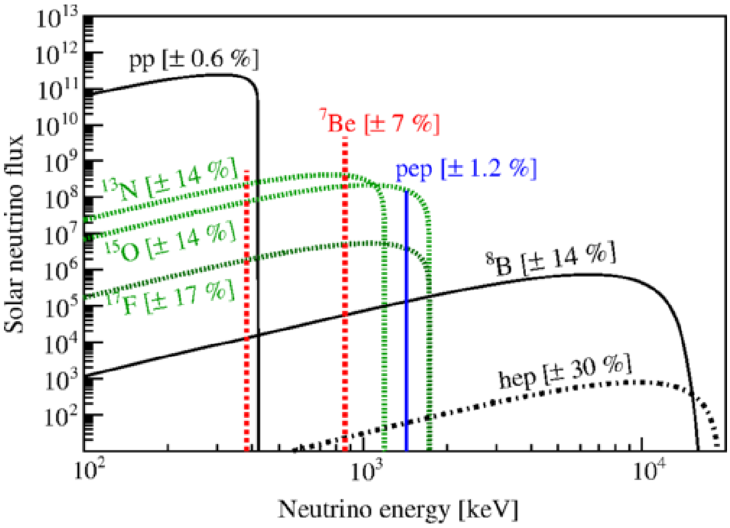

Figure 2.4: Solar neutrino flux as function of neutrino energy. The flux in the vertical axis is defined in $\mathrm{cm}^{-2}\ \mathrm{s}^{-1}(10^3\ \mathrm{keV})^{-1}$ for the continuous spectra, and in $\mathrm{cm}^{-2}\ \mathrm{s}^{-1}$ for the mono-chromatic lines [Bel+14]. Even though the neutrino flux from *hep*, ^8B and *pep* reactions is evidently lower than the ones created in the *pp chain*, the higher energies up to tens of MeV makes their detection easier.

An experiment that has been focused on studying neutrinos from the Sun as well as from other astrophysical sources is Borexino [Ali+09]. It is a low background, large liquid scintillator detector, and was initially designed to perform solar neutrino spectroscopy, but over the years it has accomplished other relevant studies. Namely, they reported the first direct observation of neutrinos produced by the CNO cycle in the Sun and quantified the contibution of CNO fusion to be about 1% [Col20].

Supernovae

A supernova forms when a massive star can no longer fuse light elements, causing an imbalance between the inward gravitational force and the outward pressure from thermonuclear fusion.
When all of the mass in the stellar core is converted to stable heavy elements (^{56}Fe and ^{59}Ni), fusion ceases to occur, the temperature decreases, and the thermal pressure is no longer sufficient to support the core. The core then collapses, releasing gravitational potential energy which is used up in reactions with iron and nickel. The protons released in this process can combine with electrons ($p + e^- \to n + \nu_e$) to form neutrons and neutrinos. The core quickly becomes very dense, culminating in an explosion, where even heavier elements are created and the shock wave spreads out material into interstellar space [Lan13].
This is one of the most highly energetic events in the Universe, in which 99% of the emitted energy is released in the form of neutrinos and antineutrinos, escaping almost unimpeded from the core, with energies spanning over a few tens of MeV [Sch12].

The first strong evidence to support the theory of supernova collapse arose in 1987, when a number of observatories, including Kamiokande-II, reported an excess of neutrino interactions over a 13 second time interval. This became known as the SN1987A event, which was confirmed to be a neutrino burst from a supernova in the Large Magellanic Cloud and demonstrated the baseline model of core collapse [Hir+87b]. However, since the rate of core collapse supernovae is estimated to be a few per century, it is more efficient to also investigate events that provide a regular, low signal, such as supernova relic neutrinos which provide a higher rate of events in the long term (∼10 events per kilotonne per year) [Sch12]. The newer Super-Kamiokande experiment is a large water Cherenkov detector which was built to observe astrophysical, atmospheric and anthropogenic neutrinos. This collaboration has achieved the best sensitivity to the diffuse supernova neutrino background (DSNB) and set the most stringent upper limit on extraterrestrial $\overline{\nu}$ flux, for energies below 31.3 MeV [Abe+21].

Atmospheric

Our atmosphere is constantly being hit by high energy cosmic rays (from a few GeV up to hundreds of PeV) which produce mesons, and through subsequent interactions create showers of unstable secondary particles such as pions, kaons and muons. During their path towards the surface, they leave behind a trail of α and β particles, as well as ν and $\overline{\nu}$. These neutrinos cover a wide range of energies from 100 MeV to over 100 GeV, and travel distances from tens to thousands of kilometres before their detection [Gou+13]. The most common production mechanisms for atmospheric neutrinos [DP18] are described through Equation (2.2) and illustrated in Figure 2.5.

$$\begin{aligned} \pi^{\pm} &\rightarrow \mu^{\pm} + \nu_{\mu}(\overline{\nu}_{\mu}) \\ \mu^{\pm} &\rightarrow e^{\pm} + \nu_{e}(\overline{\nu}_{e}) + \overline{\nu}_{\mu}(\nu_{\mu}) \end{aligned} \tag{2.2}$$

According to this, each pion decay produces two muon antineutrinos and one electron antineutrino, so one would expect to have a flux of muon neutrinos which is double the one of electron neutrinos, but this does not correspond to the findings taken from experimental observations, where they found a deficit of muon neutrinos. This *atmospheric neutrino anomaly* was cleared up by the Super-Kamiokande experiment, in which they measured the ratio of neutrinos coming from the top and bottom of the detector. They concluded that the anomaly was due to the fact that neutrinos produced in particle showers on the other side of the Earth need to travel through $\sim 1.3 \times 10^{4}$ km of matter, making it more likely for a large flavour mixing to occur; in contrast to the neutrinos produced above the detector which do not cover a large enough distance to manifest oscillations [Fuk+98a].

The first measurement of the atmospheric muon neutrino spectrum at high energies (100 GeV to 400 TeV) was performed by the IceCube observatory in 2010 [Abb+11]. This experiment makes use of one cubic kilometre of Antarctic ice as a Cherenkov detector to probe the most violent astrophysical events in an attempt to provide answers on dark-matter, sterile neutrinos and neutrino properties. They have also detected anisotropies in the arrival directions of atmospheric muons [Abb+10], and in collaboration with several other observatories, made the first identification of a source of extragalactic neutrinos [Aar+18].

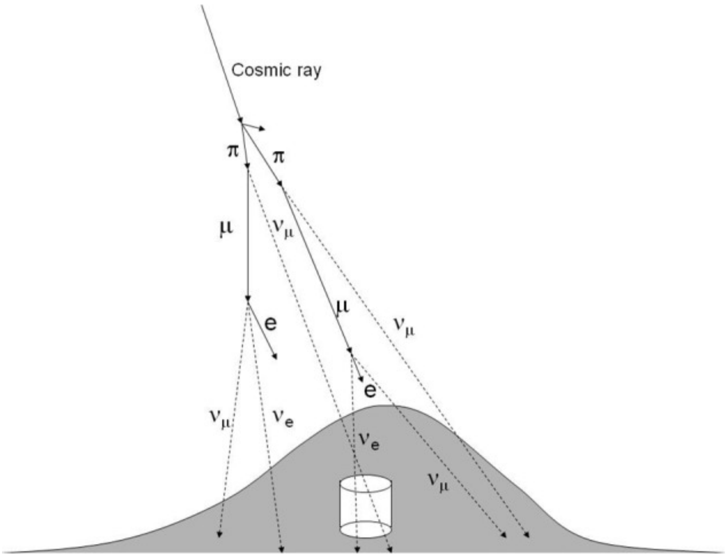

Figure 2.5: Illustration of the most common processes responsible for production of neutrinos in the atmosphere. The cylinder represents an underground detector. Figure from [KAJ10].

Geological

Geoneutrinos are a product of the natural radioactivity of Earth, and their energy ranges between $10^5 < E_{\nu\ geo} < 5 \times 10^6$ MeV (Figure 2.2). Uranium-238, Thorium-232 and Potassium-40 are among the most abundant elements which undergo β decay, producing antineutrinos. The levels of geoneutrinos carry valuable information about the abundances of these elements, radiogenic heat and the geodynamics inside our planet. Experiments like Borexino, KamLAND, SNO+ and Hanohano have contributed to test models of the Earth by predicting geoneutrino interactions in the crust and mantle and by measuring neutrino flux and spectral information [Dye+14].

Artificial Sources

Neutrinos can also originate in anthropogenic sources such as particle accelerators, reactors and nuclear weapons.

Nuclear reactors are a powerful, very pure source of neutrinos with energies between a few and several MeV. Daughter nuclides from fission are rich in neutrons and decay mostly via α and β decays. From the total energy produced, a small percentage is radiated away as antineutrinos since they easily escape the reactor. Reactors have been used to study neutrino properties as they provide a stable high flux of neutrinos at a fixed distance from the detector. Some of them like JUNO [Bal+13] and the Daya Bay experiment [An+12] are designed to measure neutrino oscillation parameters with high levels of precision and may be sensitive to the neutrino mass hierarchy [Gou+13].

Particle accelerators are often used to generate neutrino beams. Low energy beams can be obtained from pion decay at rest, resulting in a steady flux of mono-energetic ν_μ. High energy beams are the standard used for neutrino oscillation experiments, they can be produced from boosted pion decay and it is possible to select their charge and energy, yielding a beam of mostly ν_μ or $\overline{\nu}_\mu$ [Gou+13]. The technique consists in accelerating protons towards a material target which will produce kaons and pions. These will then be magnetically focused into a collimated beam and propagated through a vacuum tube until they naturally decay, similarly to what happens in the atmosphere. The muons from the decay have large lifetimes but are eventually removed from the beam through collisions along the path to the detector, hence resulting in a beam of muon neutrinos [Brá16].

2.1.2 Helicity and Chirality

For a Dirac fermion, helicity (or handedness) is the projection of the spin vector onto the linear momentum vector of a particle, as described by Equation (2.3). This is not an intrinsic property, but rather a state that relates to the physical properties of spin and momentum, since it can change depending on the reference frame of the observer [Pov+08].

$$\hat{\mathbf{h}} = \vec{\mathbf{S}} \cdot \frac{\vec{p}}{|\vec{p}|} \tag{2.3}$$

Chirality is a fundamental property which does not depend on motion. It appears for two different representations of Lorentz groups, and it determines if the particles can interact via the weak nuclear force. It is defined through the operator γ^5 and the projection operators are given by $1/2(1 \pm \gamma^5)$, where γ is the Dirac matrix [AH04].

For massless particles, helicity and chirality are indistinguishable from one another because it is not possible to have a real observer in a reference frame travelling faster than the speed of light. Thus, the observed particle will always appear to spin in the same direction as the axis of motion. In this situation, helicity is a relativistic invariant which always matches the chirality of the particle. Contrarily, in the case of massive particles, an observer in a reference frame moving faster than the particle would see the direction of its linear momentum reversed, as well as its helicity, regardless of the direction of its intrinsic chirality [Pov+08].

Every particle in the Standard Model has been verified to have a left-handed and right-handed version of chirality, with the exception of neutrinos and antineutrinos, as shown in Figure 2.6. Since the weak interaction only affects left-chiral fermions and right-chiral anti-fermions, this means it has only been possible to observe the neutrinos which interact through nuclear decay (left-chiral ν and right-chiral $\overline{\nu}$). The remaining two with opposite chirality would be *sterile neutrinos* (right-chiral ν and left-chiral $\overline{\nu}$) which should only interact gravitationally and thus, are virtually impossible to detect [Pov+08].

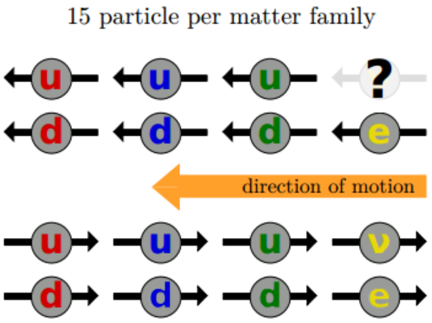

Figure 2.6: Helicity of elementary massless matter particles, according to the SM. In this case, helicity and chirality coincide, and since there is no record of right-handed neutrinos, only the left-handed ν is represented. Figure from [Del+16].

2.1.3 (C)(P) symmetry

Charge conjugation and Parity inversion symmetry states that the laws of physics should remain unchanged when a certain experiment involving a particle can be replicated with its antiparticle

whilst its spatial coordinates are mirrored. This implies that the equations in particle physics are invariant under the two transformations.
While P-symmetry appears to be valid for situations involving electromagnetism and strong interactions [LY56], tests conducted over beta decay [Wu+57] demonstrated that parity violation is a unique characteristic of weak interactions. For instance, an interaction which depends on helicity is not invariant under parity inversion because even though spin orientation is maintained, the momentum is not. On the other hand, if the helicity of neutrinos were fixed, and one applied the charge conjugation operator, then C-symmetry would be immediately violated as a left handed ν would be transformed into a left handed $\overline{\nu}$, which have never been confirmed to exist.
For neutrinos, and in general for all weak processes, C-symmetry and P-symmetry are violated separately, but the combination of both operators, CP, transforms a left handed ν into a right handed $\overline{\nu}$ interacting with equal strength - *CP conservation property of the weak interaction* [Pov+08].

2.1.4 B and L symmetries

In weak current interactions mediated by W^- and W^+ bosons, the antineutrinos present are always associated with the respective lepton [Pet16] [AH02]. This guarantees the leptonic number (L) is conserved through Equation (2.4), in which $n_l/n_{\overline{l}}$ is the number of leptons/antileptons. Baryonic number (B) is also conserved for all interactions in the SM through Equation (2.5), where $n_q/n_{\overline{q}}$ is the number of quarks/antiquarks.

$$L = \sum_{l=e,\mu,\tau} L_l = \sum_{l=e,\mu,\tau} (n_l - n_{\overline{l}}) = const. \tag{2.4}$$

$$B = \frac{1}{3}(n_q - n_{\overline{q}}) = const. \tag{2.5}$$

So far, no process has been observed where B and L numbers are not conserved, leading scientists to believe these may be symmetries of the SM. However, there is no justification as to why these quantities cannot vary, so these are usually called "accidental symmetries". On the other hand, (B-L) is a global conserved quantity which would not be broken by chiral or gravitational anomalies [FHL09].

2.1.5 Flavour oscillations

Following the solar neutrino problem observed by Davis, in 1969 Pontecorvo and Gribov proposed the solution that a neutrino could transform into a different type, therefore escaping detection. Years later, in an experiment which was only sensitive to electron neutrinos, confirmation followed that the reason for this discrepancy was indeed due to the neutrino being described by a combination of 3 quantum states, allowing them to change properties while they travel, *i.e.* they oscillate between states[9] [Lan13].

The observation of neutrino oscillations by the Super-Kamiokande (1996) [Fuk+98b] and SNO (2001)[Ahm+02] experiments, showed that a neutrino in a well defined flavour state has a non-zero probability of being observed in a different flavour than the one it originally had, after travelling away from its source [Gou+13]. Proof of these oscillations suggests two important properties: neutrinos have non-zero mass and the flavour eigenstates are a superposition of the mass eigenstates. This phenomenon is also referred to as "neutrino-mass-induced flavour oscillations". The probability of an oscillation depends on the neutrino energy, distance travelled,

---

[9] In order to paint a picture of these abstract oscillations, an analogy by Emily Conover featured on a Fermilab/SLAC publication is available at: www.symmetrymagazine.org/article/june-2013/cinderellas-convertible-carriage.

neutrino squared mass differences and the elements of the leptonic mixing matrix $\mathcal{U}$. [Gou+13].

Considering ν_a where $a = e, \mu, \tau$ as the flavour eigenstates and ν_i with $i = 1, 2, 3$ as the mass eigenstates, the relation between the two is given by Equation (2.6):

$$|\nu_a\rangle = \sum_{i=1}^{3} U_{ai}^{*} |\nu_i\rangle \tag{2.6}$$

$$\begin{pmatrix} \nu_e \\ \nu_\mu \\ \nu_\tau \end{pmatrix} = \begin{pmatrix} U_{e1} & U_{e2} & U_{e3} \\ U_{\mu 1} & U_{\mu 2} & U_{\mu 3} \\ U_{\tau 1} & U_{\tau 2} & U_{\tau 3} \end{pmatrix} \begin{pmatrix} \nu_1 \\ \nu_2 \\ \nu_3 \end{pmatrix}$$

where U_{ai} are matrix elements of the Pontecorvo-Maki-Nakagawa-Sakata matrix ($\mathcal{U}_{PMNS}$).

If neutrinos interact as predicted by the SM and there are only 3 mixing flavours, then $\mathcal{U}$ is unitary. It is parameterized with three mixing angles $\theta_{12}, \theta_{13}, \theta_{23}$ and a complex CP violating phase δ, defined as follows[10] [Gou+13]:

$$tan^2\theta_{12} \equiv \frac{|U_{e2}|^2}{|U_{e1}|^2} \qquad tan^2\theta_{23} \equiv \frac{|U_{\mu 3}|^2}{|U_{\tau 3}|^2} \qquad sin^2\theta_{13} e^{-i\delta} \equiv U_{e3} \tag{2.7}$$

Equation (2.8) describes the mass eigenstates as a function of time, where $i = 1, 2, 3$ and $E_i = (m_i^2 + p^2)$.

$$|\nu_i(t)\rangle = e^{-jE_i t} |\nu_i\rangle \tag{2.8}$$

For example, by using Equation (2.8) along with $\mathcal{U}_{PMNS}$ elements, the weak eigenstate of electron flavour would show that after it propagates from its source, there is a certain amount of muon and tau flavour mixed in, and thus a finite probability of it being detected in those flavours (see Figure 2.7).

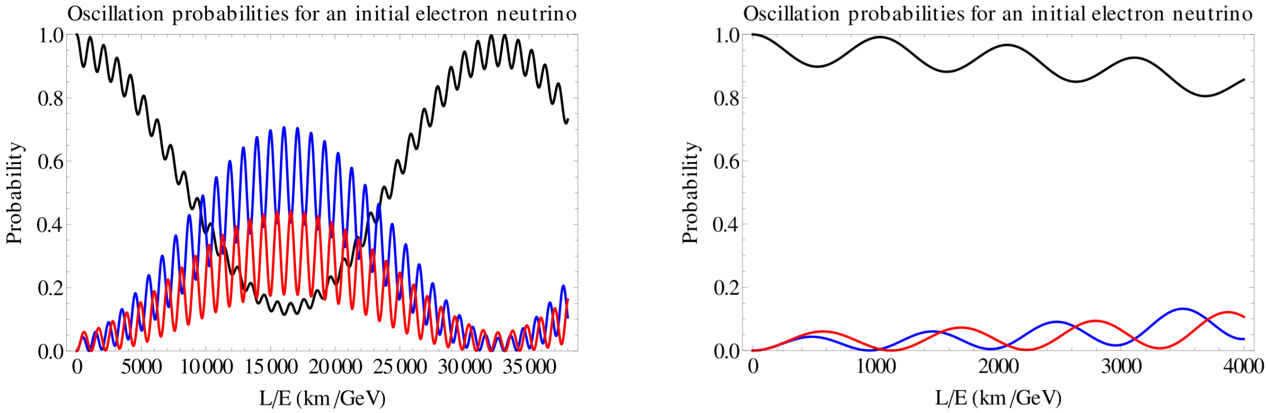

Figure 2.7: Graphs representing the oscillation probability of each flavour, for an initial electron neutrino, after propagating long distances (left) and short distances (right), considering normal mass hierarchy (see Subsection 2.1.6). The black line corresponds to ν_e, the blue is for ν_μ and the red line is for ν_τ. Figure from [Mes].

---

[10] There are possibly two additional phases, ξ and ζ, which are related to the Majorana hypothesis, but these are not responsible for the interchange of flavours.

2.1.6 Mass hierarchy

In the SM, neutrinos are massless and all other elementary particles obtain their mass by interacting with the Higgs field [Org12]. Neutrino masses are extremely small when compared to other fermions; and there is no apparent explanation as to why there is such a large gap in the mass scale between the neutrino and the electron (see Figure 2.8). Non-zero neutrino masses along with these odd characteristics are an indicator that we do not fully understand the mechanism of the Higgs mass scale. It may open a new path for a completely new mechanism unrelated to electroweak symmetry breaking, or mean that the current mechanism is more complex than dictated by the standard model [Gou+13].

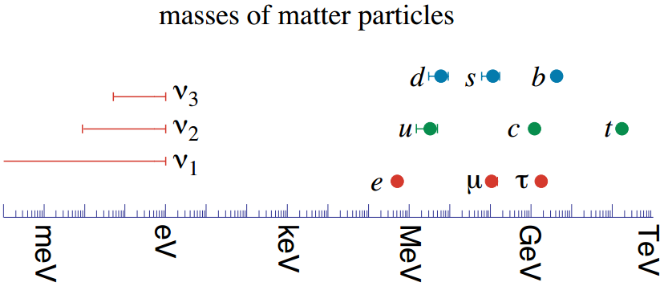

Figure 2.8: Comparative view of fermion masses in the Standard Model. Here are depicted neutrino masses assuming a normal hierarchy (see main text for details) with an upper bound $m_i < 1$ eV, for all $i = 1, 2, 3$. Figure from [Gou+13].

Although neutrino oscillation experiments are not sensitive to the absolute mass values nor to the δ phase, they have allowed us to obtain the square mass difference between neutrino eigenstates [Del+16].

In order to relate the matrix elements to experimental observables, it is crucial to define and limit the neutrino mass eigenstates: $m_2^2 > m_1^2$ and $\Delta m_{21}^2 < |\Delta m_{31}^2|$. The mass related oscillation observables are Δm_{21}^2, $|\Delta m_{31}^2|$ and the sign of Δm_{31}^2.

The mass splitting between eigenstates ν_1 and ν_2 is represented by δm^2, which is obtained from solar neutrino oscillation data; and Δm^2 is the separation between ν_3 and the mid-point of ν_2 and ν_1, and is measured from atmospheric neutrino data [Gou+13]. These parameters are described through Equation (2.9).

$$\begin{aligned} \delta m^2 &= \Delta m_{21}^2 = m_2^2 - m_1^2 \\ \Delta m^2 &= \Delta m_{31}^2 - \frac{\Delta m_{21}^2}{2} = m_3^2 - \frac{m_1^2 + m_2^2}{2} \end{aligned} \tag{2.9}$$

Experimental data confirms the solar mass difference is positive ($\delta m^2 > 0$) but the sign for the atmospheric mass difference (Δm^2) is still unknown, which means it is necessary to find the relation between the mass eigenstates. Is ν_3 more or less massive than ν_1 and ν_2? There are two possible scenarios [Del+16]:

- If Δm^2 is positive $\Rightarrow$ $m_3^2 > m_2^2$ and neutrinos have a normal mass hierarchy (NH).
- If Δm^2 is negative $\Rightarrow$ $m_3^2 < m_1^2$ and neutrinos have an inverted mass hierarchy (IH).

Figure 2.9 illustrates the difference in hierarchies and the probability of finding one of the flavour eigenstates if the neutrino is in a certain mass eigenstate.

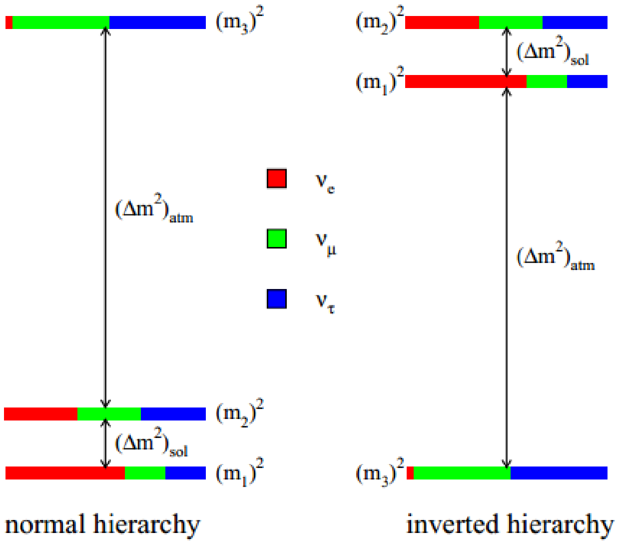

Figure 2.9: The two possible arrangements for the neutrino mass hierarchy. Normal hierarchy predicts two light neutrinos and a heavier one. In inverted hierarchy the prediction accounts for a light neutrino and two heavy neutrinos. The coloured bars show the fraction $|U_{ai}|^2$ of each flavour ν_a, contained in each mass eigenstate ν_i. For example, $|U_{e2}|^2$ corresponds to the red (ν_e) portion of the $(m_2)^2$ bar. Figure from [Gou+13].

2.2 Double Beta Decay ($2\nu\beta\beta$)

Theorised by Maria Goeppert Mayer in 1935 [Goe35], double beta decay (DBD) is a transition between isobaric nuclei in which two neutrons decay into protons with the emission of two electrons and two electron antineutrinos, as shown in Equation (2.10).

$$(A, Z) \rightarrow (A, Z + 2) + 2e^{-} + 2\overline{\nu}_e \tag{2.10}$$

This is one of the rarest known decays as it is a second-order weak interaction process. It only occurs in isotopes in which single beta decay is forbidden either by a negative mass difference between the parent and daughter nuclei or suppressed by selection rules. Thus it is observable in even-even nuclei (even atomic number Z, even neutron number N), as summarised in Figure 2.10 [Bia17].

The first observation of DBD is attributed to Inghram and Reynolds as a result of the first geochemical experiment [IR50], which consisted in separating xenon from ancient minerals and analysing the isotopes present in the sample in search of an excess amount of ^{130}Xe. In 1950, they successfully detected the transition of ^{130}Te into ^{130}Xe and calculated a half-life of $T^{2\nu}_{1/2} = 1.4 \times 10^{21}$ years[11] [Bar11], close to the current best value of $T^{2\nu}_{1/2} = 8.2 \times 10^{20}$ years [Mes+02].

Since then, several experiments have detected it, and over 30 nuclei have been observed to exhibit this decay. This process has half-lives ranging from $10^{18} - 10^{24}$ years and the Q-values vary from $2.4 - 3$ MeV [Car18].

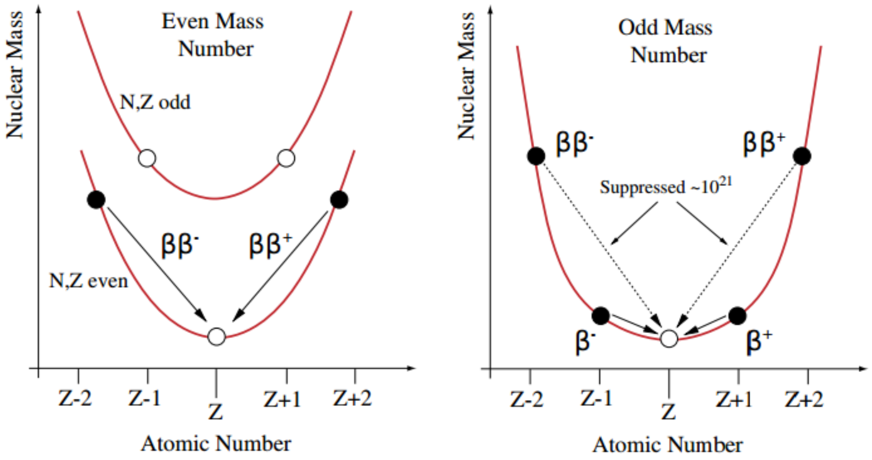

Figure 2.10: Nuclear mass as a function of the atomic number Z for a DBD decay candidate with an even and odd mass number A. [Left plot] Considering an even A nuclei (A, Z), the double β decay from an even-even nucleus is possible because the resulting (A, Z+2) nucleus is lighter. In contrast, the single β decay from an odd-odd nucleus creates a heavier (A, Z+1) daughter nucleus and is therefore kinematically forbidden. [Right plot] In the case of an odd A nuclei (A, Z), if it theoretically can decay through both single and double β decay, the branching ratio for double β decay is too small and difficult to observe due to the dominant branch of single β decay. Figure from [Del+16].

---

[11] Actually, the discovery of DBD is more commonly credited to the group of Michael Moe from UC Irvine, as they observed it in laboratory in 1987 [Moe14]. It only became clear after many years that DBD decay was indeed observed for the first time in 1950.

2.2.1 Neutrinoless Double Beta Decay ($0\nu\beta\beta$)

In 1937, Ettore Majorana discussed the possibility that the neutrino could be its own antiparticle by demonstrating the results of beta decay theory were unchanged in this situation [Maj08]. Later, in 1939, Wendell Furry studied this hypothesis [Fur39] and concluded that, if neutrinos were in fact "Majorana particles", then DBD would be more likely to occur without the emission of neutrinos - *neutrinoless double beta decay* (NDBD). He described the process as follows: the nucleus would emit one electron and transit to a virtual intermediate state along with a virtual $\overline{\nu}$ and then this virtual neutrino ($\nu \equiv \overline{\nu}$) would be absorbed by the intermediate nucleus and induce its decay, emitting a second electron [Bar11].

Between 1935 and 1939, DBD and NDBD were estimated to have lifetimes of $T^{2\nu}_{1/2} \approx 10^{21} - 10^{22}$ years and $T^{0\nu}_{1/2} \approx 10^{15} - 10^{16}$ years, respectively.
Considering the two distinctive estimates, as the lower value was relative to NDBD, it was likely that this decay would have been observed by detectors existing at that time, corroborating the Majorana neutrino hypothesis [Bar11]. Nonetheless, the first few experiments on the search for this decay ended up being unsuccessful. Between 1948 and 1949, Edward Fireman conducted experiments to detect the decay of ^{124}Sn, and thought he had confirmation of NDBD when he obtained $T_{1/2} = (4 - 9) \times 10^{15}$ years [Fir49]. But his results were disproved by more sensitive experiments years later, as the best limit for this isotope was $T_{1/2}(^{124}Sn) > 2{\times}10^{17}$ years [KL52].

Furthermore, after the discovery of space parity violation and the V-A (vector minus axial vector or left-handed) nature of weak interactions [AH04], it was evident that the probability of observing NDBD was much smaller than that of DBD. Since no experiment has given positive results for the neutrinoless process, the half-life lower limit keeps increasing. Nowadays, dedicated experiments are searching for NDBD with $T^{0\nu}_{1/2} \approx 10^{26} - 10^{28}$ years [Bar11].

There are different proposals for extensions of the SM which attempt to explain this process, and one of the most appealing is the exchange of a light, massive Majorana neutrino. This can be represented by Equation (2.11), and in the light neutrino exchange model by the Feynmann diagram in Figure 2.11.

$$(A, Z) \rightarrow (A, Z + 2) + 2e^- \tag{2.11}$$

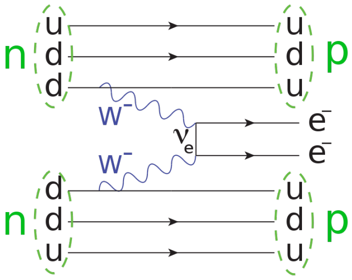

Figure 2.11: Diagram of the $0\nu\beta\beta$ process due to the exchange of massive Majorana neutrinos [Del+16].

The observable of NDBD is its half-life, which can be expressed by Equation (2.12) [Del+16]:

$$\left(T^{0\nu}_{1/2}\right)^{-1} = G^{0\nu}(Q, Z) \cdot |\mathcal{M}^{0\nu}|^2 \Big(f(m_{\nu_i}; U_{ei})\Big)^2 \tag{2.12}$$

where $G^{0\nu}$ is the lepton phase-space factor (PSF), $\mathcal{M}^{0\nu}$ is a nuclear matrix element (NME), and the last term, $f(m; U)$, quantifies the intensity of the lepton number violating process underlying the decay that represents New Physics [Car18]. In the light neutrino exchange model, the factor

$f(m_{\nu_i};U_{ei})$ is simply $\langle m_{\beta\beta}\rangle/m_e$ and the expression can be written as Equation (2.13), with $\langle m_{\beta\beta}\rangle$, the effective Majorana mass, being given by Equation (2.14) [Car18].

$$\left(T^{0\nu}_{1/2}\right)^{-1} = G^{0\nu}(Q,Z)\cdot|\mathcal{M}^{0\nu}|^2\left(\frac{\langle m_{\beta\beta}\rangle}{m_e}\right)^2 \tag{2.13}$$

$$\langle m_{\beta\beta}\rangle = \left|\sum_i U_{ei}^2 m_{\nu_i}\right| = |u_{e1}^2 e^{i\alpha 1}m_1 + u_{e2}^2 e^{i\alpha 2}m_2 + u_{e3}^2 m_3| \tag{2.14}$$

In this equation, m_{ν_i} are the neutrino mass eigenvalues, U_{ei} are parameters of the PMNS matrix, and $\alpha_{1,2}$ are the two Majorana phases [Car18].

In Equation (2.12), the PSF can be calculated with great precision given the description of the nuclear Coulomb effect on the emitted electrons. The NME term describes the transition between the initial and final nuclear states and obtaining its value is more troublesome. The reason is that there are several possible approaches to calculate them[12], with each model rendering results for the predicted NME which have a spread of a factor 2-3 as shown in Figure 2.12, introducing uncertainty on the limits of the decay half-life [Car18]. Thus, NDBD also presents an opportunity to test and refine these nuclear models.

Many theories have come up on the pursuit to explain $0\nu\beta\beta$ decay. Currently, the most appealing one is the exchange of a light massive Majorana neutrino, but among the alternatives are: introducing higher dimensional operators, a heavy neutrino exchange and models with right-handed (RH) currents [Del+16].

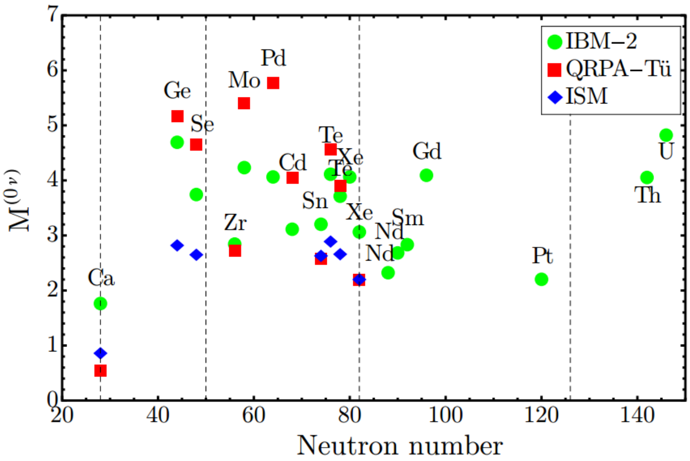

Figure 2.12: Comparison of recent NMEs calculations for NDBD in different nuclei, achieved with 3 distinct models. Figure from [Del+16].

$0\nu\beta\beta$ decay and the SM

The fact that (B-L) is a symmetry conserved non-perturbatively is a sufficient condition to forbid NDBD within the formulations of the SM. It is clear that without the emission of antineutrinos, (B-L) would be 2 values lower than in the DBD regular transition. This would immediately motivate changes to the current SM of particle physics. Furthermore, the SM was initially developed considering neutrinos to be massless particles, which we know they are not, as their flavour oscillations are a manifestation of their massive nature. The connection between these symmetries and the mass mechanism of neutrinos is therefore already an unsolved

---

[12] A summary on different NMEs models can be found in [Del+16]

problem in the SM [Del+16].

Although CP violation has been discovered in 1964 by Cronin and Fitch [Chr+64], this has only been observed for a specific set of parameters. It is allowed in the SM if a complex phase appears in the CKM matrix which describes quark mixing. However, the available data from neutrino oscillation experiments indicates the PMNS matrix - which descibes neutrino mixing - could be a completely new source of CP violation: if the probabilities for neutrinos to oscillate are fundamentally different from those of antineutrinos, then they violate CP invariance [Gou+13].

Importance of $0\nu\beta\beta$ searches

Observation of NDBD would be the first evidence that Majorana particles exist, meaning the current models for elementary particles would have to be re-evaluated and modified in order to agree with the new findings. This would prove the existence of processes which do not conserve leptonic number L, as well as violation of conservation of (B-L) number, which would no longer be considered fundamental symmetries [Car18]. On the other hand, NDBD could help us understand the matter/antimatter asymmetry in our Universe and would provide us insight into the mass mechanism of neutrinos and their properties [Gou+13].

From Equation (2.13), it is evident that an experimental limit on the NDBD half-life constrains the value of the effective Majorana mass, as described by Equation (2.15), which can provide some information on the absolute values of neutrino masses and how they are ordered [Del+16].

$$m_{\beta\beta} \leq \frac{m_e}{\mathcal{M}^{0\nu}\sqrt{G^{0\nu}T^{0\nu}_{1/2}}} \tag{2.15}$$

In Figure 2.13, the plot shows the effective Majorana neutrino mass as function of the lightest neutrino ($m_{lightest} = m_1$ for NH and $m_{lightest} = m_3$ for IH). If masses are ordered according to the inverted hierarchy, it is expected that $m_{\beta\beta} \sim 15 - 50$ meV, and $m_{\beta\beta} < 5$ meV if they have normal hierarchy [Car18]. The current best limit on $m_{\beta\beta}$ is attributed to the KamLAND-Zen experiment with a value of $m_{\beta\beta} < 61 - 165$ meV, in the quasi-degenerate region (see Subsection 3.2.1 for details) [Gan+16]. As experimental values for $T^{0\nu}_{1/2}$ increase, the upper limit on $m_{\beta\beta}$ decreases. Thus, if a value below the IH region is achieved, it would be a strong indicator that neutrino masses follow a NH instead.

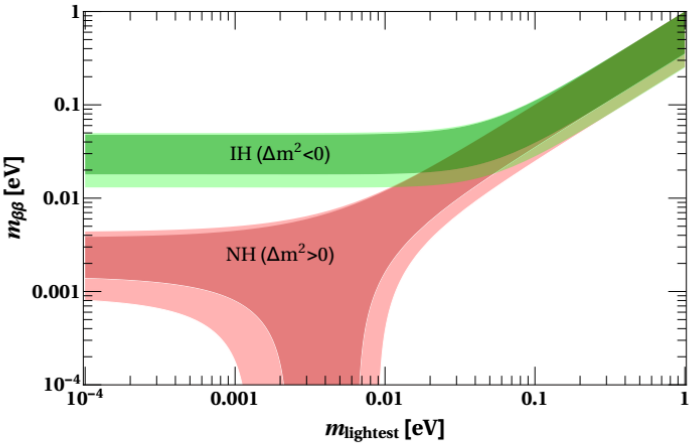

Figure 2.13: Predictions on the effective Majorana neutrino mass $m_{\beta\beta}$ as function of the lightest neutrino mass $m_{lightest}$ for each hierarchy type (green for NH and pink for IH). The darker coloured regions are the predictions based on best-fit values and the lighter coloured areas correspond to the 3σ ranges calculated from uncertainties on oscillation parameters. Figure from [Del+16].

Chapter 3

Experimental searches for $0\nu\beta\beta$ decay

3.1 Experimental Considerations

Searching for NDBD is very challenging. The energy range of electrons released from DBD lies in a region where many types of background appear and hinder their detection, the long lifetimes call for large amounts of emitter material to increase the probability of detection, and separating the signal of NDBD from DBD requires excellent energy resolution. A detector for this purpose needs to fulfil certain requirements to have a chance of being successful, which will be discussed in this section.

There are four forbidden processes regarding neutrinoless decay modes, corresponding to the allowed processes of double beta decay (Equation 3.1), double positron emission (Equation 3.2), double electron capture (Equation 3.3), and electron capture with positron emission (Equation 3.4)[Del+16]. Different types of experiments are underway or planned to explore each of them, although this work focuses only on the first of this list, neutrinoless double beta decay, which is the most widely studied.

$$(A,Z) \rightarrow (A,Z+2) + 2e^- + 2\overline{\nu}_e \ \boldsymbol{(2\nu\beta^-\beta^-)} \qquad (A,Z) \rightarrow (A,Z+2) + 2e^- \ \boldsymbol{(0\nu\beta^-\beta^-)} \tag{3.1}$$

$$(A,Z) \rightarrow (A,Z-2) + 2e^+ + 2\nu_e \ \boldsymbol{(2\nu\beta^+\beta^+)} \qquad (A,Z) \rightarrow (A,Z-2) + 2e^+ \ \boldsymbol{(0\nu\beta^+\beta^+)} \tag{3.2}$$

$$(A,Z) + 2e^- \rightarrow (A,Z-2) + 2\nu_e \ \boldsymbol{(2\nu ECEC)} \qquad (A,Z) + 2e^- \rightarrow (A,Z-2) \ \boldsymbol{(0\nu ECEC)} \tag{3.3}$$

$$(A,Z) + e^- \rightarrow (A,Z-2) + e^+ + 2\nu_e \ \boldsymbol{(2\nu EC\beta^+)} \qquad (A,Z) + e^- \rightarrow (A,Z-2) + e^+ \ \boldsymbol{(0\nu EC\beta^+)} \tag{3.4}$$

3.1.1 Signature of $0\nu\beta\beta$

The DBD spectrum covers a wide range of energies because the neutrinos released in the transition carry a variable fraction of the total energy, while the electrons share the remaining energy. In a hypothetical NDBD, we are interested in detecting the two emitted electrons that carry most of the kinetic energy of the transition, considering the energy from the recoiling nucleus is negligible. Although there is a probabilistic distribution for the energies and angles of emission of electrons [Tay20], in a simplified scenario, if we were to observe it, we would see the two electrons emitted back to back and each depositing roughly half the energy at the end of their path, as shown in Figure 3.2. Moreover, the signal produced by NDBD is a monochromatic

peak at Q-value as represented in Figure 3.1 [Del+16].
The DBD spectrum extends to $Q_{\beta\beta}$, having excellent energy resolution is crucial to differentiate the two decay modes (see inset of Figure 3.1). Since the hypothetical NDBD signal is so rare, the detector should process signals fast, meaning good temporal resolution and minimal dead time are required, as it will be looking for an excess rate of events in the region of $Q_{\beta\beta}$, comparatively to the tail of DBD decay spectrum. Finally, the technology chosen for event discrimination should be able to reject interactions that could be mistaken for NDBD [Car18].

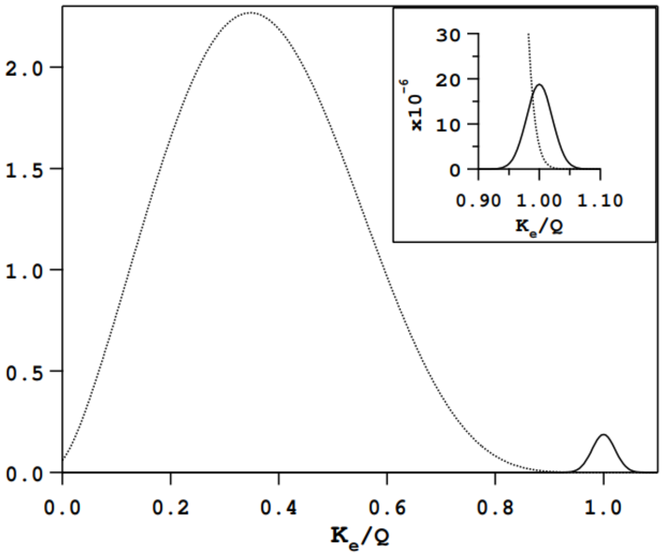

Figure 3.1: Schematic view of DBD (dotted line) and hypothetical NDBD (solid line) spectra. The spectra illustrates the sum of the electron kinetic energies (K_e) scaled with the total energy of the decay (Q), convolved with an energy resolution of 5% FWHM. The areas of the curves do not represent the expected relative rates [EV02]. The inset shows the zoom around the Q-value, normalised to 10^{-6}. Figure from [Car18].

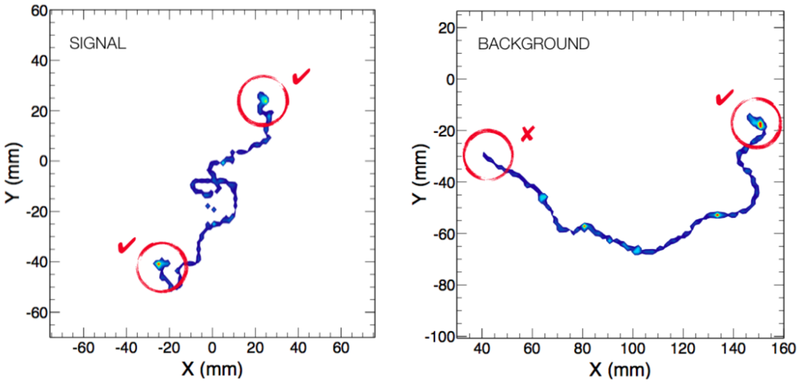

Figure 3.2: Monte Carlo simulation of the topology of a ^{136}Xe NDBD signal (left), contrasted by a similar topology in a background event (right), as shown by the NEXT collaboration. The background signal is a single electron produced by a $^{214}Bi\ \gamma$ of 2.44 MeV. A NDBD event in the conditions of the NEXT detector (gaseous xenon at ~10 bar) would produce a long track with two identical "blobs" at each end of the track, qualitatively corresponding to the energy deposited by each electron from the decay. The event topology on the right would be rejected and considered background because there is a significant ionisation density only at one end of the travelled path. Figure from [Col+16].

3.1.2 Isotope choice

Since not many isotopes can decay via NDBD and this is such a slow transition, it would make sense to choose an isotope with the shortest predicted neutrinoless half-life to maximise chances of observation. However, it has been confirmed that when combining the PSFs and NMEs, there is no isotope more advantageous than the other, they all have qualitatively the same decay rate per unit mass of isotope for any given value of $m_{\beta\beta}$ [ROB13]. Table 3.1 lists some relevant isotopes that undergo DBD along with the experimental half-life values.

Table 3.1: List of some DBD emitters, their respective isotopic abundance, Q-values and measured half-life values from several state-of-the-art experiments [Saa13].

Isotope	Abundance (%)	$Q_{\beta\beta}$ (MeV)	$T_{1/2}^{2\nu\beta\beta}$ (years)
^{48}Ca	0.187	4.268	$6.4^{\pm 0.7(stat.)}_{\pm 1.2(syst.)} \times 10^{19}$ [Arn+16b]
^{76}Ge	7.8	2.039	$(1.925 \pm 0.094) \times 10^{21}$ [Ago15]
^{100}Mo	9.6	3.035	$7.12^{\pm 0.18(stat.)}_{\pm 0.10(syst.)} \times 10^{18}$ [Arm+20]
^{130}Te	34.08	2.527	$7.9^{\pm 0.1(stat.)}_{\pm 0.2(syst.)} \times 10^{20}$ [Nut+20]
^{136}Xe	8.9	2.458	$2.21^{\pm 0.02(stat.)}_{\pm 0.07(syst.)} \times 10^{21}$ [Gan+16]
^{150}Nd	5.6	3.371	$9.34^{\pm 0.22(stat.)}_{\pm 0.62(syst.)} \times 10^{18}$ [Arn+16a]

There are a few criteria to take into account when deciding what $\beta\beta$ emitter to use for an experiment [Del+16]:

- High isotopic abundance: experiments with large emitter masses, depend either on the abundance of the chosen isotope, or on the ease of enrichment. It is difficult to get large amounts of a material with high Q-value, so there is a trade-off between the energy and the enrichment that can be achieved.

- High Q-value: ideally, the emitter should have a Q-value high enough from the energy range of natural β and γ radioactivity. The 2.614 MeV of ^{208}Tl is effectively the end point of natural radioactivity, although there is a rarer decay at 3.270 MeV from ^{214}Bi.

- Scalability: this determines how easy it would be to recreate the experiment with a higher amount of emitter mass and increased exposure to check previous results and improve future statistics. In order to possibly observe a few decays and explore the IH region, the amount of source material used in the experiment should be around hundreds of kilograms up to tonnes (depending on the abundance of the material). Not all technologies are suitable to create such large scale experiments, which makes this a decisive factor.

- Detection technique: there are two different approaches when planning the construction of the detector. One is to make the detector coincide with the source of NDBD which facilitates the collection of the two emitted electrons. The other is to separate the detector and source which in turn grants better topological reconstruction of events. This is further explained in section 3.1.5.

- Availability and cost: as experiments increase in size and number, there is a higher demand for the production of certain isotopes. This also raises the prices, making the race for obtaining the best results even tougher.

There is a strong dependence of the PSF on $Q_{\beta\beta}$ and it can be shown that $G^{0\nu} \propto Q^5_{\beta\beta}$ which in turn influences the neutrinoless decay half-life as $T^{0\nu}_{1/2} \propto Q^{-5}_{\beta\beta}$ [Saa13]. At the moment many experiments choose the ^{136}Xe isotope for its high $Q_{\beta\beta}$, ease of enrichment, and it places the energy search region above many common backgrounds.

3.1.3 Background

The long lifetimes complicate the detection of the two electrons due to background events that occur at higher rates in the region of interest (ROI) and can mask the NDBD signal. Any interaction producing a signal similar to that of NDBD is detrimental to the sensitivity of the experiment and worsens the signal-to-background ratio (SNR). Background originates mainly from cosmic rays, internal and external radioactivity, neutrinos and DBD itself, although the relevance of each of these backgrounds and how they will affect the observations depends on the detector type and technology employed.

The search for rare events is incompatible with using a surface detector, as the flux of cosmic muons is too great and would dominate over any interactions of interest. Therefore, the first step towards reducing background is building laboratories underground, where detectors are protected from cosmic rays. Depending on the depth, this can reduce the cosmic muon flux up to $\sim$6 orders of magnitude or more (as is the case with the SNOLAB experiment) [MH06].

The most common background comes from natural α, β, and γ radioactivity, which can arise from the long-lived isotopes of ^{238}U and ^{232}Th[1]. γ rays can interact via photoelectric effect, Compton scattering, or pair production, and give an energy spectrum that overlaps the DBD signal. α particles from decay chains usually have higher energies than those of $Q_{\beta\beta}$, but electrons released from β decays are more likely to mimic a $\beta\beta$ event. The natural radioactivity cut-off is an exponential drop in the spectrum which occurs after the 2.614 MeV line of ^{208}Tl from the ^{232}Th chain, so isotopes with $Q_{\beta\beta}$ higher than that benefit from a region with a significant reduction in background, although this is not the case for ^{136}Xe which has $Q_{\beta\beta} = 2.458$ MeV. The presence of Radon is troublesome, stemming from the decay chains of ^{238}U and ^{232}Th, which produce ^{222}Rn and ^{220}Rn, respectively. Radon gas can diffuse from the bedrock and detector surfaces into the detector, conditioned by the permeability of materials used. These Radon isotopes can further decay into two other background sources, that present high Q_β, $^{214}Bi \rightarrow \, ^{214}Po$ at 3.27 MeV, and $^{208}Tl \rightarrow \, ^{208}Pb$ [*stable*] at 4.99 MeV [Saa13] (see decay chain diagrams in the Appendix).

One of the most limiting backgrounds for NDBD comes from neutrons from natural radioactivity. After suffering thermalization through collisions, the slow neutrons can be captured by other nuclei of the detecting medium with emission of γs and subsequent β decay, which in turn will interact with the detector and its surroundings. This background produces a flat energy spectrum, that makes it more troublesome at higher energies where one might expect neutrinoless events at $Q_{\beta\beta}$[Saa13].

As background can emerge from the detector itself as well, all rare event experiments select only materials with high levels of radiopurity and often perform cleaning campaigns to minimise traces of long-lived radioactive contaminants.
Being underground also brings the disadvantage of being in the proximity of radioactive material present in bedrocks, which implies shielding the detector with multiple layers. The first few layers are usually passive shields made of high-Z materials to protect the detector against

---

[1] Uranium and Thorium are usually the main concern, but there are others contributing to this type of background such as ^{60}Co and ^{40}K.

external γ-rays (or water for neutrons). These are followed by a layer of low-Z material intended to moderate fast neutrons which will then participate in (n, γ) reactions. The resulting γs are absorbed by the former shields.
Active shielding (vetoing) is also useful to tag cosmic muons and rule out external background events or even interactions from inside the detector that match with events in the active shield. This type of shielding can be achieved with a scintillator medium and photodetectors surrounding one of the passive layers [Saa13]. There are other active methods to improve SNR during the stage of data analysis, such as reconstruction of event topology, pulse-shape discrimination and combination of those detection signatures [GM15].

In some detectors, it is also possible to use the detection medium as a form of self-shielding. If the detection medium coincides with the emitter, one can use a large amount of a dense, high-Z material and, in data analysis, define two separate volumes. The outer layer helps scatter some types of radiation and prevents it from entering the "quiet" inner layer of the fiducial volume with lower background [Mou+17].

To study Majorana neutrino masses in the IH region ($m_{\beta\beta} \sim 15 - 50$ meV), even the best ongoing experiments need to achieve high exposures of over 100 kg.year, and have their background level reduced to reach values of about $10^{-3} counts/(kg.year)$ in the neutrinoless ROI. Exploring neutrino masses in the NH region ($m_{\beta\beta} < 15$ meV) will only be possible with massive, nearly background-free experiments [GM15].

3.1.4 Sensitivity parameters

Sensitivity quantifies the detector's ability to observe a characteristic neutrinoless signal above the background, and in this context, it is defined as the total decay half-life with respect to the smallest detectable signal at a given confidence level, usually 90%. It can be expressed by Equation (3.5), where t_{live} is the live time of the experiment, ϵ is the detection efficiency, $N_{\beta\beta}$ is the number of nuclei decaying through $\beta\beta$ and N_{peak} is the number of decays in the region of interest [Del+16]:

$$T_{1/2} = ln(2) \cdot t_{live} \cdot \epsilon \cdot \frac{N_{\beta\beta}}{N_{peak}} \tag{3.5}$$

If no peak is detected, the sensitivity is instead defined as the decay half-life of the maximum signal that could be hidden behind background fluctuations n_B, at confidence level n_σ. This is also known as the "detector factor of merit" $S^{0\nu}$ [CP13], and to calculate it, it is required that the neutrinoless signal exceeds the standard deviation of the total detected counts in the region of interest. Assuming Poisson statistics, this follows that for a confidence level of n_σ, the relation is $n_{\beta\beta} \geq n_\sigma \sqrt{n_{\beta\beta} + n_B}$. Thus, the sensitivity can now be written as Equation (3.6) in which $n_{\beta\beta}$ is the number of NDBD events [Del+16]:

$$S^{0\nu} = T_{1/2}^{Back.fluct.} = ln(2) \cdot t_{live} \cdot \epsilon \cdot \frac{n_{\beta\beta}}{n_\sigma \cdot n_B} \tag{3.6}$$

Considering that the background scales up with the amount of source mass, one can write $N_B = B \cdot t_{live} \cdot \Delta \cdot M$ and $n_B = \sqrt{N_B} = \sqrt{B \cdot t_{live} \cdot \Delta \cdot M}$. Additionally, $N_{\beta\beta}$ can be rewritten as $N_{\beta\beta} = x \cdot \eta \cdot N_A \cdot M/\mathcal{M_A}$, and sensitivity then follows Equation (3.7).
These variables correspond to background rate per unit mass, time and energy (B), the FWHM energy resolution (Δ), the mass of the detector (M), the molecular mass ($\mathcal{M_A}$), the number of $\beta\beta$ atoms (x), the isotopic abundance of the NDBD candidate (η), and finally, the Avogadro number (N_A) [CP13].

$$S^{0\nu} = T_{1/2}^{Back.fluct.} = ln(2) \cdot \epsilon \cdot \frac{1}{n_\sigma} \cdot \frac{x\eta N_A}{\mathcal{M_A}} \sqrt{\frac{M \cdot t_{live}}{B \cdot \Delta}} \tag{3.7}$$

There are two statistical regimes that help compare different experiments according to the product of their performance (P) and scale (S). The scale is measured in number of moles of detectable isotope (including efficiencies and isotopic abundance) times years of live time, and performance has the dimensions of background counts per mole of detectable isotope per year [Bia17].

The first regime is the case of finite background, when $P \times S > 1$, the signal of interest can be hidden by background events, described by Equation (3.8). On the other hand, experiments generally strive for the zero background regime (ZB), when $P \times S \lesssim 1$, sensitivity will depend only on the signal magnitude and its fluctuations. Thus, the former Equation (3.7) is no longer valid, and ZB sensitivity is expressed by Equation (3.9), where N_S is the number of observed events in the region of interest [Del+16]. The feature of this regime is that it does not depend on background level or energy resolution and can be achieved by having a large amount of source mass and acquiring data for extended periods of time [CP13].

$$M \cdot t_{live} \cdot B \cdot \Delta > 1 \longrightarrow S_B^{0\nu} = T_{1/2}^{Back.fluct.} = ln(2) \cdot \epsilon \cdot \frac{x\eta N_A}{\mathcal{M}_\mathcal{A}} \sqrt{\frac{M \cdot t_{live}}{B \cdot \Delta}} \tag{3.8}$$

$$M \cdot t_{live} \cdot B \cdot \Delta \lesssim 1 \longrightarrow S_{ZB}^{0\nu} = T_{1/2}^{Zero\ back.fluct.} = ln(2) \cdot \epsilon \cdot \frac{x\eta N_A}{\mathcal{M}_\mathcal{A}} \frac{M \cdot t_{live}}{N_S} \tag{3.9}$$

In order to fully explore the IH mass region, sensitivity must reach the orders $10^{26} - 10^{28}$ years. Several research collaborations have projected sensitivities for their experiments reaching this goal, as discussed in section 3.2.

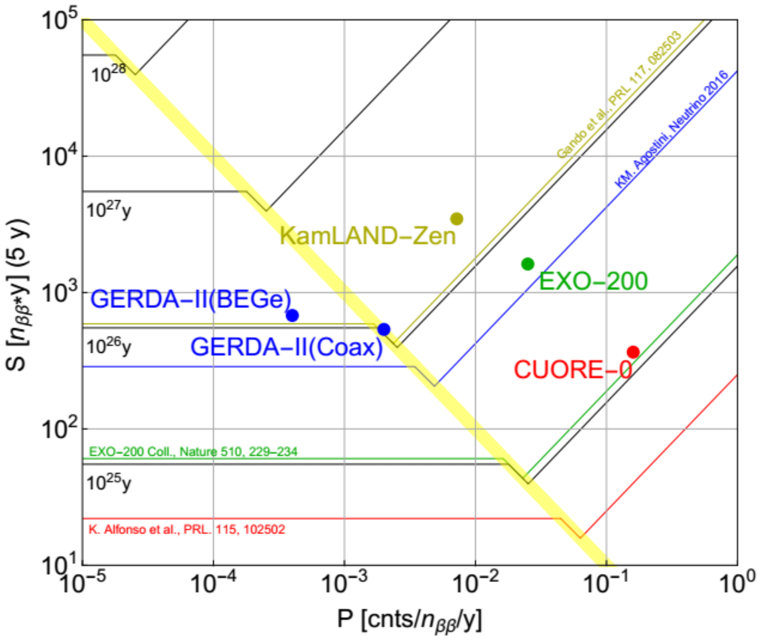

Figure 3.3: Comparison of experiments and published limits (filled circles) on the total half-life according to a P-S plane. Figure from [Bia17].

3.1.5 Detection Techniques

As aforementioned, there are a few critical characteristics desired for detectors across the board, despite the chosen technique: good energy resolution, low background, a large isotope mass, and high detection efficiency for the two electrons. However, it is impossible to optimise all of these simultaneously in a single detector. So one must choose a detection technique with an acceptable trade-off, pondering with its other characteristics [Saa13].

The observation of rare decays can derive from indirect or direct methods. In the study of DBD, an indirect technique could be working with materials containing an isotope in its composition that can undergo DBD, and then look for an excess of its daughter isotopes. The daughter nuclei can be analysed and accounted for, often by extracting accumulated gas in the material, as was the idea behind geochemical experiments [IR50]; or by using counters to detect the radioactive daughters of DBD in radiochemical experiments, such as the α particles released in the decay of ^{238}Pu [Xu+14]. The purpose of a direct method is to observe the two emitted electrons and retrieve information on the energy, timing and location of the event, and these detectors can be broadly classified in two categories: calorimeters, in which the source is encapsulated in the detector itself, and topological detectors in which the source and the detector are separate [Del+16].

Calorimeter Detectors

These include semiconductor detectors, low temperature bolometers, liquid or gaseous noble gas detectors, and liquid scintillators (LS) loaded with a $\beta\beta$ isotope. Some examples are illustrated in Figures 3.4 to 3.6. The main observable in calorimeters is the energy deposited by the electrons, and their detection is intrinsically highly efficient. They also offer excellent energy resolution, especially when using semiconductors or bolometers as they can reach $\sim 0.1\%\ FWHM$ [Del+16]. However, the energy readout is insufficient for particle identification and event topology reconstruction, meaning some experiments rely heavily on achieving low background levels [Saa13]. In contrast, liquid/gaseous noble gas detectors have some ability to reconstruct event topology, at the cost of having lower energy resolution [Del+16]. The feature of having the source coincide with the detection medium can also become a constraint when choosing which isotope to study. This is more relevant in the case of liquid noble gas detectors and semiconductors like HPGe (high-purity germanium) or CdZnTe (cadmium–zinc–telluride) because there has to be a big enough production and supply for the detector material [Del+16].

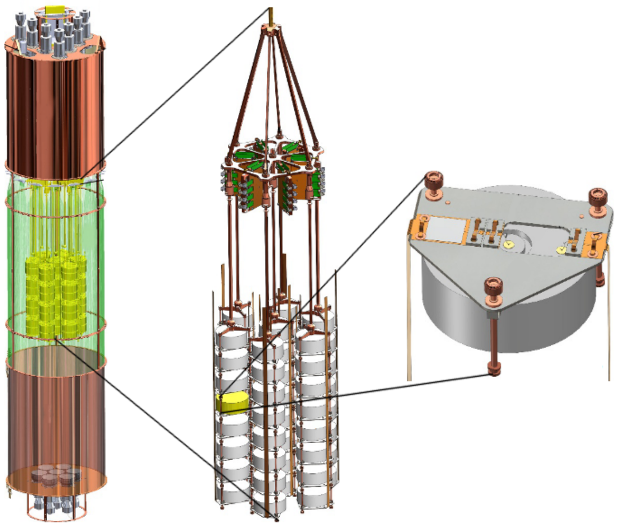

Figure 3.4: Example of a semiconductor detector, as implemented in the GERDA experiment, briefly discussed in section 3.2. Vertical arrays of HPGe detectors are arranged in seven strings and placed inside a LAr veto system. A bottom view of a single detector module is also shown. For reference of scale, the detector module on the right containing the Ge diode has ~73 mm in diameter and ~30 mm in height. Figure from [Col17].

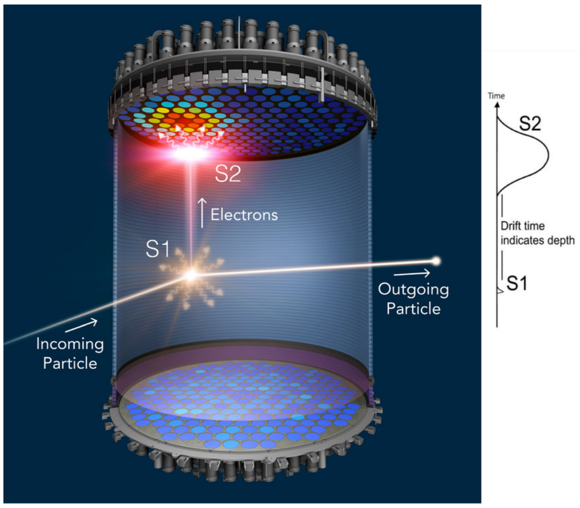

Figure 3.5: Example of a liquid noble gas detector, more specifically, a time projection chamber (TPC) with arrays of photomultiplier tubes (PMTs) at both ends of the chamber. This schematic is from the LZ experiment, discussed in section 3.2 [Mou+17].

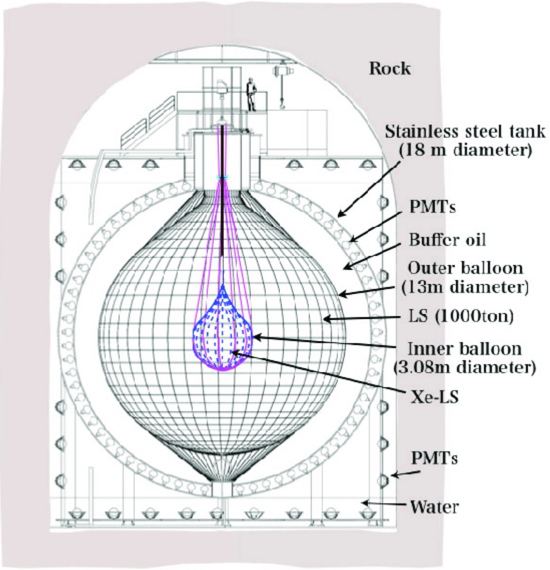

Figure 3.6: Setup example of a detector using LS loaded with a $\beta\beta$ isotope. The schematic is from the KamLAND-Zen experiment, discussed in the section 3.2 [Gan+16].

Topological Detectors

The most promising sensitivities for the NDBD half life derive from the calorimetric methods, and they have proven to deliver the best experimental results as well, so topological detectors will most likely not be the approach used in future neutrinoless experiments. Nevertheless, detectors with an external source are a valuable tool for DBD studies, and include solid state detectors, gas chambers, and scintillators [Del+16]. Figure 3.7 shows an experimental setup of the latter.

Usually the $\beta\beta$ source is surrounded by an array of detectors capable of identifying and reconstructing the individual tracks of electrons, which poses a great advantage for rejecting false NDBD interactions. This setup typically means the detectors are larger, have lower detection efficiency (around 30%), and a poor energy resolution ($\sim 10\%\ FWHM$) which does not favor separation between the DBD spectrum and possible NDBD events [Del+16]. The energy deposition in the source itself causes DBD to be the most limiting background, but this is compensated by the event reconstruction which improves SNR significantly [Saa13].Having a large isotope mass in this type of detector is a challenge due to self absorption, which is a major disadvantage as it decreases the amount of exposure of the experiment.

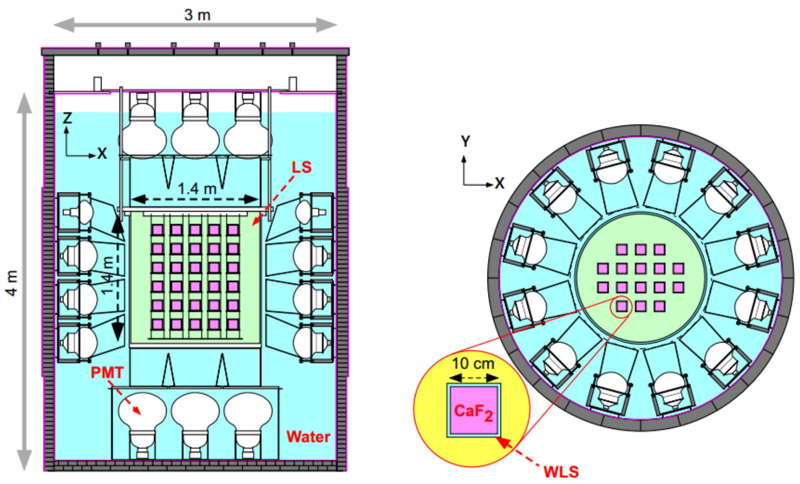

Figure 3.7: Example of a detector with scintillators. This setup belongs to the CANDLES-III experiment (side view and top view), featuring 96 CaF_2 crystal modules, a LS, a water tank, 62 PMTs, and external shields. More information on this can be found ahead in subsection 3.2.6. Image from [Aji+21].

3.2 Current and Future Experiments

In this section a review of current state of the art experiments is presented, highlighting the main features and sensitivities.

3.2.1 KamLAND-Zen

The KamLAND-Zen (KamLAND Zero-Neutrino Double-Beta Decay) experiment is an upgrade of the previous KamLAND detector which is looking for NDBD in ^{136}Xe. It is located in the Kamioka mine in Japan and it currently holds the title for the collaboration with the best results on the NDBD half-life.

The detection environment consists of an outer balloon (OB) and an inner balloon (IB) which is suspended inside the former by film straps. The OB is filled with 1 kton of LS and acts as a shield from exterior γ rays and as a detector for internal radiation. The IB is the main detection environment, containing 13 tons of xenon-loaded LS with an enrichment of $\sim 2.9\%$ by weight in xenon gas. The balloon apparatus is surrounded by a containment tank and a Cherenkov water detector for cosmic-ray identification, and PMTs installed all around the balloon collect scintillation light (see Figure 3.6 for more detail). Even though this type of experiment design and setup has lower energy resolution when compared to others, and does not provide information on event topology, it has the largest amount of the isotope of interest [Gan+16].

The experiment ran in three phases in order to improve sensitivity, material purity and eliminate some backgrounds. Phase I was completed after an exposure of 89 kg.year of ^{136}Xe as sensitivity was limited by an unexpected background of ^{110m}Ag, so a campaign of purification and calibrations ensued during 18 months. In Phase II the measured isotopic abundances were 90.77% for ^{136}Xe and 8.96% for ^{134}Xe which translates to a total amount of 380 kg of enriched xenon (345 kg of ^{136}Xe) [OO16]. This run lasted 535 days and they obtained an exposure of 504 kg-year of ^{136}Xe. Aside from ^{110m}Ag, other backgrounds worth noting were ^{134}Cs attributed to the Fukushima reactor accident, ^{214}Bi on the IB film, muon spallation products such as ^{10}C and ^{137}Xe, and DBD itself (Figure 3.8). The energy resolution at $Q_{\beta\beta}$ increased from 9.9% $FWHM$ (Phase I) to 11% $FWHM$ (Phase II) due to an increase in dead PMTs. Combining Phase I and Phase II results, gives a lower limit of $T^{0\nu}_{1/2} > 1.1 \times 10^{26}$ years at 90% C.L. [Gan+16], making it the first experiment to reach the limit of the quasi-degenerate mass region.

During Phase III, the collaboration rebuilt the IB with even cleaner materials to increase its capacity, now holding 745 kg of enriched xenon and an exposure of 970 kg.year of ^{136}Xe. The first data search of this phase obtained a sensitivity of $T^{0\nu}_{1/2} > 2.3 \times 10^{26}$ years at 90% C.L, which corresponds to a limit on the neutrino mass $m_{\beta\beta}$ of 36-156 meV [Zen22].
An upgrade to the detector is predicted for the future, KamLAND2-Zen will feature over 1 tonne of enriched xenon, and in order to improve energy resolution to be better than 6% $FWHM$, light concentrators, a brighter scintillator, and PMTs with higher quantum efficiency will be installed [OO16]. After 5 years of data taking the experiment will hopefully cover the full IH mass region [Gan+16].

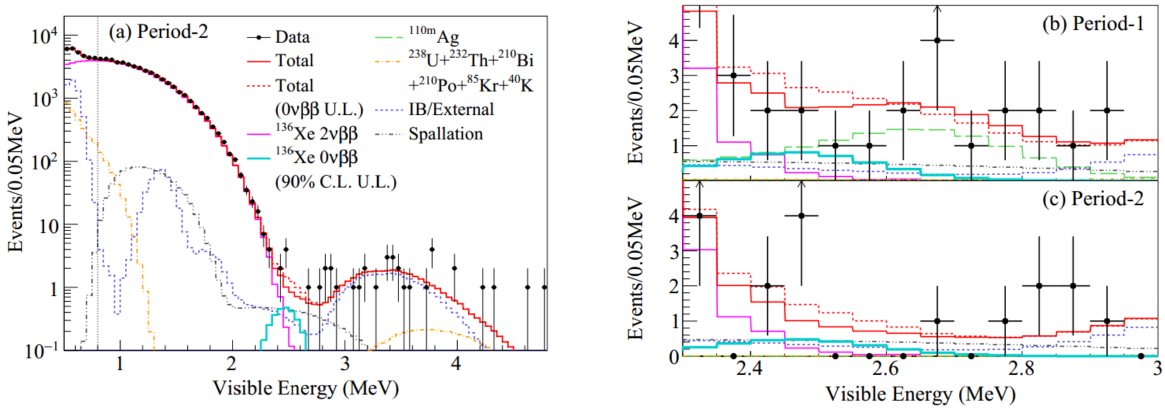

Figure 3.8: KamLAND-Zen results from data acquired during Phase II, which was divided into two equal time periods, each corresponding to one average lifetime of ^{110m}Ag. On the left, the energy spectrum of selected $\beta\beta$ candidates within a spherical volume of 1 m radius in Period 2, drawn together with best fit backgrounds. The DBD decay spectrum (solid pink line) and 90% C.L. upper limit for NDBD decay (solid light blue line) are also represented . On the right, a close-up energy spectra of the ROI, comparing both Periods. In the neutrinoless ROI, the background rate (solid red line) is very low and its reduction is clear from Period 1 to 2. Figure from [Gan+16].

3.2.2 EXO-200

The Enriched Xenon Observatory is located in a salt mine in New Mexico, USA. The detector is a cylindrical LXe time projecton chamber (TPC) with capacity for $\sim 200\ kg$ of enriched xenon ($\sim$ 81% is ^{136}Xe), where 110 kg are in the active volume. The cathode is installed in the centre of the chamber and each end has avalanche photodiodes (APDs) and anode wire grids to collect scintillation light and ionisation charge from the interactions, respectively. Each event has a two-signal signature which allows for better energy resolution compared to each channel individually and the energy of the event is retrieved by combining the information of these two signals [Col14].
The data acquisition stage was divided in two phases, spanning from 2011 to 2018, with an interruption between 2014-2016 due to an incident at the Waste Isolation Pilot Plant. Combining Phase I and II, they attained an exposure of 234.2 kg.year of ^{136}Xe and an energy resolution of $1.15\%/E$ in the NDBD ROI. The detection efficiency for NDBD reached 97.8% thanks to relaxation of selection criteria and deep neural network algorithms were used for signal discrimination [Ant+19]. As for backgrounds, the external most relevant observed isotopes were ^{232}Th, ^{238}U. The backgrounds coming from inside the TPC were ^{222}Rn, ^{60}Co, ^{137}Xe, neutron spallation γs and DBD decay [OO16]. The total combined limit for NDBD half-life is $T^{0\nu}_{1/2} > 3.5 \times 10^{25}$ years at 90% C.L. [Ant+19].

The next phase of the experiment, nEXO [Col+18], will operate with 5 tonnes of isotopically enriched LXe and the median 90% C.L. sensitivity is projected to reach $T^{0\nu}_{1/2} > 1.35 \times 10^{28}$ years, and a 3σ discovery potential of 0.74×10^{28} years after a 10 year run (Figure 3.10) [Adh+21]. The bigger size of the experiment is a major advantage to reduce external backgrounds through self-shielding, and nEXO is also planned to be deployed to a deeper location, which will help reduce the ^{137}Xe background produced cosmogenically [Col+17]. Some other upgrades to the detector will include moving the cathode to the end of the TPC, work on the radiopurity of components and improve energy resolution to avoid DBD from hindering the detection of a neutrinoless signal. To enhance the resolution, silicon photomultipliers (SiPMs, operated in Geiger mode) with a higher gain than the APDs (operated in the linear regime) used in EXO-200, will be installed in the lateral walls of the TPC which significantly improve light collection and reduce noise [OO16]. In the future, they also plan to use the technique of "Barium-tagging" through Single Molecule Fluorescent Imaging, to identify individual ^{136}Ba atoms produced in the $\beta\beta$ decay of ^{136}Xe to reduce the background even further [Car18].

3.2.3 NEXT

NEXT (Neutrino Experiment with a Xenon TPC) operates at the Canfranc Underground Laboratory in Spain, and is currently working under the stage called NEXT-WHITE or NEW, with the goal to assess the background model of the detector and study DBD. The detector is a high pressure gaseous xenon time projection chamber: a pressurized vessel at 10-15 bar holds a drift chamber inside with an active volume with capacity for 5 kg of xenon (and fiducial mass of 3.5 kg), where the electroluminescence light generated near the anode is recorded by a "tracking plane" of SiPMs and by an "energy plane" of PMTs behind the cathode [Alv+12]. Although it is difficult to reach a large exposure due to the low density of GXe, it has a smaller Fano factor than LXe, thus offering better energy resolution of $< 1\%\ FWHM$ at Q-value, and the choice to have separate detection systems for tracking and calorimetry provides access to the topological signature of the event. Under these pressure conditions, a NDBD can create a track up to ~ 15 cm long (in contrast to $\sim 2\ mm$ in LXe), and deposit most of their energy at both ends of the track, meaning the 2 electrons can clearly be set apart from backgrounds like ^{208}Tl and ^{214}Bi, in which the bulk of ionisation density is seen only at one end of the track (as shown in Figure 3.2) [OO16][Col+16].

During NEW, the measurement of the DBD half-life was calculated using a novel approach of direct background subtraction. There were two periods of data acquisition, one using ^{136}Xe-depleted xenon and the other with ^{136}Xe-enriched natural xenon, followed by two types of analysis. A background model-dependent analysis based on best fit values showed $T^{2\nu}_{1/2} = (2.03 \pm 0.56) \times 10^{21}$ years, and a background model-independent evaluation was done by directly subtracting the ^{136}Xe-depleted data from the ^{136}Xe-enriched data, arriving at $T^{2\nu}_{1/2} = (1.93 \pm 0.47) \times 10^{21}$ years. The values from both analysis are consistent, and combining them gives a half-life for DBD of $T^{2\nu}_{1/2} = 2.34^{+0.80}_{-0.46}(stat)^{+0.30}_{-0.17}(sys) \times 10^{21}$ years, compatible with results from other experiments [Col+21].

The near future of the experiment lies in the NEXT-100 stage, that will be dedicated to scale up the detector to employ 100 kg of xenon at 10 bar (or 150 kg of xenon at 15 bar) and study the NDBD of ^{136}Xe. According to NEW results, the expected background level is 4.29×10^{-4} (counts/(keV.kg.year)). Considering 5 years of data-taking, this places the sensitivity at $T^{0\nu}_{1/2} > 5.9 \times 10^{25}$ years, or in terms of Majorana neutrino mass, $m_{\beta\beta} < 70 - 130$ meV at 90% C.L. [Alv+12].

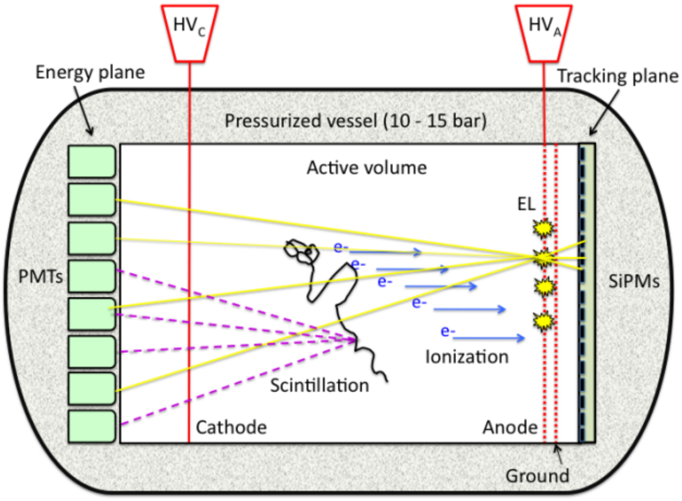

Figure 3.9: The Separate Optimized Functions (SOFT) concept in the NEXT experiment. The electroluminescence light collected by the plane of SiPMs is used for tracking particles, and the PMTs at the other end use the light signal for a precise energy measurement. Image from [Alv+12].

3.2.4 SNO+

SNO+ (Sudbury National Observatory) explores the facilities of its precursor experiment (the SNO neutrino experiment), at SNOLAB, inside a canadian mine in Sudbury. The detector consists of a 12 m diameter acrylic vessel filled with ~ 780 *tonnes* of liquid scintillator, surrounded by a geodesic PMT support structure ($\sim 36\ m$ in diameter), equipped with 9362 inward-facing PMTs and 91 facing outwards, to detect light from events inside the detector medium and external background events, respectively. The volume external to the acrylic vessel is filled with 7000 tonnes of ultra-pure water, providing shielding against external radiation [Pat19].

There are 3 stages to the experiment, each using a different detection medium and targeting different physics goals. The final phase is the one intended to study the NDBD of ^{130}Te, in which the scintillator will be loaded with 0.5% of ^{nat}Te, corresponding to about 1.3 tonnes of ^{130}Te. The internal background consists mainly of elastic scattering of solar neutrinos from ^{8}B, DBD, $^{238}U/^{232}Th$ chains and external γs. Under these conditions, the estimated sensitivity to NDBD is $T^{0\nu}_{1/2} > 2.1 \times 10^{26}$ years, which probes the Majorana neutrino mass between $m_{\beta\beta} < 37 - 89$ meV, considering a 5 year run and a 3.3 m fiducial volume. The decision on this isotope is supported by the fact that ^{130}Te has a high natural abundance, which eliminates the need for enrichment. The technique for loading the scintillator is also easily scalable, and a future increase in Tellurium concentration (up to 3%) could push the sensistivity to 10^{27} years [Fis18] [Alb+21].

3.2.5 LUX-ZEPLIN

Dedicated NDBD experiments are costly, and since there are already on-going highly sensitive, fully funded experiments studying other phenomena, it is practical to join two in a bigger synergetic collaboration which can provide competitive results [OO16].

One of the most promising candidates for this purpose is the LZ (LUX-ZEPLIN) experiment, which focuses on dark matter searches, specifically weakly interactive massive particles (WIMPS), and is located at the Sanford Underground Research Facility in South Dakota, USA. The detector is a dual-phase (with liquid and gas) xenon TPC, with a total of 494 PMTs distributed between the top and bottom of the chamber which collect the light from prompt scintillation (S1 signal) and secondary electroluminescence (S2 signal), as depicted in Figure 3.5. This setup allows for 3D position reconstruction and the deposited energy is retrieved from both S1 and S2 signals. Besides the internal background reduction due to xenon self shielding, the chamber is surrounded by two veto detectors from the innermost to outermost shield, starting with an instrumented xenon skin to veto γ-rays, followed by a Gadolinium-loaded LS outer detector with additional PMTs, which are crucial tools to reject interactions from radioactive backgrounds like neutrons and muons. The whole apparatus lives inside a water tank that serves as an instrumented shield from external backgrounds. The TPC features 7 tons of active ^{nat}Xe, which amounts to ~623 kg of ^{136}Xe in the active region without enrichment [Mou+17].

The extremely low background levels and large emitter mass grant good conditions for the study of NDBD. For the profile likelihood analysis to calculate the sensitivity of LZ, a low background fiducial volume was defined containing 5.6 tonnes of xenon in the centre of the TPC. The measured energy resolution is $0.65\%(\sigma)$ at $Q_{\beta\beta}$ [Per22a], but 1% is assumed for a conservative study. Sensitivity also depends on the discrimination between multiple scatter (MS) and single scatter (SS) events, and is dictated by the detectors' ability to spatially separate two interactions. NDBD events in LXe are almost point-like as the electron path is very short (~2 mm), so a SS is expected. The minimal vertex separation needed to reject MS events is assumed to be 3 mm in the z direction, and this effect on the *(x,y)* plane was not considered. Under these conditions, the background model points to 35.66 $counts/(kg.day)$ in the ROI [Ake+20b].

Depicted in Figure 3.11 is the projected 90% C.L. sensitivity of LZ, $T^{0\nu}_{1/2} > 1.06 \times 10^{26}$ years, corresponding to a Majorana neutrino effective mass of $m_{\beta\beta} < 53 - 164$ meV for 1000 days of data acquisition, or 1360 kg-year of exposure to ^{136}Xe. In the future, a dedicated search run with 90% enrichment in ^{136}Xe and the same amount of exposure could push the sensitivity up by an order of magnitude $T^{0\nu}_{1/2} > 1.06 \times 10^{27}$ years and $m_{\beta\beta} < 17 - 52$ meV [Ake+20b].

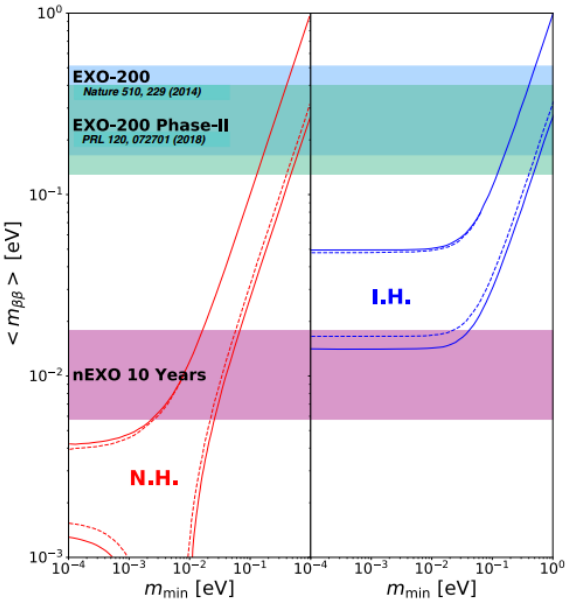

Figure 3.10: Comparison between the sensitivities of EXO-200 and nEXO at 90% C.L. for $m_{\beta\beta}$ as a function of the lightest neutrino mass for NH and IH. The width of the horizontal bands derive from the uncertainty in the nuclear matrix elements. Figure from [Col+17].

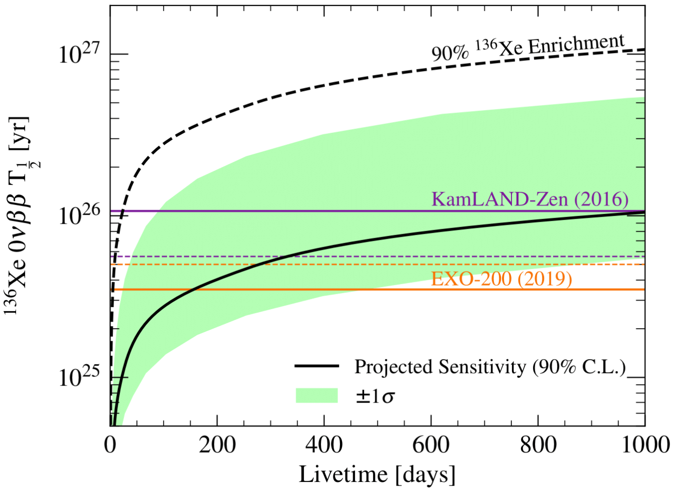

Figure 3.11: The solid black line is the LZ sensitivity projection in a 1000 day run for the half-life of NDBD decay in ^{136}Xe and the shaded green is the $\pm 1\sigma$ uncertainty. The dashed black line the LZ projection considering up to 90% ^{136}Xe enrichment. The results from KamLAND-Zen and EXO-200 are also plotted for comparison. Figure from [Ake+20b].

3.2.6 Other mentions

- The CANDLES-III experiment (CAlcium fluoride for the study of Neutrinos and Dark matters by Low Energy Spectrometer) is located in the Kamioka observatory in Japan. It uses 96 CaF_2 crystals with ^{nat}Ca, which amounts to 305 kg in total and corresponds to 350 g of ^{48}Ca. The detector consists of a water tank protected by an outer shield made of lead and Si sheets; inside the tank, the emitter crystals are immersed in a LS vessel, surrounded by an array of PMTs (see Figure 3.7). Even though ^{48}Ca has one of the lowest isotopic abundances from all NDBD candidates, it has the highest Q-value of them all, at 4.268 MeV, which places the signal above most backgrounds. The measured background rate was $\sim 10^{-3}$ events/(keV.(kg of ^{nat}Ca).years) in the ROI. The estimated detection efficiency is 35.7% and the energy resolution 2.4% $FWHM$ at $Q_{\beta\beta}$. After a run of 130.4 days, the results obtained for the lower bound on the NDBD half-life were $T^{0\nu}_{1/2} > 5.6 \times 10^{22}$ at 90% C.L. [Aji+21] [IID18].

- The GERDA experiment (GERmanium Detector Array) operates in Italy at the Gran Sasso Laboratory, and uses HPGe detectors isotopically enriched in ^{76}Ge to 87% [Ago+20]. During phase-I of the experiment, it reached an exposure of 23.5 kg-year while using 17.67 kg of mass of reprocessed detectors. This technique provided an energy resolution between 0.20% and 0.28% $FWHM$, a background rate of 11×10^{-3} counts/(keV.kg.year) at $Q_{\beta\beta}$ and a limit on the half-life of $T_{1/2} > 2.1 \times 10^{25}$ years at 90% C.L.. Phase-II of the experiment included an upgrade to BEGe (broad energy germanium) detectors which have a better resolution of 0.13% FWHM, and a LAr veto system, as seen in Figure 3.4 [OO16] [Ago+13]. This provided a decrease in the background rate to 5.2×10^{-4}

counts/(keV.kg.year) in the ROI, making GERDA the first experiment to reach the ZB regime, and the lower bound was set at $T_{1/2} > 1.5 \times 10^{26}$ years at 90% C.L. Combining the results of phase-I and phase-II, the total exposure amounts to 127.2 kg-year and the half-life of NDBD in ^{76}Ge is estimated to be $T_{1/2} > 1.8 \times 10^{26}$ years at 90% C.L., which coincides with the sensitivity assuming no signal was observed [Ago+20]. GERDA, along with the Majorana Demonstrator (an experiment which also used a similar approach with Ge diodes), joined to form a bigger collaboration and work on the LEGEND experiment (Large Enriched Germanium Experiment for Neutrinoless $\beta\beta$ Decay). It will operate in two stages, the first being LEGEND-200 featuring 200 kg of source mass, and the second LEGEND-1000 to reach 1 tonne of mass [Mys18].

- AMoRE-II (Advanced Mo-based Rare process Experiment) will be the third phase of a korean experiment which aims to study the NDBD of ^{100}Mo, with a fairly high Q-value of 3.035 MeV. Its operation is based on metallic magnetic calorimeters (MMCs) which measure temperature variations induced by energy depositions in $CaMoO_4$ crystals, operated at very low temperatures ($\sim$ 10 mK), as represented in Figure 3.13. In the future it will employ 200 kg of crystal mass, that should grant an energy resolution $<$ 10 keV in FWHM, and the background level in the ROI is expected to be $< 10^{-4}$ counts/(keV.kg.year). The projected sensitivity of a 5 year run is $T^{0\nu}_{1/2} \sim 1 \times 10^{27}$ years, and it is expected to reach the $m_{\beta\beta}$ limit of 20 meV [Bha+12] [Luq+17] [Kim+17].

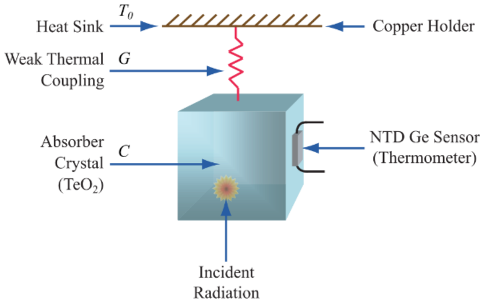

Figure 3.12: Schematic of a low temperature bolometer and its key components, as used by the CUORE experiment. Figure from [Nut+20].

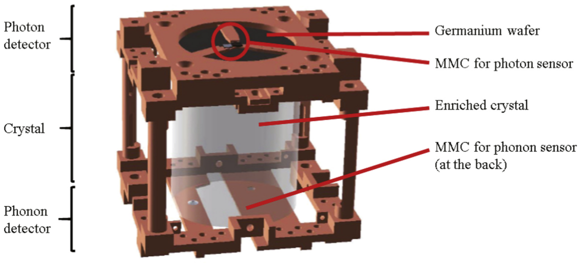

Figure 3.13: One of the detector modules used by the AMoRE experiment. It is composed of three main parts: a photon detector, a scintillating crystal and a phonon detector. Figure from [Kim+17].

Figure 3.14 summarises the fundamental sensitivity parameters for the experiments discussed in this chapter and many more, including future experiments as well.

Research on atmospheric ν so far point to the region of interest being below the IH band, meaning the mass hierarchy would be Normal, assuming the mechanism for NDBD is in indeed the exchange of a light neutrino. However, these experimental limits depend strongly on the theoretical model behind it, so it is important to develop the theory even further in order to avoid discrepancies between models and uncertainties in calculations [Bia17].

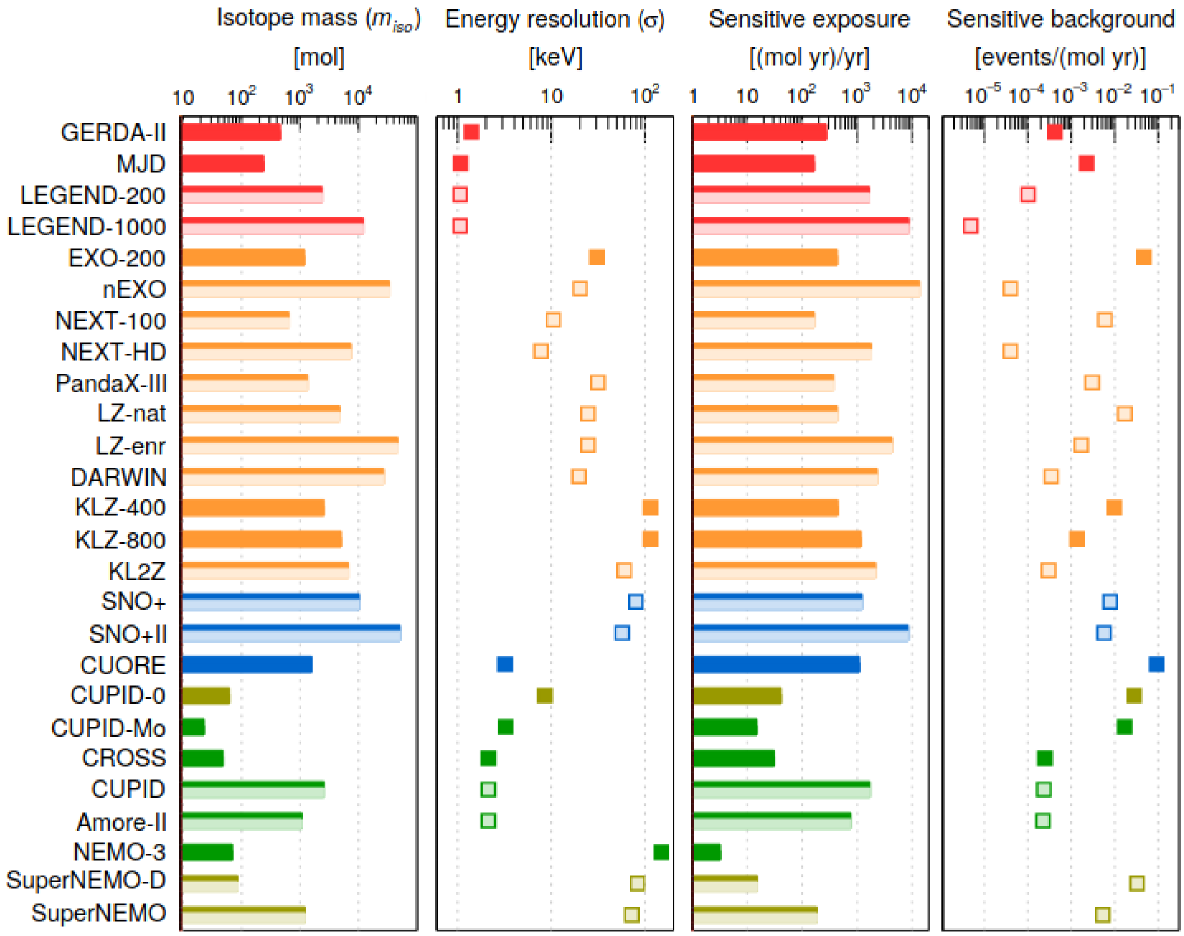

Figure 3.14: Fundamental parameters that define the sensitivity of recent (darker shades) and future experiments (lighter shades) researching NDBD. Red is representative of experiments using ^{76}Ge, blue for ^{130}Te, green for ^{100}Mo, orange for ^{136}Xe and sepia for ^{82}Se. Image adapted from [Ago+22].

Chapter 4

Xenon Dual-Phase Time Projection Chambers

In 1967, proportional scintillation in LXe was observed for the first time by Dolgoshein, Lebedenko and Rodionov [AD10]. Using a gas filled spark chamber, they looked to assess if it was possible to record the trajectory of ionizing particles in a noble gas, and noted that electrons produced by a charged particle passing through LXe had a sufficient long lifetime and could be accelerated by an electric field to energies high enough to excite the xenon atoms [DLR67].

In the following year, the development of the first multiwire proportional counter (MWPC) by Georges Charpak was of the utmost importance in the field of particle physics as this detector was the predecessor to drift chambers and later on time projection chambers, and he was awarded the Nobel Prize for his work on MWPCs in 1992. The MWPC consisted of an array of equally spaced and grounded anode wires placed between two cathode planes with negative potentials. The chamber was filled with an argon-heptane mixture between the two cathodes and the strong electric field allowed to amplify the signal and collect charges to obtain positional information by tracking the trails of gaseous ionization. The detector was directly connected to a computer which was crucial to significantly improve the speed of data collection, resulting in counting rates higher than 10^5 per second per wire [CHa+68].

Building on the work mentioned in the previous paragraphs, in 1974 Nygren proposed a detector capable of measuring momentum and position which he called the time projection chamber [Nyg74]. In 1977, Carlo Rubbia[1] extended this concept to be used with a liquefied noble gas, which resulted in the first liquid argon projection chamber [Rub77]. The first major application of a TPC was the PEP-4 detector which studied electron-positron collisions at SLAC (Stanford Linear Accelerator) [MN78] and the use of TPCs for DM studies was originally proposed by Barabash and Bolozdynya [BB89].

Time projection chambers use a sensitive volume that can be solid, liquid or gaseous to retrieve information on the *(x,y,z)* coordinates of the event from the combination of light and charge signals[2]. The previous detector technologies offered a *(x,y)* plane picture of the event meaning that it was only possible to reconstruct a few interactions, whereas the concept of a TPC allowed to break the event degeneracy in the z direction making it possible to distinguish particles with different linear energy transfer (LET) [Hil10].
The interaction volume of a TPC can be filled with an inert noble gas (e.g. xenon or argon) or liquid scintillators. If the detection medium is the same throughout the chamber then the

---

[1] Rubbia and Van der Meer received the Nobel Prize in 1984 for their decisive contributions through the UA1 experiment which led to the discovery of the W and Z bosons at CERN.

[2] The original TPC was operated with argon gas and recorded charge signals only.

detector is said to be single-phase, but if it has different states then it is called a dual-phase TPC which can be identified by two distinct phases (i.e. liquid/gas or solid/gas). A characteristic of TPCs that is crucial in particle identification is the use of electric fields, sometimes combined with a perpendicular magnetic field ($\vec{E} \perp \vec{B}$). The light/charge signals can be collected by using photosensors or electrode wires connected to RC circuits or even a composition of both.

TPCs are now a leading technology in particle physics as they provide a 3D picture of the interactions. Through event topology discrimination algorithms and position reconstruction capabilities, TPCs achieve excellent energy resolution and background rejection [AD10]. Dual-phase (liquid and gas) xenon TPCs have been particularly successful due to the vast amount of information encompassed in their signals, therefore this chapter focuses on this detector model, described with the technological choices that will be implemented in the prototype from Chapter 5.

4.1 Overview

These TPCs consist of a liquid noble gas target where an interaction can occur, above it is a gaseous phase where signal amplification takes place, and one or two photosensor arrays rest at each end of the chamber for signal detection. There are three main electrode grids woven from thin metal wires which are set at high voltages, these are responsible for applying electric fields in different regions of the chamber. The TPC walls are composed of field shaping rings that keep the field uniform in the longitudinal direction, and are covered by polytetrafluoroethylene (PTFE) reflector panels to improve light collection. An example of a TPC with this design, that of the LZ detector, is shown in Figure 4.1.
The field between the cathode grid at the bottom and the gate grid below the liquid surface defines the drift region (DR), where after an interaction, scintillation photons are created and ionisation electrons are released and transported towards the liquid surface. When they reach the LXe interface, the electrons are extracted to the GXe by a stronger electric field created between the gate and anode grids. This is the electroluminescence region (ELR), where a secondary light signal occurs only if electrons traverse to the gas. An additional two grids can be implemented if the photosensors are PMTs in order to protect them from high fields, one at the bottom below the cathode grid and another at the top located above the anode. The volume between the cathode and bottom grids is called the reverse field region (RFR) [Mou+17].

The photosensors installed on TPCs are commonly PMTs specifically targeted for cryogenic working conditions, recently SiPMs have also been considered as their characteristics have become increasingly competitive. These devices are manufactured with low radioactivity materials and the average quantum efficiency for the xenon scintillation light is usually between 30-40% for PMTs [Par+18] and 20-30% for SiPMs [Jam+18][Bau+18]. This is why the use of PTFE is extremely important, as it has a reflectivity of $\geq 97\%$ for xenon scintillation VUV photons when immersed in LXe [Nev+17].

These TPCs are housed inside a vacuum insulated cryostat vessel to maintain the low temperatures, the chamber also is connected to a purification system to remove electronegative impurities from xenon and there are systems in place to reduce radioactive contaminants such as ^{222}Rn, ^{85}Kr and ^{39}Ar, for instance through activated charcoal traps and gas charcoal chromatography [Mou+17].

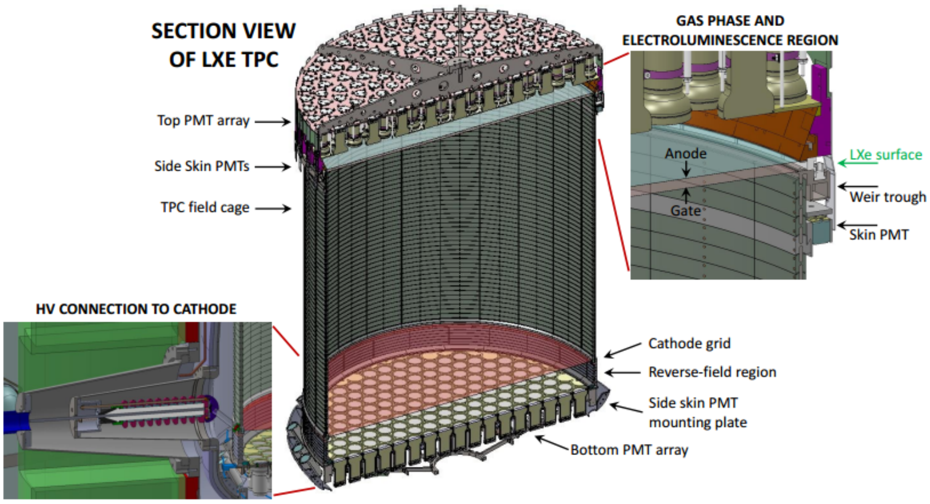

Figure 4.1: Schematic view of the LZ LXe TPC and its main components. Figure taken from [Mou+17].

4.2 Xenon Properties

Noble gases can be purified relatively easily and can be obtained in large quantities from the steel industry, as a result of liquid oxygen production since it needs to be separated from other gases present in the atmosphere [Ava+21]. Xenon, in particular, can be enriched with the isotope of interest to increase the exposure of the experiment and has several advantageous properties which makes it a suitable detection medium for ionisation detectors.

The high atomic number and relatively high density of LXe (see Table 4.1) allow for higher interaction rates and this also makes it a very efficient material to stop penetrating radiation [Apr+06b]. Figure 4.2 shows the stopping power of xenon for electrons as a function of energy, from which can be asserted that from the 0.8 MeV mark the stopping power increases rapidly, meaning that electrons with higher or lower energies will deposit their energy faster as they travel. Highly purified LXe is transparent to its own scintillation light, having a photon attenuation length in excess of 360 mm [Sol+04], but it also shields the detector from high energy photons. Figure 4.3 depicts the mean interaction length of photons in LXe, calculated from mass attenuation coefficients.

The self-shielding and high compressibility of xenon are great advantages as this means a LXe detector can be quite compact while still reducing the amount of backgrounds from neutrons and gammas in the central region of the detector (fiducialisation) [Mou+17]. Since the detector has ability to resolve interactions in 3D, if its size is larger than the mean interaction lengths for MeV γ-rays and neutrons, when these particles penetrate more than a few centimetres they scatter multiple times and are rejected in analysis. For example, γ-rays of 1 MeV have a mean interaction length of 6 cm in LXe, meaning that from that radial distance inwards, the detector is mostly "quiet" to photons of that energy.

Table 4.1 lists the natural isotopes of xenon with their respective abundances. The various isotopes undergo different processes making them appealing to many physics applications, for instance, ^{124}Xe is used to study double electron capture, ^{135}Xe (synthetic) is a common neutron poison in fission reactors, and double beta decay can be studied with ^{136}Xe and ^{134}Xe. Additionally, all natural isotopes are stable with the exception ^{124}Xe, ^{134}Xe and ^{136}Xe, and since their combined isotopic abundances are only about 20%, a detector that uses natural xenon should have very low radioactivity levels.

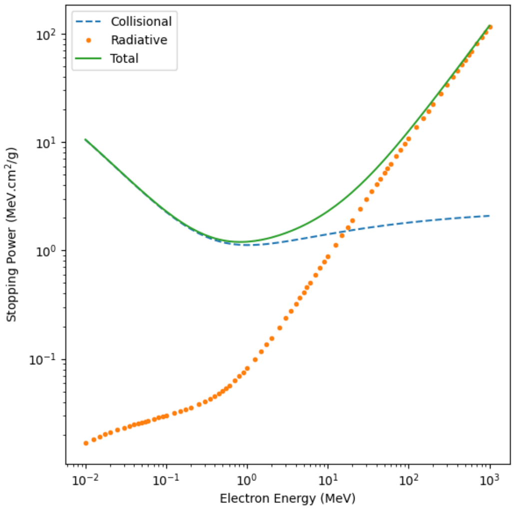

Figure 4.2: Stopping power of xenon as a function of electron energy [Ber+17].

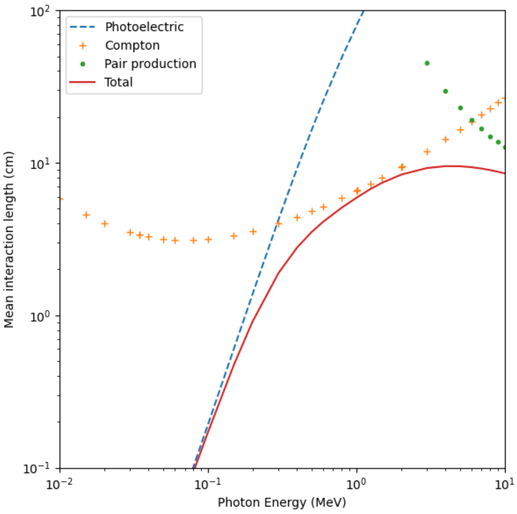

Figure 4.3: Mean interaction length of photons in LXe, for Compton scattering, pair production and photoelectric processes [Ber+10].

Understanding the electronic structure of noble gases is useful for studying the ionisation and scintillation processes that occur in TPCs. Absorption spectroscopy done on LXe, LAr and LKr has shown that these noble gases have an electronic band structure with considerable band gap energies (E_g), making them excellent insulators; LXe having the smallest gap energy of the three at 9.28 eV [Apr+06b]. Out of the rare gases used in experimental settings, LXe has the smallest W-value[3] at 15.6 eV and, as consequence, it features the highest ionization yield. Its W_{ph}-value[4] has been measured to be W_{ph} = 13.8 eV for LXe, giving it the highest scintillation yield[AD10]. It is also the fastest scintillator as the de-excitation of the dimer Xe$_2^*$[5] decays into a singlet in $\tau_S = 4.1$ ns and triplet state in $\tau_T = 21$ ns.

The electron mobility (μ_e) in LXe is high and comparable to that of Silicon, about 2000 cm^2/(V·s), which is important if one is interested in minimising the diffusion of charges in the drift region, which is discussed in the following sections [AD10].

The photoelectron yield in GXe depends on the extraction probability of ionization electrons, the electroluminescence gain, and light collection efficiency of photons generated in the ELR. For a small number of electrons extracted to the gas phase which produces a small secondary light signal, a photon yield of at least 50 photoelectrons per emitted electron is needed to accurately reconstruct the event [Mou+17]. Important physical properties of GXe and LXe are summarised in Table 4.2.

---

[3] Average energy expended to produce an ion pair.

[4] Average energy expended per scintillation photon.

[5] This dimer arises from direct excitation of xenon atoms and recombination.

Table 4.1: General information about xenon [AD10].

Xenon	
Isotopes	^{124}Xe (0.09%); ^{126}Xe (0.09 %) ^{128}Xe (1.92%); ^{129}Xe (26.44%) ^{130}Xe (4.08%); ^{131}Xe (21.18%) ^{132}Xe (26.89%); ^{134}Xe (10.44%) ^{136}Xe (8.87%)
Atomic Number Z	54
Atomic Mass A	131.30

Table 4.2: Physical properties of LXe and GXe as a detection medium [AD10].

Property	**Value**
Gaseous Xenon	
Density (at boiling point)	0.0169 g/cm^3
Ionisation potential	12.13 eV
W-value	22.0 eV
Liquid Xenon	
Density (at boiling point)	2.942 g/cm^3
Gap energy	9.28 eV
W-value	15.6 eV
Scintillation wavelength (λ_{sc})	177.6 nm (6.93 eV)
Dielectric const.	1.95
Refraction index (at λ_{sc})	1.69 [Sol+04]
Thermal conductivity	16.8×10^{-3} cal/s cm K
Heat capacity	10.65 cal g/mol K
Electron mobility	2000 cm^2/(V·s)
Ion mobility	3.6×10^{-3} cm^2/(V·s)
Threshold $\vec{E}$ for electron multiplication	1-2$\times10^6$ V/cm
Threshold $\vec{E}$ for electroluminescence	4-7$\times10^5$ V/cm

LXe detectors have been impactful in many areas of research, including gamma ray astrophysics, dark matter detection, particle physics and medical imaging [AD10]. Some applications include Compton telescopes [Apr+00], direct detection of dark matter, neutrinoless double beta decay searches, study of neutrino properties, ionisation calorimeters, study of the $\pi \rightarrow \mu\nu\gamma$ decay [Car+96] and $\mu \rightarrow e\gamma$ decay [Gal+14], Compton positron emission tomography (PET) [Che+02] and time-of-flight PET [Fer18].

4.3 Working Principle

Figure 4.4 summarises how deposited energy in xenon is partitioned and Figure 4.5 illustrates the process of signal formation in a LXe TPC, described in this section. In the active volume of a TPC, a particle can interact with a xenon nucleus or with an atomic electron, producing a nuclear recoil (NR) or electronic recoil (ER) respectively. Part of the energy excites the medium generating scintillation light and the remaining is spent on ionisation, although a fraction goes to heat. The prompt scintillation light is released by excited dimers with a characteristic wavelength in the VUV region and it is detected by the top and bottom photodetectors, creating the S1 signal. In the absence of an electric field, most electrons recombine near the interaction site. Meanwhile, even in the presence of an electric field some ionisation electrons recombine with the xenon ions which subsequently suffer de-excitation, contributing to the S1 signal.
The electrons that escape recombination are removed from the interaction site and drifted in the opposite direction parallel to the field, following the drift field lines. During their journey electrons can be captured by electronegative impurities (e.g. oxygen and water) in the liquid, thus the electron lifetime dictates the amount of charge that reaches the surface.

When the charges reach the gate grid where the field is stronger, they are accelerated towards the LXe surface where a fraction of them is extracted into the gas phase and then further accelerated by the high electric field. As the electrons move through the gas, energy is deposited leaving a trail of excited xenon atoms along their path which in turn emit photons in a phenomenon called electroluminescence. This produces a large amount of light that constitutes the S2 signal and it is proportional to the number of extracted electrons. As a consequence of total internal reflection in the liquid-gas interface, the majority of the S1 light is detected by the bottom array, and the top array mostly collects the S2 light.

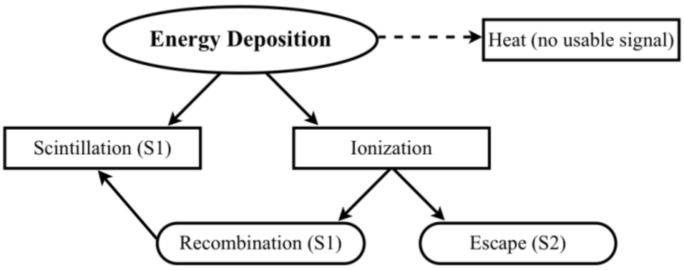

Figure 4.4: Schematic of processes that occur after energy deposition in a noble gas medium by a recoiling species. As described in the text, an interaction can transfer energy to produce scintillation, ionisation, and heat. After ionisation some electrons might recombine with xenon ions, forming excimers that decay to the ground state by emitting light which contributes to the S1 signal. In the presence of an electric field, the electrons that escaped recombination move towards the gas phase where a higher field generates electroluminescence light, forming the S2 signal. Figure adapted from [Szy+11].

As previously mentioned, one of the main advantages of the TPC is the ability to do 3D event reconstruction. The intensity and distribution of light from the S2 signal throughout the top photosensors is used to reconstruct the *(x,y)* position of the interaction; this can be achieved, for example, with light response functions (LRFs) of the photosensors, further explained in Chapter 6. This light "map" (as in the PMT array from Figure 4.5) translates the position of the electron cloud that was extracted into the gas, and the initial coordinates can be inferred from the *(x,y)* in the gas phase.

The z coordinate of the interaction is determined from the time difference between the S1 and S2 signals (shown on the right of Figure 4.5), the electron drift velocity in LXe under the applied electric field and additional factors to correct for the possible non-uniformity of the field lines.

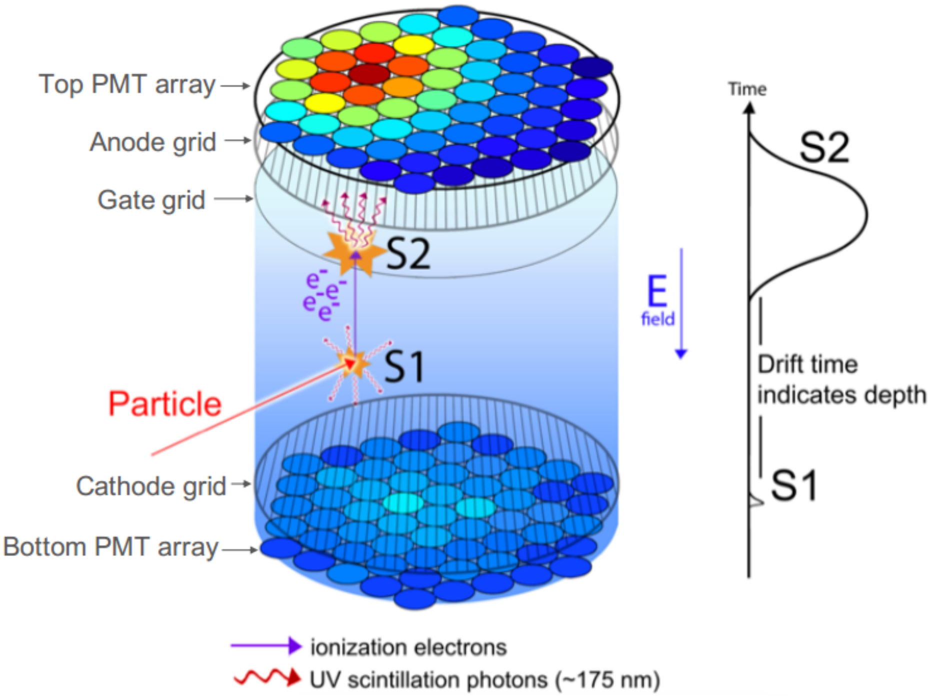

Figure 4.5: Illustration of the main components in a dual-phase TPC and its operation principle. On the right hand side is a simplified drawing of a typical signal: a small S1 peak triggered by prompt scintillation in the liquid, and a larger and broader S2 peak is the result of electroluminescence light from the diffused electrons which were extracted to the gas. Figure adapted from [Ake+13].

4.4 Scintillation and Ionisation Yields

In rare gases, the deposited energy E_{dep} in a single interaction is divided between excitation, ionisation and sub-excitation electrons, described by an energy balance equation, also known as Platzmann equation [AD10]:

$$E_{dep} = N_{ex}E_{ex} + N_iE_i + N_i\epsilon \tag{4.1}$$

where E_i is the average energy expended per pair, N_i the number of electron-ion pairs, E_{ex} is the energy needed to create an excimer, N_{ex} the number of excimers, and ϵ is the average kinetic energy of sub-excitation electrons.
The W-value is the average energy required to produce an electron-ion pair and can be taken from $W = E_{dep}/N_i$:

$$W = E_{ex}\frac{N_{ex}}{N_i} + E_i + \epsilon \tag{4.2}$$

where $N_{ex}/N_i \equiv \alpha$ is the exciton-to-ion ratio.
Considering the fact that LXe has an electronic band structure, Equation 4.1 can also be rewritten as 4.3. This ratio W/E_g is about 1.6 for LXe as well as for LAr and LKr, which supports the theory for the electronic band structure in liquefied rare gases [AD10].

$$W/E_g = \frac{N_{ex}}{N_i}\frac{E_{ex}}{E_g} + \frac{E_i}{E_g} + \frac{\epsilon}{E_g} \tag{4.3}$$

Equation 4.1 can be simplified by absorbing the influence of sub-excitation electrons into an average W-value $\overline{W} = (\alpha E_{ex} + E_i)/(1+\alpha)$, and assuming that nearly all excimers and recombined electrons lead to S1, results in Equation 4.4 [Szy+11].
The expected number of scintillation quanta n_{ph} is the sum of the initial photons from excitons and the number of electron-ion pair recombinations. The expected number of charged quanta n_e decreases by the amount that suffered recombination. These are respectively given by Equations 4.5 and 4.6 [Szy+11]:

$$E_{dep} = \overline{W}(N_{ex} + N_i) \tag{4.4}$$

$$n_{ph} = N_{ex} + rN_i \tag{4.5}$$

$$n_e = N_i(1 - r) \tag{4.6}$$

where r is the recombination probability which depends on electric field and on the energy loss per unit length.

The S1 and S2 signals are measured in terms of *phd* (photons detected) and depend directly on g_1, the photon detection efficiency of the detector, and g_2, the number of photons detected deriving from one ionisation electron removed from the interaction site (effective charge gain). The former can be calculated from the product between the light collection efficiency of the detector and the photodetector quantum efficiency so that $S1 = n_{ph} \cdot LCE \cdot QE$. The latter is the effective charge gain and depends on the electron extraction efficiency ϵ_e, on the number of photons produced by a single electron in the gas SE_{yield} and on g_{1gas} which is the average number of photons detected per photon that was emitted in the gas. The S2 signal can therefore be inferred from $S2 = n_e \ \epsilon_e \ SE_{yield} \ g_{1gas}$ [Brá20].

The deposited energy in the detector is related to the S1 and S2 signals, so the reconstructed energy of the interaction can be obtained from Equation 4.7.

$$E = \overline{W}\left(\frac{S1}{g_1} + \frac{S2}{g_2}\right) \tag{4.7}$$

The theoretical energy resolution of a LXe detector (assuming 100% collection efficiency for ionization electrons and scintillation photons) is given by Equation 4.8 in terms of FWHM, where F is the Fano factor. However, the experimental resolution usually disparates from that value, this spread is attributed to fluctuations in the number of secondary particles that are able to continue ionising the medium [AD10].

$$\Delta E(keV) = 2.35\sqrt{F \cdot W[eV] \cdot E[MeV]} \tag{4.8}$$

In order to achieve the best resolution possible, the loss of charge carriers needs to be minimised by avoiding impurities in the medium, by applying a high enough electric field so that the electrons and ions created have a smaller probability to recombine and by maximising the photon detection efficiency. Figures 4.6 and 4.7 show the variation of recombination probability at different energy ranges.

4.5 Electron drift and diffusion

The motion of charge carriers subject to a field in gas or liquid depends on their drift velocity, diffusion, and fluctuations due to gain or loss of electrons to ionisation or electronic attachment. This has been studied as a function of temperature, field strength and impurity concentration by many authors [AD10].
In the absence of an electric field, electrons are in thermal equilibrium with the medium, they move isotropically according to a diffusion coefficient D from the Einstein relation in Equation

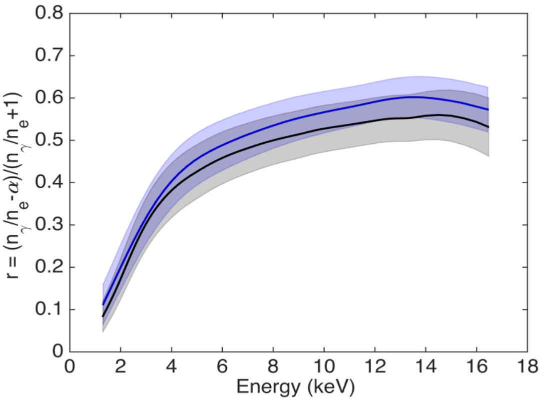

Figure 4.6: Recombination probability of low energy ER events in LXe, from NEST models, adjusted to LUX data. The black line is for a simulated field of 180 V/cm and the blue line is for 105 V/cm, with $\alpha = 0.2$. Image from [Ake+16].

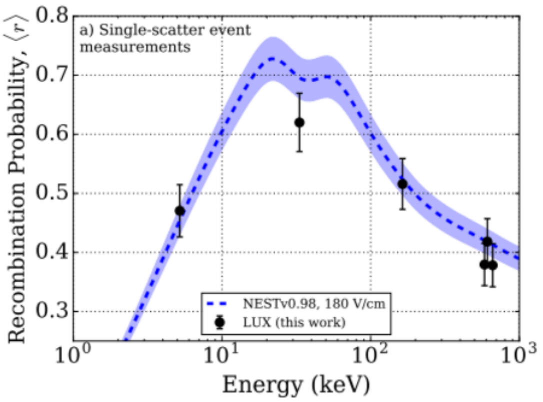

Figure 4.7: Measurements by the LUX experiment of the recombination probability at different energies, for single-scatter events. The dashed blue line is the mean recombination predicted by empirical models in NEST (Noble Element Simulation Technique). Image from [Ake+17].

4.9 in which k_B is the Boltzmann constant, T is the temperature of the medium and e is the electron charge.

However, if an electric field is applied, the motion behaviour is anisotropic: the charges are accelerated between collisions and drift along the electric field lines, in the same direction (opposite direction) to the electric field in the case of positive (negative) charges. Their velocity is almost proportional to the field with the mobility μ_{e0} (for $\vec{E} = 0$) as a constant, and is given by Equation 4.10 where m_e is the electron mass and τ is the average time between collisions [CA13]. At fields higher than 100 V/cm, the electron mobility deviates from the nominal value μ_{e0} and the drift velocity saturates, as seen in Figure 4.8.

$$D = \frac{k_B T \mu_{e0}}{e} \tag{4.9}$$

$$\vec{v_d} = \frac{e\tau}{m_e}\vec{E} = \mu_{e0}\vec{E} \tag{4.10}$$

As it moves, the cluster of electrons suffers diffusion in the longitudinal (D_L) and transversal (D_T) directions, spreading out to form a cloud. In cold rare gases $D_L < D_T$ under a large field, and in LXe the ratio is $D_L/D_T \sim 0.1$ for fields larger than 1 kV/cm [AD10]. The spread of an electron cloud can be described through a Gaussian distribution due to the random collisions in the medium. The width of the cloud after t seconds of formation and travelled distance d is expressed by Equation 4.11, valid while drift velocity is unsaturated [Hil10].

$$\sigma(t) = \sqrt{2Dt} = \sqrt{\frac{2k_B T d}{e|\vec{E}|}} \tag{4.11}$$

The diffusion progresses from the interaction point up to the anode, so the further away the interaction occurs from the anode, the wider the cloud becomes. This significantly affects spatial resolution as the light signals in the top array will be recorded over a wider number of photosensors, making reconstruction less precise. However, the problem of diffusion can be reduced by applying stronger fields as shown in Figure 4.9.

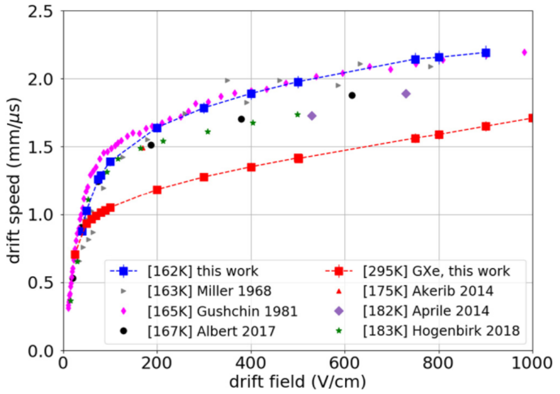

Figure 4.8: Results from several authors showing the dependence of electron drift velocity in LXe with the drift field. The values for GXe are plotted in red squares for comparison. Figure from [Njo+20].

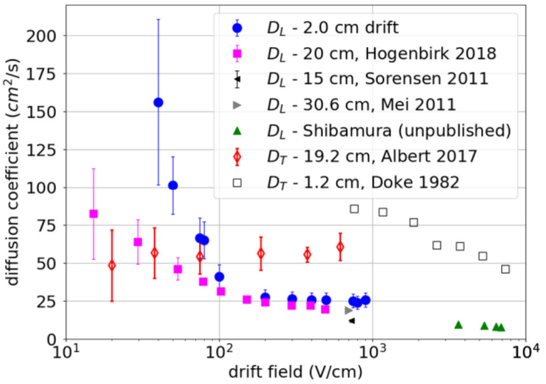

Figure 4.9: Diffusion coefficient measurements in LXe as a function of drift field. Figure from [Njo+20].

4.6 Discrimination of Electronic and Nuclear Recoils

Studying the discrimination power of a TPC is crucial to understand how some detector parameters affect the overall sensitivity of the detector. By combining the light and charge signals it is possible to obtain two data populations that distinguish between ER and NR interactions, since the α ratios are different: their values are approximately $\alpha \approx 0.06$ (min.) - 0.2 (max.) for ER and $\alpha \approx 1$ for NR at a field of 12.7 kV/cm [Dok+02]. Overall, NR expend more energy to the S1 signal while in ER a larger fraction of the energy contributes to the S2 signal [Ake+20a]. In Figure 4.11 there is a clear separation of the ER and NR bands, where for a large S1 the corresponding S2 is small.

Considering that the prompt scintillation fraction for S1 is small, the partition of the electron population between the processes of recombination and escape dictates the energy dependence of the S1 yield. Furthermore, because an electron lost to recombination cannot escape to the gas phase and vice-versa, the S1 and S2 signals are strongly anti-correlated [Szy+11]. This can be seen in Figures 4.10 as the ER charge yield increases at the same rate that the ER light yield decreases. For a given S1 energy, the corresponding S2 can have a wide range of energies, of which a broad region of events corresponds to ER (this is related to the energy of the event and recombination rate) and a smaller region comes from NR. Therefore, applying a stronger electric field would disperse electrons from atoms and ions, reducing recombination and improving discrimination as well.

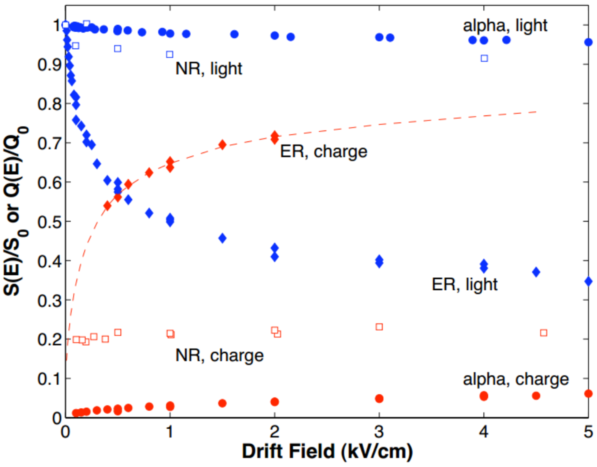

Figure 4.10: Field dependence of scintillation and ionisation yields in LXe. The blue diamonds refer to the ER scintillation yield while the red diamonds are for ER charge yield. Figure from [Apr+06a].

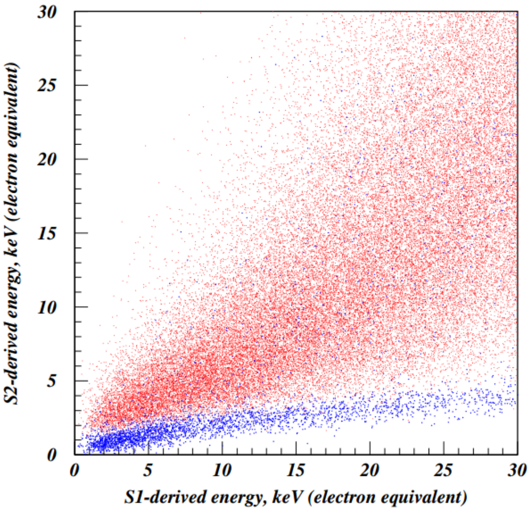

Figure 4.11: Scatter plot of S2 versus S1 scintillation for electronic recoils (population in red) and for nuclear recoils (blue). This data is from ZEPLIN-III calibration runs at 3.9 kV/cm drift field in LXe [CA13].

Chapter 5

R&D for a 3^{rd} Generation Detector

A 3^{rd} generation experiment refers to the future 50 to 100 tonne-scale detectors which will have advanced capabilities in various rare physics searches, as some discoveries lie beyond the reach of current tonne-scale experiments [Aal+22].
For instance, the present best sensitivity on spin-independent WIMP-nucleon scatter cross-section is estimated to be $1.5 \times 10^{-48}\text{cm}^2$ for a 50 GeV/c^2 WIMP with a 7 tonne LXe TPC [Ake+20c]. Nonetheless, the ultimate goal is to scan the entire range of WIMP scatter cross-section down to the neutrino "fog" [OHa21]. This introduces a constraint on the sensitivity since coherent nuclear scattering of ν_{atm} with xenon atoms are indistinguishable from a WIMP signal. A future 40 tonne detector will approach this limit, having a projected WIMP sensitivity of 2.5×10^{-49} cm^2 and at 50 GeV this neutrino background corresponds to $\sim 10^{-49}$ cm^2 [Aal+16].

Furthermore, if NDBD is not detected during the searches already in progress, it is possible that the half-life of the decay falls above the $T^{0\nu}_{1/2} \sim 10^{27}$ years limit. This next generation of detectors will be competitive against other dedicated experiments searching for NDBD, which regardless of the decay mechanism prevails as an important process to possibly study lepton number violation, sterile neutrinos and other extensions to the SM [Ava+21].
This motivates the construction of larger detectors to house dozens of tonnes of xenon that would enable to enhance the discovery potential and sensitivity to NDBD in ^{136}Xe. If possible, it is also advantageous to conduct several physics studies in the same detector, thus the concept of existing LXe TPCs used in dark matter experiments will be scaled up and improved to reach a competitive sensitivity limit in the study of NDBD and the neutrino magnetic moment, without impacting the ongoing WIMP searches [AAa21].

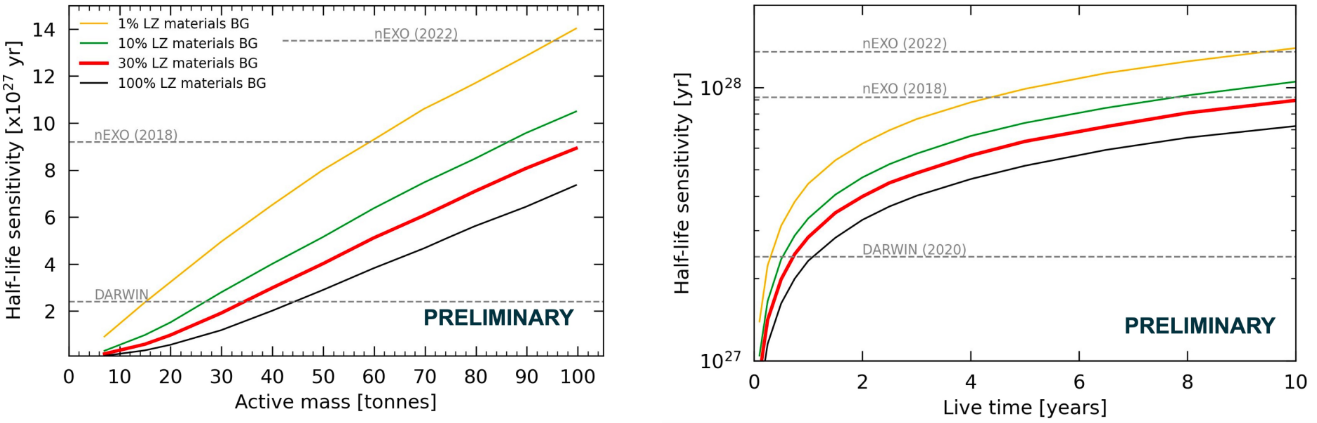

Figure 5.1: Estimated half-life sensitivities as function of active mass (left) and as a function of data acquisition live time (right), for a 3^{rd} generation detector with varying γ-ray background (percentages relative to the total amount of background in the LZ experiment) [LO22].

In order to probe most of the allowed parameter space for NDBD, a detector should reach a sensitivity of $\langle m_{\beta\beta} \rangle \sim 1$ meV, which corresponds to a half-life of 10^{30} years, for which it would require several kilotonnes of target mass [Ava+21]. For the moment, preliminary studies for a 3^{rd} generation experiment such as the one from Figure 5.1 indicate that a TPC with 100 tonnes of active mass (9 tonnes of ^{136}Xe) could reach a sensitivity of $T^{0\nu}_{1/2} = 8.9 \times 10^{27}$ years with a 10 year long exposure [LO22]. The biggest challenge in carrying out such an experiment lies in acquiring large amounts of xenon, which are currently unattainable since the available production methods are limited and expensive. Xenon is usually extracted from the atmosphere via cryogenic liquefaction followed by distillation. By pairing this with alternative techniques such as non-cryogenic xenon adsorption (pressure, vacuum or thermal swing adsorption) it would be possible to meet the required acquisition rates, giving good prospects to this next generation of detectors [Ava+21].

Illustrated in Figure 5.2 is Xenia, a small dual-phase LXe TPC prototype being developed to perform R&D studies towards the optimisation of a 3^{rd} generation detector for NDBD searches. The active volume in Xenia will be a cylinder with 8 cm in diameter and 8.5 cm long, corresponding to 1.2 kg of active LXe mass. Four square 1-inch PMTs will be installed at the bottom of the chamber, and a 64 photosensor array at the top, both looking into the active volume to detect xenon luminescence (initially a 2-inch PMT will be installed and later replaced by the SiPM array).

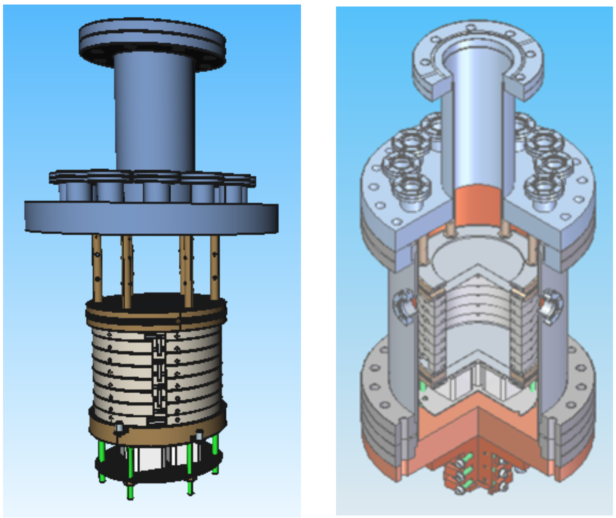

Figure 5.2: Exterior and interior view of the Xenia detector in its initial stage with room for one PMT at the top. The design of Xenia is versatile and will allow to install either a PMT or the SiPM array at the top. CAD courtesy of E. Holtom, Rutherford Appleton Laboratory.

The discrimination of possible neutrinoless events requires a higher level of granularity in terms of space than PMTs usually offer. The signal used for *(x,y)* reconstruction of events is the S2 acquired from the top array and the z coordinate is only dependent on the temporal separation of S1 and S2; additionally the smaller S1 signal is mostly detected by the PMTs which collect more light as they have no recovery time and are larger in area. Therefore, PMTs are used for time performance and SiPM for spatial granularity, which is why the configuration of PMTs in the bottom and SiPMs in the top array is preferred should SiPMs be used in a large experiment.

5.1 Xenia Simulations

The simulated detector geometry consists of a cylindrical chamber with 114 mm outer diameter and with a total height that will vary between 118 mm and 143 mm in the simulations, depending on the test parameters. The dimensions of the active region are 80 mm in internal diameter and 85 mm in height. The reflectivities of the main components are mostly set to 97% (i.e. all PTFE elements immersed into LXe) or 0% (i.e. Kapton elements and blackened copper), unless indicated otherwise; these are good approximations for the xenon VUV luminescence. With reference to Figure 5.3, the chamber is composed by various stacked volumes which are now described, from top to bottom.

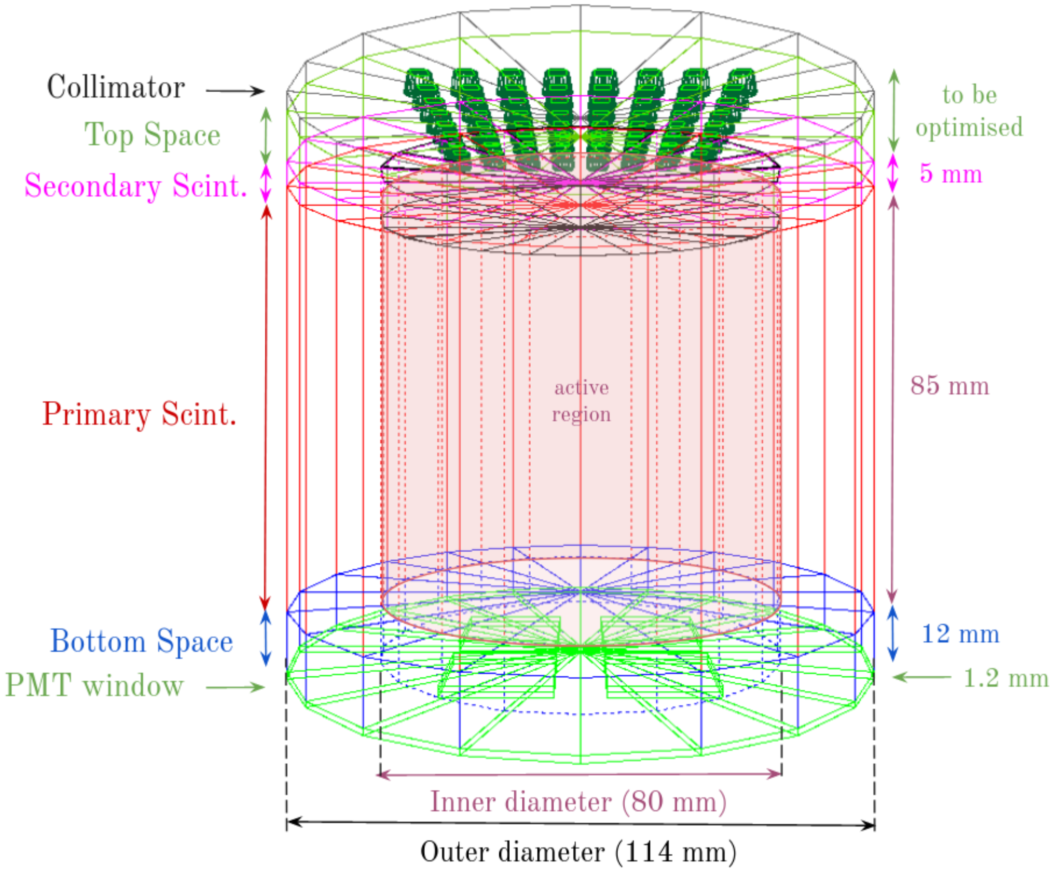

Figure 5.3: Full chamber geometry of the Xenia detector used in the simulations.

At the top of the chamber sits an array of 64 SiPM devices as shown in see Figure 5.4. The sensor parameters (dimensions, number of pixels, PDE) considered in the simulation correspond to two models: Hamamatsu S13370-3075CN or S13370-3050CN [Pho17], more details on these devices are provided in Chapter 6.

The photosensor array is supported by the structure of the collimator which has 64 apertures, with axes aligned with the centres of the SiPM active areas. The SiPM front surfaces are located at the exit aperture of the collimator. The collimator material has zero reflectivity (blackened copper), and is surrounded by GXe.

Immediately below is the Top Space region, in the simulations this will be a volume of variable height, 114 mm diameter and lateral walls are coated in a Kapton skirt. The anode grid is located at the interface between this Top Space and the Secondary Scintillation volumes (Secondary Scint), with 20% reflectivity considered for the stainless steel wires, other grid properties such as the pitch, transparency and wire diameter are not fixed and will be tested in the simulations as to find the optimal parameters from commercial options. The volume denominated Secondary Scintillation is the electroluminescence region with 5 mm height and the diameter tapers in to 80 mm. From the Secondary Scintillation region (included) upwards, the active area of the stacked volumes are filled with GXe; below that region all other active volumes contain LXe. The LXe optical properties were defined at 175 nm with refractive index equal to 1.69, Rayleigh mean free path of 300 mm, bulk absorption of 3.3×10^{-5} mm^{-1}, and at the interface with PTFE we set 97% Lambertian scattering and 3% absorption.

The drift region corresponds to the 85 mm long Primary Scintillation (Primary Scint) volume containing LXe bounded by the PTFE fieldcage of unity reflectivity. The gate grid sits 5 mm below the surface of the liquid, with properties to be tested.
The Bottom Space is equivalent to a reverse field region of 12 mm height and diameter of 80 mm with PTFE walls to help collect as much light as possible.
The cathode is located at the interface between the drift region and the Bottom Space and the bottom grid is set just on top of the PMT window. There is a small volume before the photosensors which acts as the PMT window, these are 1.2 mm thick quartz windows.
The PMT array is the last component of the chamber and contains four 1-inch Hamamatsu R8520 phototubes [Pho21] (see Figure 5.5) and the remaining bottom surface of the chamber is PTFE.

The simulations implement a uniform electric field inside the chamber by using the corresponding electron drift velocities throughout the calculations of electron diffusion. The electric field is divided into three regions:

- Field between cathode and gate grids (80 mm) - 380 V/cm
- Field from gate to the LXe surface (5 mm) - 5 kV/cm
- Field from the LXe surface to the anode grid (5 mm) - 10 kV/cm

The electrode grids at the top of the chamber can affect spatial resolution, so the gate and anode were considered in the simulation. During the optical optimisation studies three grids were tested, and their characteristics are described in Table 6.1. Afterwards, only the best combination of gate and anode grids were used throughout the remaining simulation work.

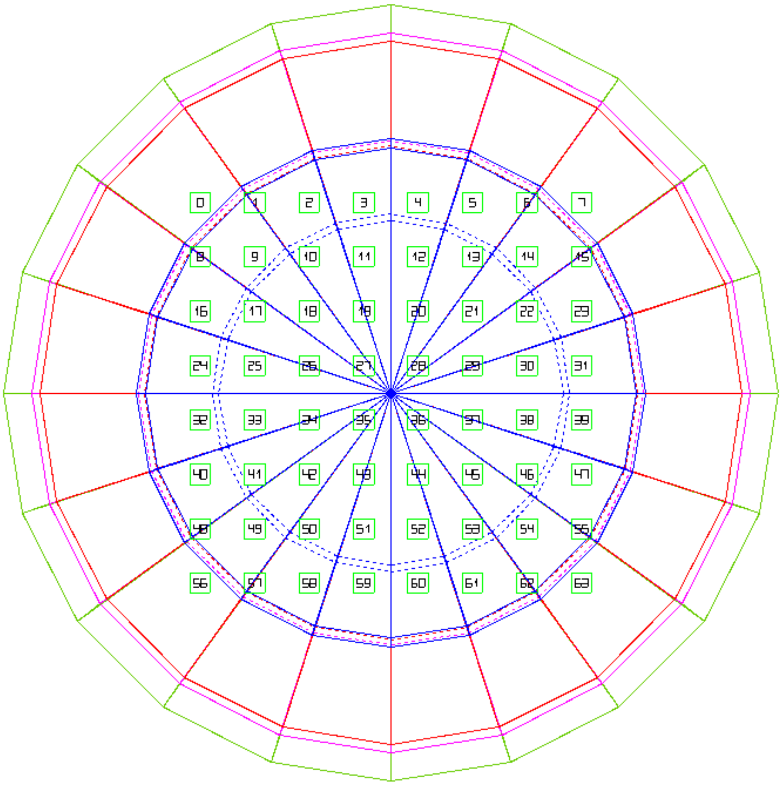

Figure 5.4: Top view of the Xenia SiPM array and indexation of each photosensor. The simulated geometry is composed of several cylinders and this top view should be seen as a series of circumferences; the apparent polygon faces in this image are simply a limitation of the visualisation software. The solid blue circumference represents the limits of the inner chamber volume which is filled with LXe. The solid pink circumference corresponds to the outer diameter of the Secondary Scintillation region, filled with GXe.

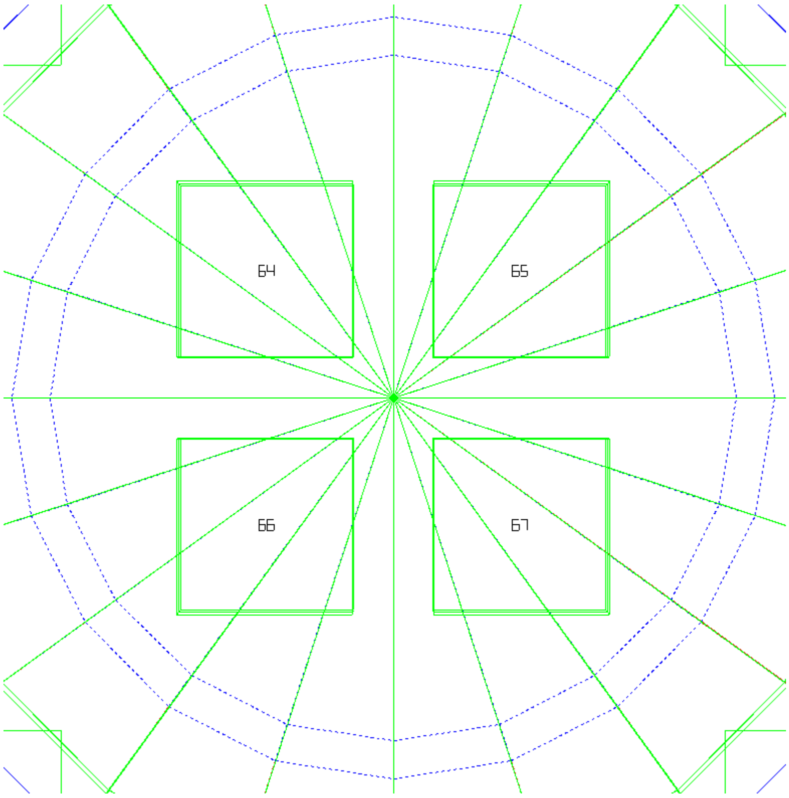

Figure 5.5: Top view of the Xenia PMT array and indexation of each device.

5.2 Key characteristics of the prototype

5.2.1 Silicon Photomultipliers

The main function of the SiPM array is to read out the electroluminescence light (S2) generated between the liquid surface and the anode, with the bottom PMTs mostly detecting the weaker prompt scintillation light (S1). The time resolved data collected with the SiPM array will be used to perform measurements of spatially-resolved tracks from MeV particle interactions, both in pure and in hydrogen-doped liquid xenon, a candidate mixture to assess whether this is a viable technique for background discrimination in NDBD measurements (see subsection 5.2.2).

Silicon photomultipliers are solid state devices made from an array of single photon avalanche diodes (SPADs) each coupled with a quenching resistor and connected to a common output. Each pair of SPAD and resistor is a microcell that operates in Geiger mode. The SiPM response is characterised by gain, photon detection efficiency (PDE), recovery time and dynamic range. The main sources of noise arise from thermal pulses (dark counts), cross-talk and afterpulses [ESS12]. For the simulations in this work, only the number of pixels and PDE were considered. SiPMs for the VUV region are improving in performance, and in some specific scenarios they may be able to compete with traditional PMTs. The PDE at the xenon scintillation wavelength is now comparable to that of PMTs, and the gain is also similar ($\sim 10^6$) [Per22b]. The dark rate per unit area is still a significant shortcoming ($\sim$ 50 times higher) even at low temperatures (-100 °C), but progress continues to be made on this issue [Per22b]. Correlated noise such as cross-talk and afterpulse are also problematic since they increase with overvoltage[1]. However, there are also potential advantages as SiPMs reach high gain with bias voltages as low as 30 V (for the SiPMs to be used in Xenia is $\sim$ 60 V) when compared to the high voltage required for PMTs ($\sim$ 800 V), very low radioactive backgrounds can be achieved (by moving the readout electronics away from the detector sensitive area), they are compact devices, insensitive to external electric and magnetic fields, and in some cases high granularity of readout is desired and SiPMs lend themselves to that task [Ind21].

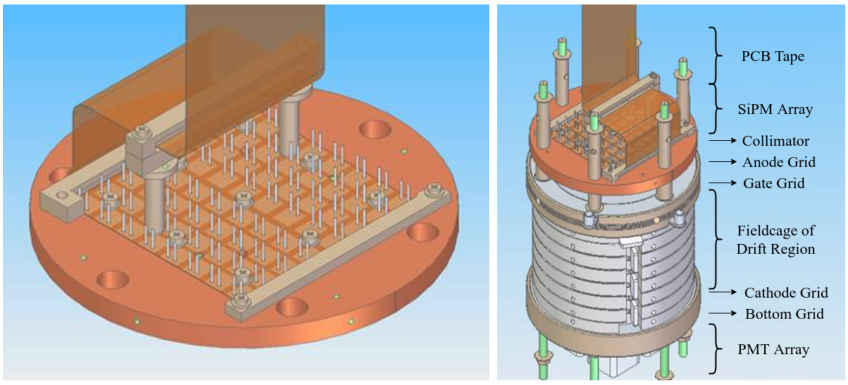

Figure 5.6: SiPM array (left) and array mounted on Xenia (right). The high-density PCB tape depicted in the image will transport the SiPM signals to the electronics responsible for signal processing, outside the main volume. CAD courtesy of E. Holtom, Rutherford Appleton Laboratory.

The development of this small SiPM array helps to prototype crucial technical aspects (Figure 5.6), such as achievable radioactive backgrounds and readout electronics schemes, should a large SiPM array be used to instrument a next-generation experiment. A scaled up version of the photosensor array could be implemented by tiling multiple modules of the present design or, more realistically, larger SiPM modules.

---

[1] The overvoltage controls the operation of an SiPM and is defined as $\Delta V = V_{bias} - V_{breakdown}$. The breakdown voltage is the bias point at which the electric field strength generated in the depletion region is high enough to sustain avalanche multiplication [Ind21].

5.2.2 Xenon doping with light elements

Xenia will run using LXe in the active volume and some studies will feature percent-level doping with hydrogen (H_2 or D_2). Additionally to the standard LXe TPC components and xenon handling system, this involves the design and construction of an H_2 delivery system. A study of the detector response from first principles will be required, taking into account the detailed transport properties of the doped medium, although this is outside the scope of this work.

From theoretical calculations it is expected that hydrogen doping could reduce spatial diffusion approximately by a factor of 2, through a reduction in longitudinal and transverse diffusion coefficients and an increase in electron drift velocity [Tez+04]. It is possible to benefit from the improvement in the longitudinal (z) direction by analysing the shape of the S2 signal in the TPC (work is ongoing covering this subject by exploring deconvolution techniques as shown in Figure 5.7 [Jac22]), and the new array will allow us to exploit a similar improvement in the transverse (x,y) plane. This will be done by exploring machine learning techniques to achieve topology based discrimination of events, which has been done for (z) separation [Sol21] and will be further investigated for (x,y) discrimination as well. These algorithms allow to label each event and separate a single recoiling electron or a double electron event from the NDBD decay by identifying high ionization density regions and the position where the event took place.
The optical optimisation of the chamber combined with these discrimination algorithms under development are expected to give a few hundred micrometre performance in spatial resolution for extended electron tracks of a few millimetres. On the other hand, doping will reduce S2 yields several times [Tez+04], and in Chapter 6 results are presented which approximately quantify how such a reduction impacts the spatial resolution.

Besides these properties, H_2 doping would also be of importance in the dark matter front of a 3^{rd} generation experiment. The doping element would act as the dark matter target and LXe as a sensor: after an interaction of a WIMP particle with hydrogen, the recoiling proton will transfer most of the energy to the medium and produce scintillation and ionisation signals by interacting with xenon electrons [Mon].
Given that this is a single proton and the smallest atomic mass, this is the best target for low mass DM searches (below 10 GeV/c^2) and it further allows the study of spin-independent and spin-dependent DM interactions while LXe continues to provide the essential self-shielding [LAH17] [DAk+21].

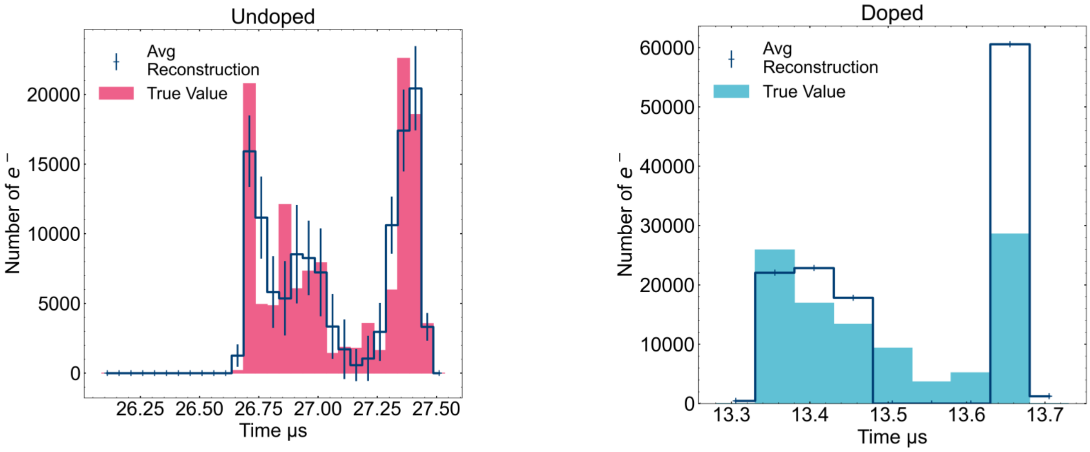

Figure 5.7: Reconstruction of the ionization electron depositions from a $0\nu\beta\beta$ event using a time-domain deconvolution method, for the undoped detector (left) and the doped case (right). Figure from [Jac22].

5.2.3 Collimator

Since the standard LXe TPC design is not an "imaging system", in order to better distinguish the two energy deposition spots corresponding to the electrons from NDBD (as discussed in Chapter 3), the addition of a collimator to the photosensor array is advantageous. Collimators are widely used in gamma cameras and medical imaging devices to produce an image by filtering the radiation in a specific direction before it reaches the sensors [CSP12]. Moreover, in the case of Xenia the collimator will also serve as the mechanical support for the SiPM array.

Xenia will be equipped with a copper collimator (made from a precision-machined single piece of ultrapure copper), blackened by a coating of material with negligible reflectivity in the VUV. It will be placed just under the SiPM array, and have 64 holes aligned with the centre of each sensor. Its purpose is to help improve spatial resolution down to the scale of 100 μm. However, this has a downside of reducing the detection efficiency as it blocks a considerable amount of light coming from the source; even more so because this will be an absorptive collimator rather than a reflective one, which means photons not travelling towards the openings will be absorbed and only direct light will reach the photosensors. This is especially relevant for WIMP signals which are considerably smaller than electronic recoils from NDBD signals; which is why using a collimator in a TPC is unfavourable for WIMP interactions.

The collimator determines the overall performance of the detector, which is why this component needs to be carefully designed. The main aspects to consider are the geometry of the holes (shape, length and diameter), septal thickness, resolution and geometric efficiency. In Xenia the septa are not a concern since all indirect VUV light emitted by the xenon will be absorbed before having a chance to penetrate the walls. Collimator resolution (R_{coll}) can be inferred from the FWHM of a point or linear spread function (PSF or LSP), which can be obtained by building the light profile from a source projected by the collimator onto the detector [CSP12]. For a parallel hole type collimator with round holes, R_{coll} can be estimated from Equation 5.1, where a is the aperture diameter, L is the length of the holes and d is the distance from source to the collimator base. The constant ρ is a correction factor which is a function of the hole shape, angle relative to the sensor axes and of source-detector distance [Wie+04][Wie+05].

$$R_{coll} = \rho \cdot a \cdot \frac{d + L}{L} \tag{5.1}$$

The geometric efficiency is the ratio of light transmitted through the collimator holes over the initial amount of light emitted by the source. For the stated collimator type, it is given by Equation 5.2, where t is the thickness of the material between each aperture [Wie+05].

$$g = \frac{a^2}{4\pi L^2} \frac{a^2}{(a+t)^2} \tag{5.2}$$

The previous equations indicate that resolution improves when the ratio a/L decreases, meaning that long and narrow holes give the best spatial resolution, although it comes at the cost of worse geometric efficiency since $g \propto (R_{coll}^2)$. Another takeaway from Equation (5.1) is that the smaller the distance between source and collimator, the sharper the image will be. Seeing that R_{coll} and g are correlated, increasing this distance results in degraded efficiency according to an inverse square law ($1/d^2$); on the other hand, light is able to pass through a larger number of holes which is proportional to d^2. This can also be observed from the PSF as the maximum height of the function decreases and the width increases in such a way that the total counting rate remains unchanged [CSP12].

The effect of using different types of collimators is further investigated in Chapter 6, where a few variations of parallel-hole, diverging, and converging type collimators were tested.

5.3 Simulation Strategy

The design of the chamber and optimization of its parameters were explored using three main simulation toolkits: ANTS2 [2] [Mor+16], Geant4 [3] [Ago+03] and NEST [4] [Szy+11]. These packages have been developed to meet specific requirements, and the intersection of their strong suits into one integrated tool results in a versatile mechanism for simulating dual-phase drift chambers for particle physics studies.

The work presented in this thesis can be categorised into two parts: the optical optimisation of the chamber and the the simulation of the detector response to interactions, from particle tracking and energy depositions up to the generation of realistic waveforms. The following is a short description of each toolkit and the role attributed to them in the simulations, this is summarised in Figure 5.8. Moreover, a detailed explanation of the development and procedure of each simulation is presented in Chapter 6 and Chapter 7, respectively.

5.3.1 Geant4

Widely used in the scientific community, Geant4 was the first object-oriented simulation toolkit to answer the increasing demand for software which allowed to replicate large and intricate particle detectors (namely the LHC experiments) and the physical processes that occur within. It focuses on the simulation of how particles interact with matter in a variety of applications ranging from high energy physics to nuclear medicine [Ago+03] [All+06].

5.3.2 ANTS2

ANTS2 was created to aid in the development and optimization of Anger camera type detectors. This software was used as the basis for the simulations in the present work, as it was used to build the full detector geometry, define material characteristics, photosensor arrays and electrode grids. The main code to control the flow of simulations was developed using the Python script interface available in ANTS2 and its built-in functions.

Even though Geant4 is a comprehensive tool, for the purpose of fine-tuning detector parameters and optimising performance, the iterative process of adapting the detector to a new configuration and testing it can be somewhat laborious and slow. Additionally, Geant4 is not as versatile for simulating light propagation and it does not feature position reconstruction algorithms from the simulated depositions. These difficulties motivated the use of ANTS2 with Geant4 integration[5]: the geometry and particles are initially defined in ANTS2 which sends this information over to Geant4 to perform particle propagation and the energy depositions are returned to ANTS2 which subsequently executes photon propagation and handles detection in the sensors. ANTS2 allows quick geometry adjustments and delivers results on photossensor hits, photon and particle tracking history retrieved from Geant4 (including timing information), physical processes that occur within detector volumes, and position and energy reconstruction of events [Mor+16].

---

[2] **A**nger-camera type **N**eutron detector: **T**oolkit for **S**imulations

[3] **Ge**ometry **an**d **T**racking

[4] **N**oble **E**lement **S**imulation **T**echnique

[5] Called the G4ANTS module.

5.3.3 NEST

This package was developed for usage alongside Geant4, and as the name implies[3], focuses on simulating energy deposition microphysics in noble elements. NEST can simulate interactions in xenon (and argon) and their detection in a TPC. It offers an exhaustive and accurate description of excitation, ionisation and recombination processes through the use of empirical models for both electron recoils (ER) and nuclear recoils (NR), which were computed based on real world data [Szy+18].

NEST has the ability to simulate NRs from ions, WIMPs, coherent elastic ν-nucleus scattering (solar neutrinos from ^{8}B); as well as ERs induced by γ and β rays, Compton interactions, atmospheric and *pp* solar neutrinos, and other decays like ^{83m}Kr. This tool has been shown to accurately predict light and charge yields as a function of energy, stopping power, drift field, particle and interaction type when compared to existing calibration data sets [Aal+22].

Here, NEST was used to complement the simulation potential of ANTS2 and Geant4 by adapting some crucial parts of the code to be used in the ANTS2 simulation, namely the calculation of scintillation and charge yields, recombination fluctuations, electron diffusion and photon emission timing information.
This implementation was possible thanks to the NESTpy package, which facilitates the implementation of NEST functions in Python based environments.

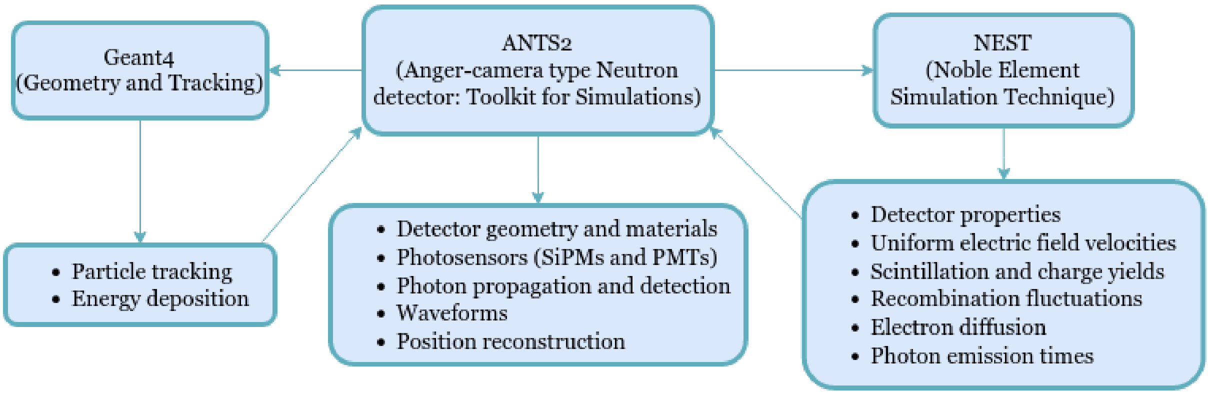

Figure 5.8: Overview of the toolkits used in the simulations and their purpose within the scope of this work.

Chapter 6

Collimator and SiPM Array Studies

6.1 Optical optimisation

The chosen methodology to optimise the position resolution of the chamber consisted in running sets of tests with different parameters which were modified gradually with each new simulation. This allowed to assure that the results were viable before moving on to the next iteration. The first tests were simpler, starting from point-source photon "bombs" located half-way in the electroluminescence gap, along a regular grid in *(x,y)* covering the entire active area. The final set of simulations were more realistic, using photon bombs distributed along a line segment in the z-direction spanning the full height of the Secondary Scintillation region, and sampled in *(x,y)* according to a quasi-random Sobol sequence. The SiPM hits accounted for the geometric fill factor and photon detection efficiency (PDE) of the SiPMs; saturation of each device was analysed and a Poisson correction was applied (see subsection 6.1.1). The anode and gate grids were also added to the detector and were simulated in detail by ANTS2. The details of this process are described thoroughly in the following sub-sections. The geometry being optimised in ANTS2 is shown in Figure 6.1.

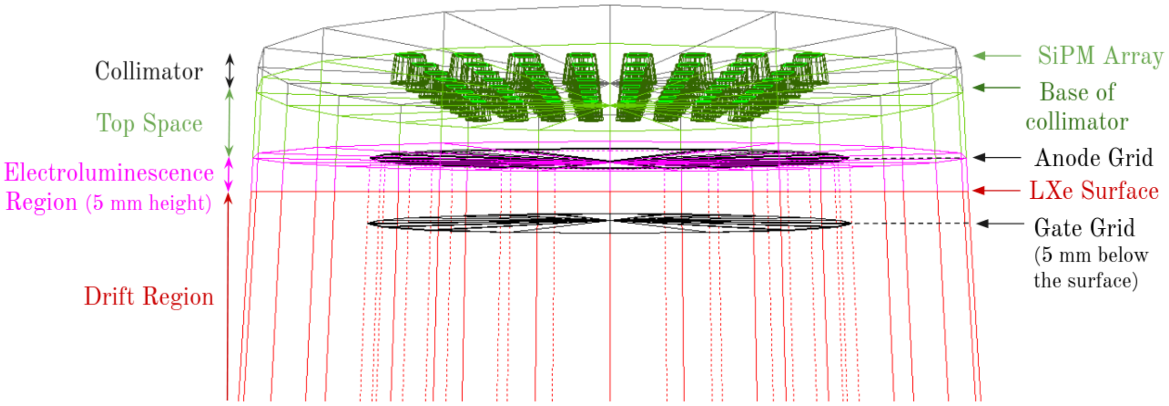

Figure 6.1: ANTS2 simulation geometry of Xenia: top of the chamber.

6.1.1 Simulation procedure

Using the ANTS2 simulation package, over 5000 point sources (i.e. photon bombs) were created to simulate the photon emission in the electroluminescence region, each one defined by their position, emission time and number of photons. These photon bombs were generated with random *(x,y)* coordinates along a 5 mm vertical line, representing the electroluminescence emission which is approximately uniform as electrons emitted from the liquid surface travel in the high electric field up to the anode. The total electroluminescence light expected from a NDBD decay event is approximately 60 million photons in nominal conditions when using undoped LXe. Using the NEST calculator[1], for a β of 1.25 MeV, the number of ionisation electrons produced is ∼60 000, so the two βs in a NDBD would produce a total of 120 000 electrons of which 110 000 would be extracted to the gas phase, considering an extraction efficiency of 92%. The average electroluminescence yield calculated by NEST for the Xenia detector is $\sim$ 500 photons per electron in the gas, which amounts to a total of 60 million S2 photons. For each source in the simulation, 6 million[2] S2 photons were emitted which would correspond to the amount of photons that make up a slice of the NDBD track, if we were to divide the track into 10 parts for analysis. The retrieved data for analysis is the number of firing pixels in each SiPM channel, which is recorded after ANTS2 finishes light propagation from each photon bomb.

SiPM saturation, corresponding to the occurrence of multiple photons hitting the same microcell, is a key consideration which was addressed for the two device models. The dead area between pixels, defined by a geometric fill factor, was also implemented in the simulation. However, the characteristic pixel recovery time and crosstalk were not included and the silicon was considered to have no reflection.
Saturation curves for the SiPM models were generated through a simple simulation in which an increasing amount of photons is released with each new iteration. The simulation registers the number of pixels hit and the number of photons that were able to reach the sensor in each iteration. Fitting the saturated data with Equation (6.1)[3] which takes into account the Poisson nature of the process, allowed to obtain the free fit parameter N_{total} and use the function to convert the number of activated pixels to the number of pixels expected to have fired [Gru+14]. Later this function was used to correct the light collection data from the main photon bombs simulations.

In Figure 6.2, N_{photon} corresponds to an ideal scenario where the number of photons reaching the sensor equals the number of detected photons and N_{fired} represents a realistic situation in which the SiPM saturates due to the finite number of pixels [4]. N_{seed} is the correction we want to achieve, where we calculate the number of fired pixels if the SiPM did not saturate, only considering the PDE limitation of the device. A concrete example of this is shown further down in Figure 6.8.

$$N_{fired} = N_{total} \times \left[1 - e^{-\frac{N_{photons\ \ reach} \times PDE}{N_{total}}}\right] \tag{6.1}$$

---

[1] Calculator available at https://nest.physics.ucdavis.edu/download/calculator.

[2] Due to the high use of computational resources for this simulation, the number of simulated S2 photons was reduced to 6 million without loss of generality in the final results.

[3] This equation is valid for an ideal SiPM and an infinitely short light pulse.

[4] In reality, the SiPM response curve deviates from linearity not only because of the number of pixels as well as their characteristic recovery time, after-pulsing, cross-talk, and dark-noise. However, these other parameters were not taken into account here.

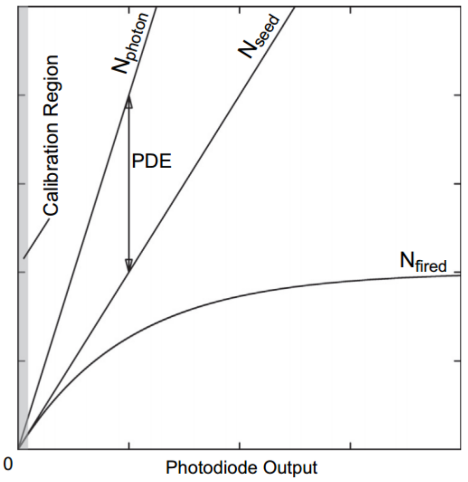

Figure 6.2: Schematic of a typical calibration plot for an SiPM [Gru+14].

Corrected data from the photon bombs is then loaded back into ANTS2, and using the Reconstruction module, LRFs are fitted [Mor+16]. The LRFs parameterise the light collection response from each SiPM as a function of distance to the sensor axis [Sol+12], as exemplified in Figure 6.3. A spline fit is made to the data points from each channel, according to a few user-defined parameters, such as LRF type (which can be axial, polar, or vary in x and y). In these studies, all LRFs were set to have axial symmetry, null derivative at the centre of the SiPM, and have a negative derivative with increasing radial distance.

The leading algorithm for vertex reconstruction in two-phase xenon detectors is called Mercury, a code developed by the Dark Matter group from LIP-Coimbra for ZEPLIN-III, then used in LUX and now in LZ [Sol+12]. This is a data-driven technique which is fast and very accurate; it is based on the measurement of LRFs for each channel using calibration data for instance. These LRFs are determined iteratively by adjusting the general spline parameters until the fit converges for every sensor, and then used "offline" in a least-squares or a maximum likelihood fit for the reconstruction of the *(x,y)* position of the S2 light pattern in each event. ANTS2 implements these algorithms on top of a fast optical code optimised for these and similar detector arrays.

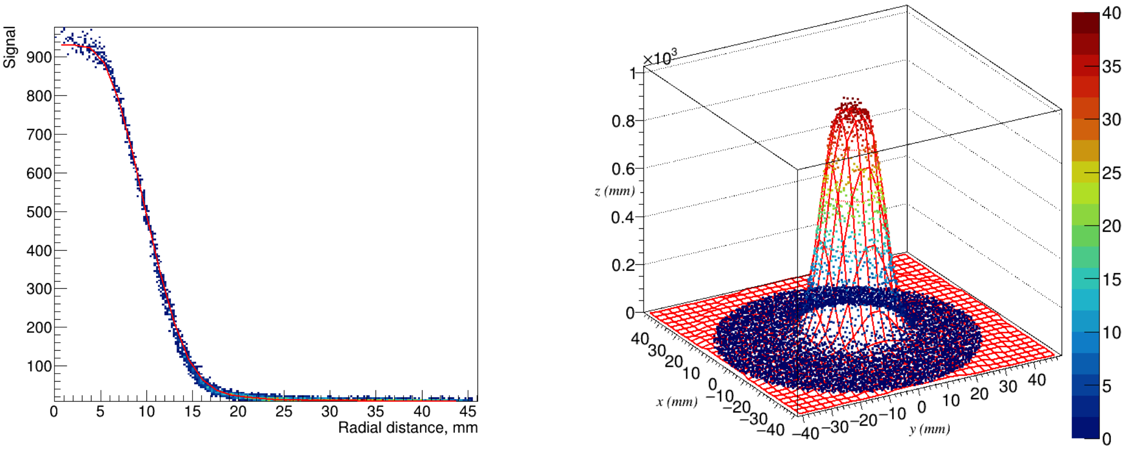

Figure 6.3: Example of a light response function with axial symmetry for an SiPM in a central location of the chamber (left) - refer to Figure 5.4 to see the position of device number 28 - and the equivalent plot in 3D (right). The red curve represents the fit and simulated data points follow the coloured scale.

In these studies, the Mercury algorithm was used for event reconstruction with a maximum likelihood fit, and three cuts were applied to the data before reconstruction, namely defining which sensors are passive, meaning the data for these channels is not considered when reconstructing events. The lower PMTs were defined as static passive sensors as they do not contribute appreciably towards the S2 signal; data from dynamic passive SiPMs was discarded as these recorded hits above a saturation threshold (chosen during saturation tests); as well as the SiPMs with hits below a certain noise cut, where the light is so faint it does not improve reconstruction.

6.1.2 Parameters under study

The main chamber characteristics iterated in the simulation study were:

a) The device model (S13370-3050 or S13370-3075);

b) The distance between the liquid surface and the collimator plate;

c) The thickness of the collimator plate;

d) The shape of the collimator apertures;

e) Reflectivity of TPC fieldcage;

f) Anode and gate mesh parameters;

g) Position resolution as function of S2 photons;

h) Effect of SiPM misalignment relative to the centre of the collimator hole (x,y tolerance);

i) Effect of vertical separation between collimator and SiPM (z tolerance).

The SiPM devices which were tested in this work are Hamamatsu S13370-3050CN and S13370-3075CN [Pho17]. Both devices have the same size 5.9×6.6 mm, with 3×3 mm active area and are arranged in a square array of 64 photosensors. The -3050CN model features 3600 pixels with a pixel pitch of 0.05 mm filling 60% of the entire array area. The -3075CN model has 1600 pixels and a fill factor of 70% giving a pixel pitch of 0.075 mm. Detection takes into account the average PDE of these devices at 175 nm, which were measured to be to 28.0% for -3050CN and 34.5% for -3075CN, respectively.

The distance between each SiPM device in the array (pitch) was set the smallest possible at 8 mm; this was not part of the optical optimisation. Keeping the array “real-estate” within a 64-mm side footprint allows the stacking of this design with no dead spaces. It was assumed that the array itself as well as the lateral walls immediately around it would be black, since lateral reflections will harm the position resolution. In the detector, this will be acomplished by using a Kapton skirt around the array and the copper piece itself will be blackened.

The distance between the collimator plate and the LXe surface was varied and tested to find which offers better results. The collimator plate is located in the gas with the SiPM array devices at the back. The apertures of the collimator plate were varied in shape (conical and cylindrical) and size, and are specified in Tables 6.2 and 6.3. Only the collimators with the best preliminary results were chosen to be simulated several times at different distances from the LXe surface.

The reflectivity of the Xenia fieldcage was a design parameter: this could remain as bare PTFE (very high reflectance in the VUV) or it could be lined with Kapton (nearly black in the VUV).

The former is strongly preferred for various reasons, but confirmation was needed that this would not come at the expense of optimal position resolution.

Another set of critical parameters was related to the electrode grids used in Xenia, in particular the anode (5 mm above the liquid surface) and the gate grid (5 mm below the surface). These grids were included only in the later stages of the studies. The gate has the effect of focusing the ionisation clouds being drifted from the active volume, and here it was considered that the pitch of this grid is small enough as to not degrade the spatial resolution significantly; a grid with ∼ 0.100 mm pitch or less will be selected for the real chamber, although the one considered here is somewhat coarser (this has little optical impact for this particular study). The anode has a sizeable effect, since this grid will cast a shadow onto the SiPM array when S2 photons emitted from below, and this does have a major effect on the achievable resolution as shown in the next section. In this case the two finest meshes in the market were identified and studied. Table 6.1 specifies the characteristics of the two different anode grids (a coarser and a finer one) and one gate grid that were tested in the last stages of this study.

Table 6.1: Geometric characteristics of the electrode grids tested in the simulations.

	Anode №1	Anode №2	Gate №1
Shape	Crossed wires	Crossed wires	Crossed wires
Aperture (mm)	0.83	0.111	0.077
Wire diameter (mm)	0.15	0.03	0.050
Pitch (mm)	0.98	0.14	0.127
LPI (lines per inch)	25.9	180.1	200
Open area (%)	72	62	37

For obtaining the resolution of each set of runs, it is recommended to use two different sets of data, one for training (usually a well defined grid of photon bombs) and other for testing (with more realistic and random photon bombs), meaning each detector setup would need to be simulated twice as this reduces the bias in the results. However, to reduce simulation time in this work, the same dataset was used for training LRFs and for resolution measurement.
Excluding the first set of runs, in all cases hereafter, the distributions of reconstructed positions taken from Mercury in x and y, are approximately Gaussian and have negligible bias; examples are given in Figures 6.6 and 6.14. In the following sections, the standard deviation of the fitted Gaussian is quoted as the linear resolution (σ_x and σ_y), which typically has error in the final significant digit. This metric is somewhat more optimistic than the RMS values for the actual raw distributions obtained in each case, but this difference is actually small for the more central regions in the LXe TPC, less affected by wall effects. The radial resolution in the following tables is calculated as $R_{radial} = \sqrt{\sigma_x^2 + \sigma_y^2}$. The standard deviation of the fitted Gaussians is the key metric here since it will be possible to select these events in the actual detector.

The vertical spacing and the misalignment of an SiPM centre relative to that of the collimator hole was also a necessary study to take into account real conditions when assembling the detector, as these can heavily influence LCE, energy and spatial resolution. The *(x,y)* positional tolerance comes from the location of the silicon chip within its ceramic carrier, and the fact that the an SiPM chip can be manually replaced if needed, thus possibly introducing a systematic error larger than the original uncertainty quoted by the chip manufacturer.

6.2 Results and discussion

6.2.1 First set of runs

Initially, five 4 mm thick collimators were tested, as described in Table 6.2, informed by previous work done by an internship student [Jak20]. These first tests using point photon bombs were the least realistic, using a detector geometry very similar to Xenia[5], hence some parameters were replaced for the correct values for the following runs. This first set was carried out with the collimator placed at a distance of 30 mm away from the LXe surface, without any grids, with a simple SiPM model of 2500 pixels and 100% PDE. This was a preliminary study that only contemplated qualitative results in order to get a picture of which designs were the most promising moving forward. Collimators number *1a* and *4a* were excluded for being the least favourable in terms of saturation threshold, LCE, light radius and the number of useful SiPMs (with non-null signal and unsaturated); an example for LCE is shown in Figure 6.4. The remaining designs moved on to the next set of simulations to test one collimator of each shape in the accurate model of Xenia.

Table 6.2: Characteristics of the collimators studied in the preliminary simulations.

Collimator designation	*1a*	*2a*	*3a*	*4a*	*5a*
Shape	cone section	cone section	cylinder	inverted cone section	inverted cone section
Thickness (mm)	4	4	4	4	4
Exit aperture (mm)	2.54	3	3	4.3	4.3
Entry aperture (mm)	4.66	4	3	2.3	3.3

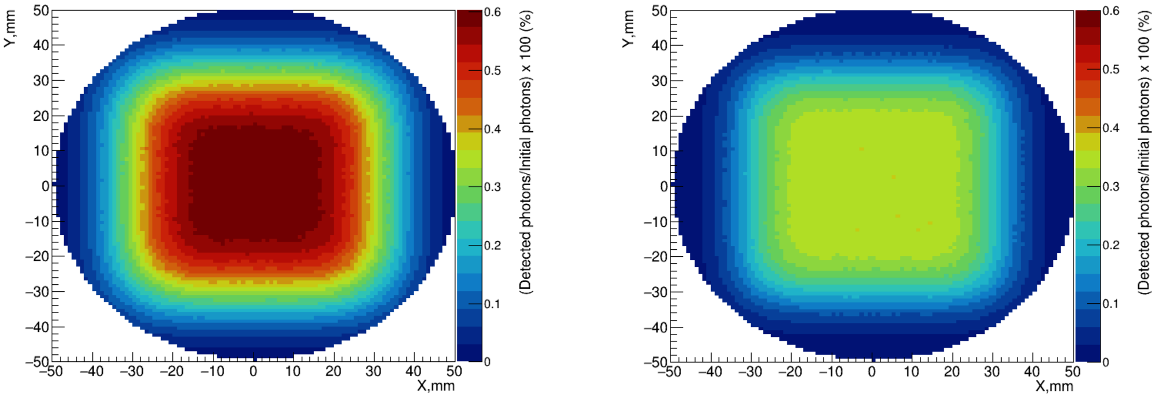

Figure 6.4: Light collection efficiency for collimator *2a* (left) and collimator *3a* (right). In the central region design *2a* has a LCE of 0.6% and design *3a* has a maximum LCE of 0.3%.

---

[5] At the time of performing the first test runs there was lack of information on the specific geometry and dimensions of Xenia.

6.2.2 Second set of runs

From this point onwards, the chamber dimensions were corrected to match Xenia and the two Hamamatsu SiPM models referred above were introduced in the simulation. The different collimators studied with the Xenia geometry are described in Table 6.3.

Taking as reference the most promising designs from the previous runs, this set aimed to test the effect of decreasing the collimator thickness (designs *2b*, *3b* and *5b*), as it could improve light collection and possibly resolution too. Three additional designs were introduced (*7b*, *8a* and *8b*), in which the collimator apertures are wider to make use of all the pixels in the photosensors. The photon sources in this run were single points spaced by 1 mm in the *(x,y)* plane. During these runs the two Hamamatsu SiPM models were tested and it was found that the S13370-3075CN model consistently offered better results for all configurations. This can be explained by the higher PDE in this model, coming from the larger fraction of active SiPM area, despite the smaller number of pixels.

Table 6.3: Characteristics of the collimators studied in the Xenia simulations.

Collimator	*2a*	*2b*	*3b*	*5b*	*7b*	*8a*	*8b*	*9a*	*10a*
Shape	cone section	cone section	cylinder	inv. cone section	cone section	inv. cone section	inv. cone section	cone section	cylinder
Thickness (mm)	4	2	2	2	2	4	2	4	4
Exit aperture (mm)	3	3	3	4.3	4	6	6	4.2	4.2
Entry aperture (mm)	4	4	3	3.3	6	4	4	5.2	4.2

The conclusion after this set of simulations pointed to the best design being collimator *2a* with SiPM model S13370-3075CN at shorter distance (21 mm) to the LXe surface, as summarised in Table 6.4. Both the total and central resolution are shown, the latter being relative to the inner part of the chamber for a radial distance smaller than 20 mm, which omits the points in the outer 20 mm of the detector where resolution deteriorates significantly (see subsection 6.2.6). Although design *3b* with the same SiPM model had a similar resolution, the choice of the mentioned *2a* design was also supported by a test to infer the LCE, which was higher for a conical shaped collimator compared to a cylindrical one, as shown in Figure 6.4.

The following figures are relative to the analysis of design *2a*. For the sake of illustration, Figure 6.5 shows the data for two different LRFs, represented as the number of detected photons as a function of the distance from the light source to the centre of an SiPM. The spatial resolution for each axis represented in Figure 6.6 was obtained by plotting a histogram of the reconstructed coordinate subtracted by the true simulated position and taking the sigma of the Gaussian fit. The individual x and y resolutions are around 80 μm, giving a combined radial resolution of 122 μm for this design, fairly close to the desired value of 100 μm as mentioned in the previous chapter.

Table 6.4: Summary of radial resolution for the second set of ANTS2 simulations (SiPM data is not area resolved, saturation correction and grids were not considered here).

Col.	Field cage reflectivity	Dist. to LXe (mm)	SiPM model (pixels)	Light source	XY sampling	Z sampling	Total Radial Resolution (mm)	Central Radial Resolution for r<20 mm (mm)
2b	Kapton	21	1600	point	1 mm grid	point	0.129 ± 0.001	0.102 ± 0.002
2b	Kapton	21	3600	point	1 mm grid	point	0.134 ± 0.001	0.108 ± 0.002
3b	Kapton	21	1600	point	1 mm grid	point	0.124 ± 0.001	0.098 ± 0.002
3b	Kapton	21	3600	point	1 mm grid	point	0.135 ± 0.001	0.107 ± 0.002
5b	Kapton	21	1600	point	1 mm grid	point	0.134 ± 0.001	0.149 ± 0.002
5b	Kapton	21	3600	point	1 mm grid	point	0.133 ± 0.001	0.106 ± 0.002
7b	Kapton	21	1600	point	1 mm grid	point	0.138 ± 0.001	0.112 ± 0.002
7b	Kapton	21	3600	point	1 mm grid	point	0.141 ± 0.001	0.120 ± 0.002
8b	Kapton	21	1600	point	1 mm grid	point	0.132 ± 0.001	0.105 ± 0.002
8b	Kapton	21	3600	point	1 mm grid	point	0.133 ± 0.001	0.106 ± 0.002
2a	Kapton	21	1600	point	1 mm grid	point	0.122 ± 0.001	0.089 ± 0.001
8a	Kapton	21	1600	point	1 mm grid	point	0.153 ± 0.001	0.131 ± 0.002
2a	Kapton	30	1600	point	1 mm grid	point	0.149 ± 0.001	0.118 ± 0.002
8b	Kapton	30	1600	point	1 mm grid	point	0.187 ± 0.001	0.159 ± 0.003

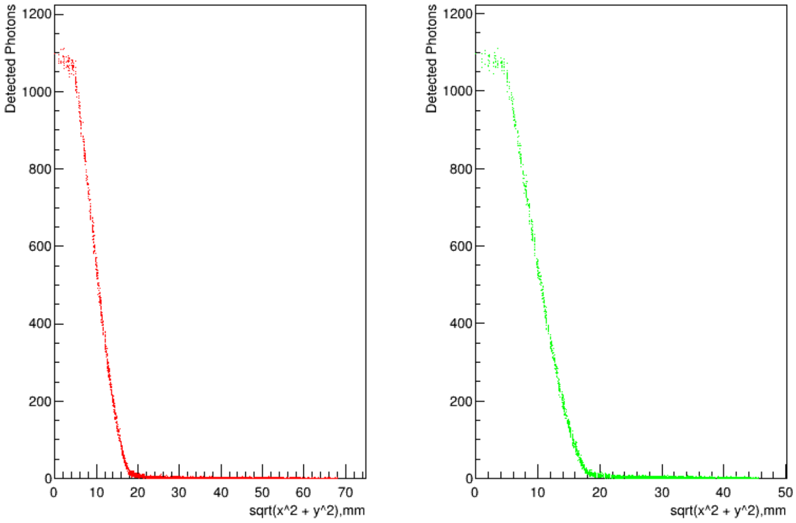

Figure 6.5: Data of SiPM hits from all events for SiPM9 located in the edge of the chamber (left), and SiPM28 near the centre (right). The distance in the x-axis is measured from the emission point to the centre of each SiPM. These plots are relative to the highlighted configuration in Table 6.4. The fits made to these data points for each channel will be the set of LRFs for each specific detector configuration.

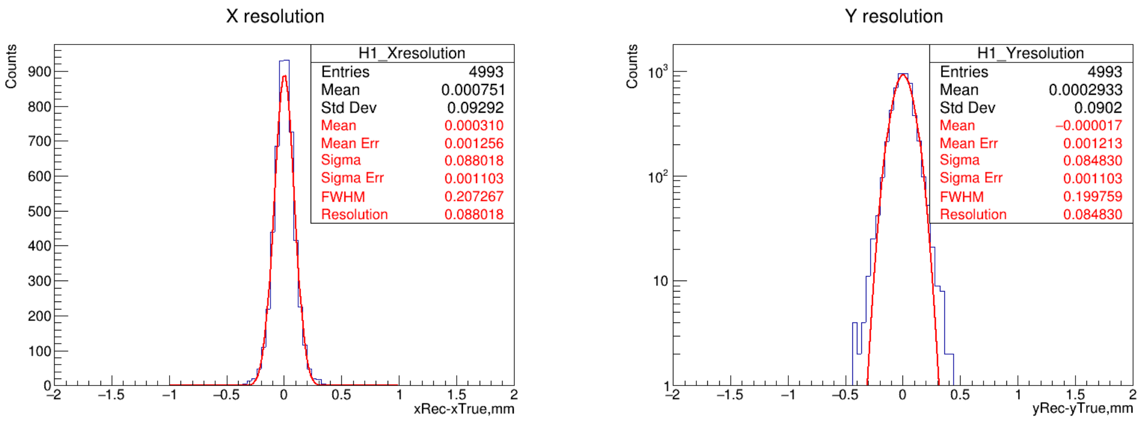

Figure 6.6: Resolution in the total active region of the chamber (r<40 mm) in the x-direction (left) and y-direction with log scale (right) for the highlighted configuration from Table 6.4.

6.2.3 Third set of runs

The evidence suggested that the studies should follow collimator *2a* (conical), so we proceed by examining the resolution at several distances from the LXe surface (at 15, 21, 30 and 40 mm), and to check the effect of the fieldcage reflectivity. This was the first set of runs where the light correction due to saturation was applied.
The test results are compiled in Table 6.5 and Figure 6.7. These revealed that resolution is better overall when Kapton is used in the fieldcage walls, and that it improves for distances closer to the LXe surface. However, at the smallest separation considered (15 mm), the use of Kapton or PTFE ceased to have an influence, as the resolution was the similar in both cases. The higher fieldcage reflectivity brings more advantages as it makes the detector more sensitive to other physics studies of interest at lower energies, for this reason the decision was made to continue with the PTFE walls.

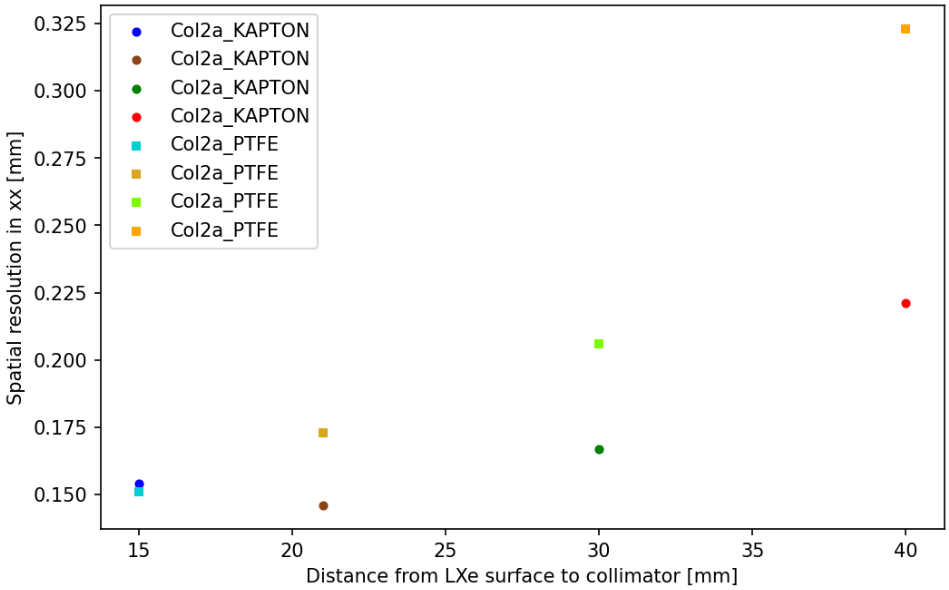

Figure 6.7: Linear resolution along x direction as a function of the distance between the LXe surface and the collimator plate.

Table 6.5: Summary of the radial resolution for the third set of ANTS2 simulations (SiPM data is not area resolved but light saturation correction was applied, grids are not included).

Col.	Field cage reflectivity	Dist. to LXe (mm)	SiPM model (pixels)	Light source	XY sampling	Z sampling	Total Radial Resolution (mm)	Central Radial Resolution for r<20 mm (mm)
2a	PTFE	15	1600	point	1 mm grid	point	0.151 ± 0.001	0.119 ± 0.012
2a	PTFE	21	1600	point	1 mm grid	point	0.173 ± 0.002	0.119 ± 0.002
2a	PTFE	30	1600	point	1 mm grid	point	0.206 ± 0.002	0.147 ± 0.002
2a	PTFE	40	1600	point	1 mm grid	point	0.323 ± 0.003	0.232 ± 0.004
2a	Kapton	15	1600	point	1 mm grid	point	0.154 ± 0.001	0.121 ± 0.002
2a	Kapton	21	1600	point	1 mm grid	point	0.146 ± 0.001	0.111 ± 0.002
2a	Kapton	30	1600	point	1 mm grid	point	0.167 ± 0.001	0.127 ± 0.002
2a	Kapton	40	1600	point	1 mm grid	point	0.221 ± 0.013	0.176 ± 0.003

6.2.4 Fourth set of runs

Considering that design *2a* has an aperture that partially covers the photosensor, cutting down the area of useful pixels, a final collimator similar to design *2a* was tested, with the same thickness but wider diameters, keeping the ratio between the two openings. Collimator *9a* was therefore simulated with the two previous best configurations (21 mm separation with Kapton and 15 mm with PTFE walls) to assess if this could be the final design in lieu of collimator *2a*. An additional collimator *10a* (see Table 6.3), was simulated as well in order to confirm that a wider cylindrical aperture was not a viable option.

At this stage, after some troubleshooting, a fault was found in the simulation, which prevented to make the SiPM response area resolved, i.e. the geometric fill factor was not properly being taken into account, so this was corrected from here onwards. The results in Table 6.6 confirmed that the resolutions for collimators *2a* and *9a* under the same conditions were similar and that the use of Kapton enhanced resolution, as was previously found.

Table 6.6: Summary of radial resolution for the fourth set of ANTS2 simulations (SiPM data is area resolved with light saturation correction and without grids).

Col.	Field cage reflectivity	Dist. to LXe (mm)	SiPM model (pixels)	Light source	XY sampling	Z sampling	Total Radial Resolution (mm)	Central Radial Resolution for r<20 mm (mm)
2a	PTFE	15	1600	point	1 mm grid	point	0.155 ± 0.001	0.119 ± 0.002
9a	PTFE	15	1600	point	1 mm grid	point	0.157 ± 0.002	0.113 ± 0.002
9a	Kapton	21	1600	point	1 mm grid	point	0.151 ± 0.001	0.102 ± 0.002
10a	PTFE	15	1600	point	1 mm grid	point	0.194 ± 0.002	0.172 ± 0.003

It was decided to select collimator *9a* as this takes advantage of the full SiPM active area while maximising light collection, and a PTFE fieldcage. This parallel cone collimator is often called single-sided knife-edge pinhole in the literature. Although further research is necessary on this type of collimators in order to clarify discrepancies between theoretical predictions and simulated data [MH17], we were able to confirm the overall behaviour of each collimator type during these optical optimisation studies.

Comparing the results obtained so far and looking back at the theoretical considerations on collimators from section 5.2.3, we verified that for conic/diverging collimators with the same aperture, longer and narrower holes give better results: for instance collimator *2a* is longer and better than *2b* in Table 6.4, and design *2a* contrasted by *9a* in Table 6.6 shows that the wider

aperture of design *9a* diminishes the resolution slightly (possibly offset by the larger amount of pixels receiving light).
However, in the case of inverted cones/converging collimators with the same opening, a shorter length is more advantageous (e.g. *8a* versus *8b* in Table 6.4). It was also seen that for the same collimator length, narrower apertures improve resolution although at the cost of geometric efficiency, this is observed for instance in collimators *2b* and *3b*: even though design *3* grants better resolution, design *2* has higher LCE (see Table 6.4).

Additionally, in Chapter 5 it was shown that smaller distances between source and collimator result in sharper images, this was clear in the third set of runs (see Table 6.5), for the four distances that were tested in both Kapton and PTFE.

6.2.5 Fifth set of runs

The next step was to assess the effect of introducing the electrode grids. The selection of gate and anode grid meshes is critical to obtain the best resolution. In both cases the tests were made with ultra-fine woven meshes which can be sourced commercially. The gate, which sits a few mm below the liquid surface, "focuses" the electron clouds as they drift to the liquid surface, and hence its pitch must be much smaller than the required spatial resolution. The anode, which sits in the gas phase a few mm above the liquid surface, creates the strong electric field needed to emit the drifting electrons and then to generate the large S2 response. Several effects can be introduced by the anode in particular; these include the shaping of the field lines followed by electrons as they approach the anode as well optical effects, for instance the casting of a shadow onto the array which spoils the resolution significantly.

Even though it had been established that 15 mm was the ideal distance to the liquid surface, the configurations with 15 mm and 21 mm were tested once more as it was unclear if the presence of the grids could influence the chosen distance. Furthermore, the best configuration was also tested with the 3600 pixel SiPM so as to verify that introducing the grids would not change the preferred sensor model.

Finally, the point source photon bombs were altered to vertical sources composed of 20 evenly spaced points in the 5 mm between the liquid surface and the anode. The sampling of the *(x,y)* coordinate was randomised to approximate a more realistic scenario and minimise systematic effects. The results for this set of runs are described in Table 6.7 and it was found that very fine meshes were needed for both gate and anode to optimise the spatial resolution, having chosen to combine Anode №2 with Gate №1 (see Table 6.1).

Table 6.7: Summary of radial resolution for the fifth set of ANTS2 simulations (SiPM data is area resolved with light saturation correction).

Col.	Field cage reflectivity	Dist. to LXe (mm)	SiPM model (pixels)	Grids	Light source	XY sampling	Z sampling	Total Radial Resolution (mm)	Central Radial Resolution for r<20 mm (mm)
9a	PTFE	15	1600	none	point	1 mm grid	point	0.157 ± 0.002	0.113 ± 0.002
9a	PTFE	15	1600	none	linear	1 mm grid	20 even points	0.141 ± 0.005	0.105 ± 0.002
9a	PTFE	15	1600	anode1	linear	1 mm grid	20 even points	0.197 ± 0.002	0.125 ± 0.002
9a	PTFE	15	1600	anode1+gate1	linear	1 mm grid	20 even points	0.178 ± 0.002	0.119 ± 0.002
9a	PTFE	15	1600	anode1+gate1	linear	random unif.	20 even points	0.219 ± 0.002	0.182 ± 0.003
9a	PTFE	21	1600	anode1+gate1	linear	random unif.	20 even points	0.228 ± 0.003	0.189 ± 0.003
9a	PTFE	15	1600	anode2+gate1	linear	random unif.	20 even points	0.155 ± 0.002	0.118 ± 0.002
9a	PTFE	21	1600	anode2+gate1	linear	random unif.	20 even points	0.229 ± 0.002	0.183 ± 0.002
9a	PTFE	15	3600	anode2+gate1	linear	random unif.	20 even points	0.175 ± 0.002	0.147 ± 0.002

In addition, the stainless steel used in the meshes has some VUV reflectivity and this causes additional effects which can be detrimental for reconstruction but it also has the benefit of increasing LCE as the presence of the gate traps more light between the electrodes, which gets reflected repeatedly until it reaches the sensor or is absorbed (compare resolutions in lines 3 and 4 of Table 6.7).

6.2.6 Final set of runs: best design

In conclusion, the best design was for a 4 mm thick collimator plate with 5.2-to-4.2 mm conical apertures, located 15 mm above from the liquid surface (i.e. 10 mm above the anode plane), combined with the 1600-pixel SiPM model. The *(x,y)* sampling was switched from a random sequence to a quasi-random Sobol sequence [JK03] (i.e. low discrepancy between the points of a set), which ensures a more uniform dispersion of points.

The results with this configuration are summarised in Table 6.8, and the corresponding saturation plots, LRFs and resolution histograms are presented in the subsequent figures from Figure 6.8 to 6.16.
Figure 6.8 is relative to the SiPM saturation analysis. The dashed blue line is set at the total number of pixels in the SiPM without accounting for the geometric fill factor. The data points come from the aforementioned ANTS2 simulation: the orange points are the number of photons reaching the surface of the SiPM and the green data points are the number of fired pixels, meaning the orange points were corrected by applying the PDE factor. The solid red line is the Poisson fit (from Equation (6.1) and as shown in Figure 6.2) to the simulation points and the inset has the optimal fit value for N_{total}. The Poisson correction was applied to the uncorrected data points and the verification is shown in the plot on the right hand side, which is consistent with the expected slope of fired pixels.

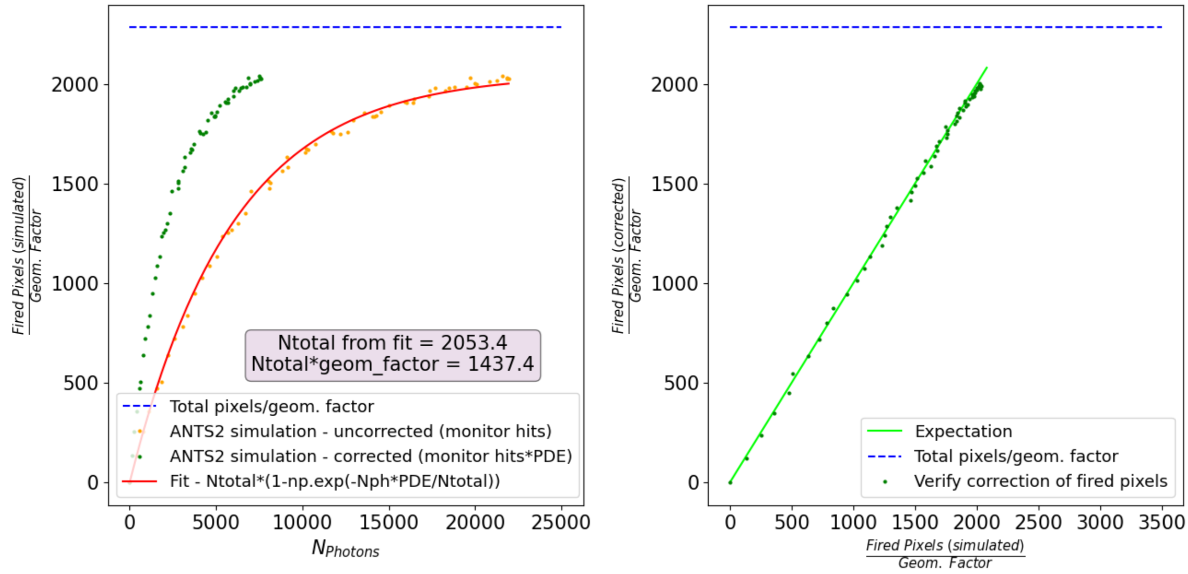

Figure 6.8: Simulated saturation curves and Poisson fit (left) and corrected number of expected firing pixels against the simulated firing pixels (right) for a central SiPM sensor. The axis scale is corrected with the fill factor since the simulation was run with this value into account and Equation (6.1) does not include this.

Figure 6.9 shows the number of detected photons (hits) in the entire run, with the data from all 64 SiPMs overlapped in different colours in order to have a full picture of where the light cuts should be made. By looking at the two plots one can note where the cuts were defined for saturation and noise light: in this particular case to mitigate errors from non-linearity, the

SiPMs that registered more than 850 hits could not be used for reconstruction, which corresponds to a threshold of ~60% of N_{total} and the noise cut was defined at 30 hits. It was verified using ANTS2 that cutting above this would start increasing the deviation instead of improving resolution.

The dispersion and intensity of light from a vertical photon source of 6 million photons is shown in Figure 6.10, located under SiPM number 28. To visualise the negative effect the PTFE walls have on reconstruction bias, Figure 6.11 was made by plotting on a 2D histogram how much the reconstructed position deviates from the true position.

Since the amount of light collected heavily influences spatial and energy resolution, two tests were run to obtain the LCE for the best design with and without electrode grids for comparison. Figure 6.12 shows that without grids this setup allows ~0.45% of the total light to be collected and including the gate and anode of choice (as discussed in sub-section 6.2.5), the collection efficiency is at most ~0.25% in the central region. As expected, these results indicate that the light collection worsens with the presence of grids, however these are a key component of the TPC detector,so they need to be carefully chosen in order to assure the LCE is still high enough for the physics studies of interest.

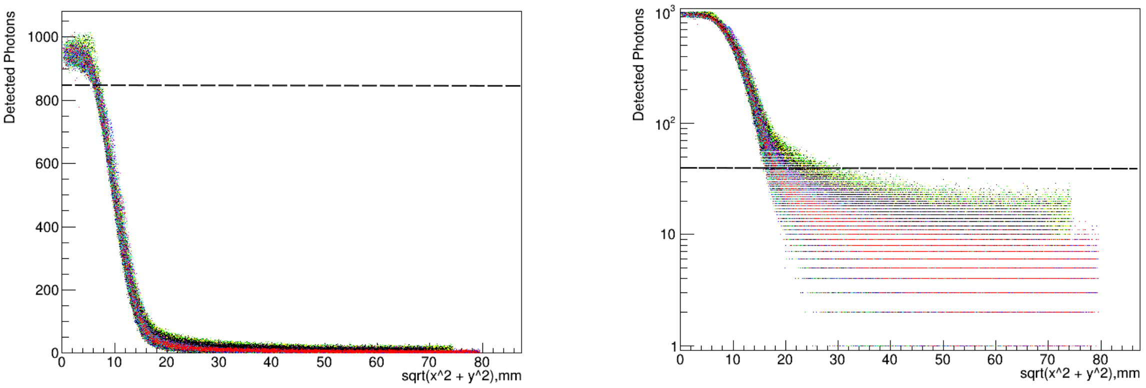

Figure 6.9: Overlapped data of corrected SiPM hits from all events (left), the saturation cutoff at 60% sets the threshold number of detected photons above which the data ceases to be used for reconstruction. Same plot with log-y scale, allowing to estimate noise from faint light (right). The dashed lines indicate the signal cuts.

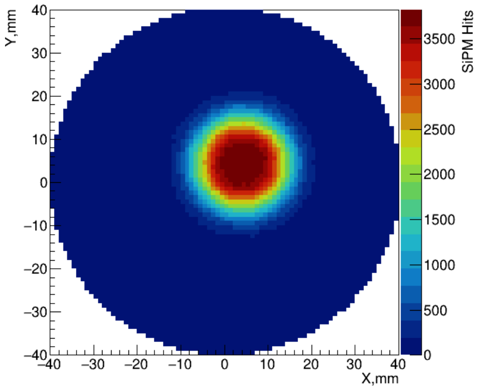

Figure 6.10: 2-D histogram showing the transversal dispersion and intensity of detected light over the chamber for a photon source located under SiPM28.

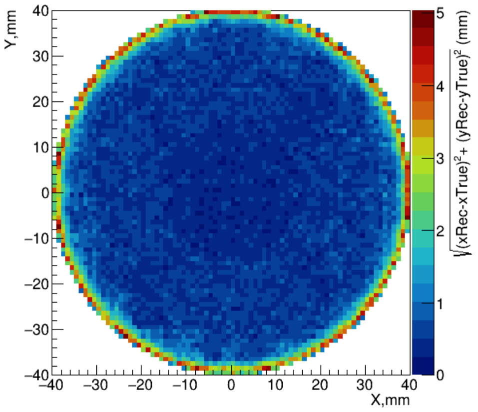

Figure 6.11: 2D-histogram representing the difference between true and reconstructed positions of events throughout the radial active area.

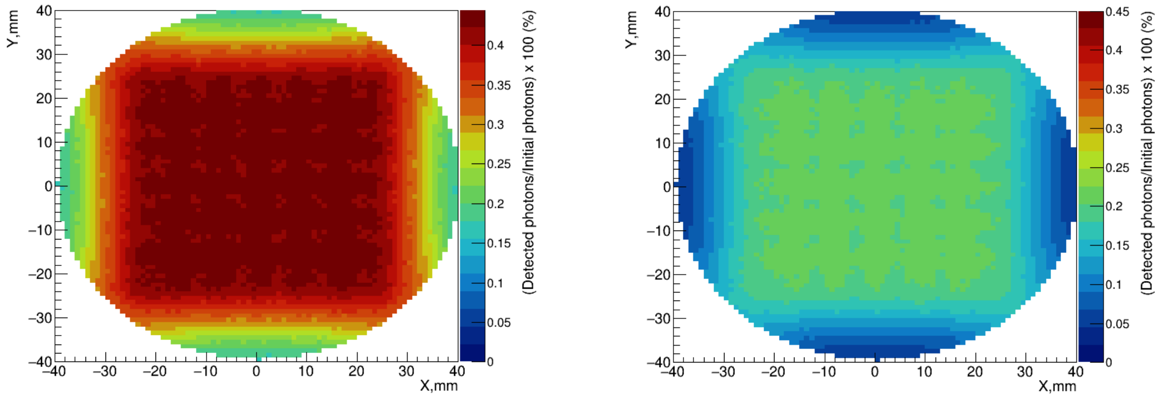

Figure 6.12: Light collection efficiency of best design with no grids (left) and with anode and gate grids (right).

The resolution in the full chamber is represented in Figure 6.13, where there are residual tails that do not follow the Gaussian fit. These are a consequence of the presence of PTFE walls which disperse the light several times before it gets detected, meaning the events occurring in the outer regions of the chamber will not be reconstructed within a small margin of error[6]. Therefore, the region that ought to be considered when selecting events of interest (fiducial volume) should not include the periphery of the chamber.

Figure 6.16 represents the resolution in radial slices of the detector, which is seen to decline for r>20 mm outwards; this is also visible in Figure 6.15, where there is a somewhat wider dispersion of points from linearity, this suggests the 20 mm mark is the clear choice for the fiducial radius. The resolution histograms from Figure 6.14 were made using only events in the inner 20 mm radius of the detector and these values are also included in Table 6.8. The spatial resolution found for these conditions is 124 μm radially, and for each direction x and y the Gaussian sigma reaches 87 μm and 89 μm respectively. During testing resolutions improved when the number of simulated events was increased, and considering these results were obtained with ∼6000 events only, they could possibly improve with a more extensive simulation run.

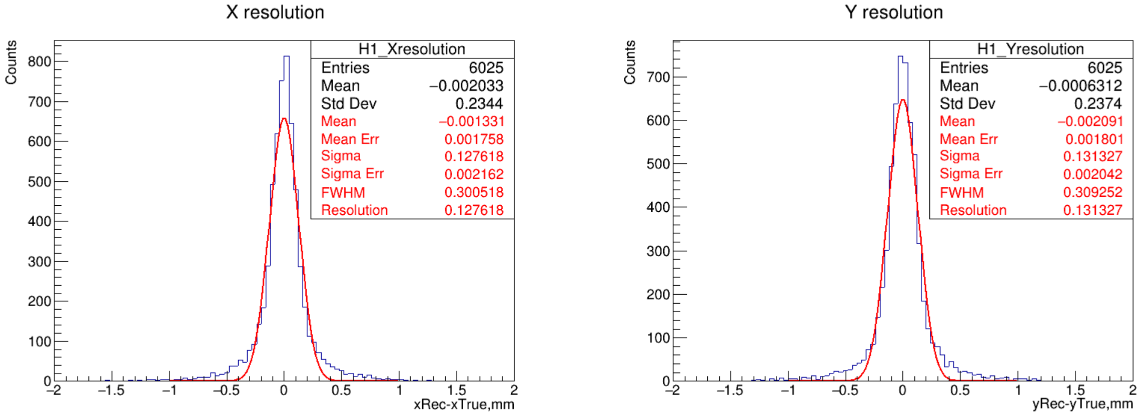

Figure 6.13: Resolutions in the x-direction (left) and in the y-direction (right) for the best design option: collimator *9a* with 1600-pixel SiPM, PTFE walls and 15 mm separation to the LXe surface.

---

[6] This can be remedied by using XY LRFs since the true LRFs of the sensors near the walls cease to be axial, so fitting it with an axial function introduces bias in the reconstruction.

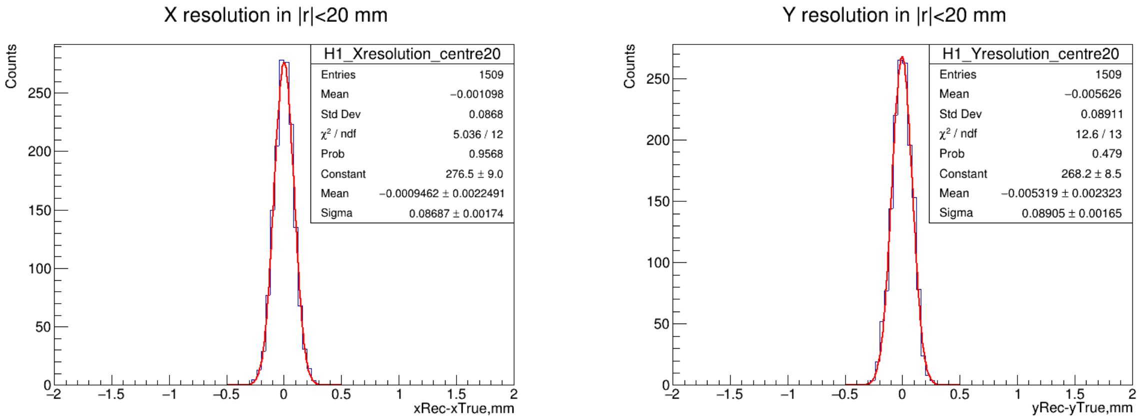

Figure 6.14: Resolutions in the x-direction (left) and in the y-direction (right) for the best design option, showing events only in the inner region of the LXe-TPC (r<20 mm).

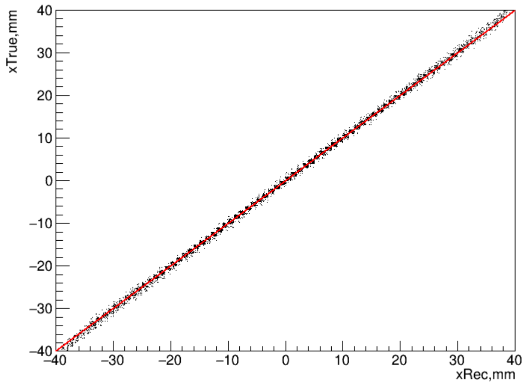

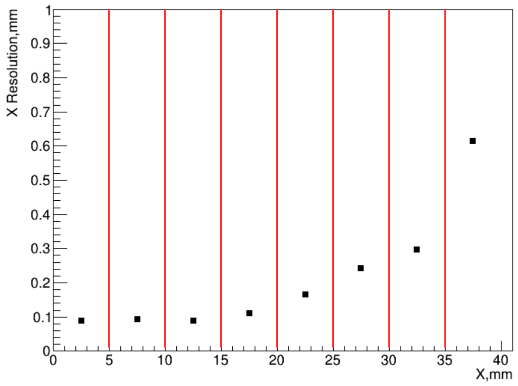

Figure 6.15: Reconstruction performance in the x-direction, analysed as true simulated position against reconstructed position.

Figure 6.16: Variation of the resolution (x-direction) from the centre of the chamber to the periphery, in radial slices of 5 mm.

SiPM tolerances in *(x,y)*

To test the effect of uncertainties due to mechanical tolerances affecting the positioning of individual silicon chips, a simulation was run with an array of spatially-shifted devices behind a perfectly aligned collimator: the centres of the sensors were shifted according to a Gaussian with $\sigma = 0.100$ mm in x and in y (i.e. 0.140 mm radially) truncated at a maximum absolute displacement of 0.300 mm for both coordinates; then the reconstruction LRFs were optimised and position was reconstructed again. The SiPMs will only be attached to the Kapton tape so most of the positional tolerance comes from the location of the chip within the ceramic carrier of the array. An average for the worst case scenario indicates that misplaced SiPMs would worsen resolution to a value of 216 μm, up from 124 μm for the same central region with r<20 mm (see Table 6.8).

However, in principle it should be possible to correct for this in the real detector since we will be able to change the LRFs parameters as necessary with the array already in place. During these optimisation tests, the LRFs were trained under the assumption that each SiPM was placed in a fixed position, and a possible solution would be to set unfixed positions for the centres of the LRFs thus overcoming the bias. From the tolerance tests it was found that errors inherent to the LRFs were more detrimental to the resolution rather than having a significant physical displacement. While analysing the data from one of the runs with a random shift in *(x,y)*, if reconstruction was calculated with LRFs from the shifted geometry, the resolution was 130 μm; but reconstructing the same set of events using LRFs from an ideal geometry (SiPMs perfectly centered with collimator apertures) lowered the resolution to 119 μm.

Additionally, a test run was made with the same systematic offset for all SiPMs, in which they were all shifted to the right by 0.15 mm. The histograms for this case are in Figure 6.17, and the outcome was a resolution of 130 μm, it barely declined in comparison to the ideal scenario of 124 μm. The noticeable change appeared in the mean value of the histogram, which shifted from 0 to ~0.5 mm. This bias introduced by the effect of parallax depends on the setup geometry (the parallax decreases as the distance between the source and the collimator increases) and could be corrected in post processing, although this was not tested.

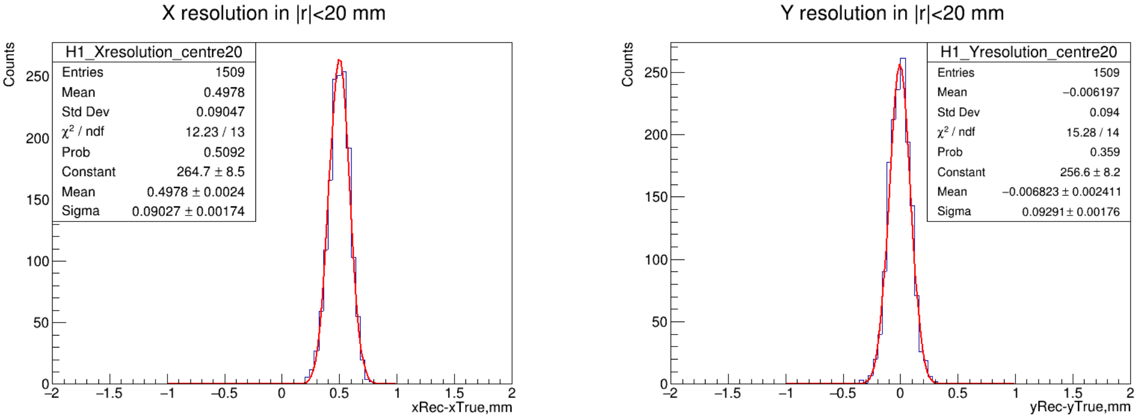

Figure 6.17: Resolution in the region of r<20 mm, in the x-direction (left) and in the y-direction (right) for the best design option, with all SiPMs systematically displaced to the right by 0.15 mm relative to the centre of the collimator holes.

SiPM tolerances in z

To test the effect of adding a short distance between the collimator exit and the front face of the SiPM chips, the best configuration was retested with this distance increased from 0 mm to 1 mm. The radial resolution in the centre of the LXe-TPC increased from 124 ± 2 μm to 139 ± 2 μm. If the separation was set to 0.5 mm instead, the resolution achieved would be 121 ± 2 μm, which falls inside the uncertainty.

Spatial resolution with varying energy

To complete the analysis, the performance with a decreasing number of photons was tested, to simulate the effect of "slicing" the S2 signal in time and lower S2 yield due to hydrogen doping (see subsection 5.2.2). The resolution degrades as expected, approximately as the square-root law expected from photon statistics as pictured in Figure 6.18; this is only partly offset by the less severe saturation cut which is required. A reasonable expectation for the case of H_2 doping is reducing the original number of photons by a factor of 8, which would decrease the resolution from 124 μm to 245 μm considering r $<$ 20 mm the central region of the detector.

Table 6.8: Summary of radial resolution for the final set of ANTS2 simulations (SiPM data is area resolved and corrected for saturation).

Photons (millions)	Observations	XY sampling	Z sampling	Total Radial Resolution (mm)	Central Radial Resolution for r<20 mm (mm)
6	No collimator	sobol seq.	20 rand. points	0.540 ± 0.007	0.376 ± 0.006
6	No grids	sobol seq.	20 rand. points	0.174 ± 0.002	0.103 ± 0.001
6	-	sobol seq.	20 rand. points	0.183 ± 0.002	0.124 ± 0.002
3	-	sobol seq.	20 rand. points	0.220 ± 0.002	0.165 ± 0.002
1.5	-	sobol seq.	20 rand. points	0.259 ± 0.002	0.193 ± 0.003
0.75	-	sobol seq.	20 rand. points	0.324 ± 0.003	0.245 ± 0.003
0.375	-	sobol seq.	20 rand. points	0.458 ± 0.004	0.341 ± 0.005
SiPMs with $(x,\ y)$ and z tolerances					
6	random shift in (x,y)	sobol seq.	20 rand. points	0.314 ± 0.003	0.216 ± 0.003
6	shift in x by adding 0.15 mm	sobol seq.	20 rand. points	0.200 ± 0.015	0.130 ± 0.002
6	space in z by adding 1 mm	sobol seq.	20 rand. points	0.197 ± 0.002	0.139 ± 0.002
6	space in z by adding 0.5 mm	sobol seq.	20 rand. points	0.176 ± 0.002	0.121 ± 0.002

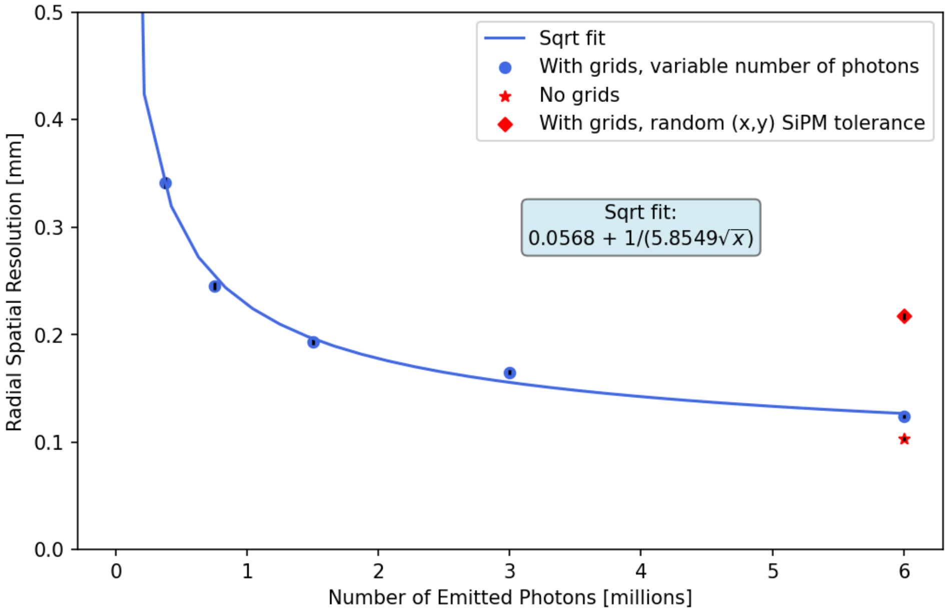

Figure 6.18: Radial resolution as a function of photon yield for r<20 mm for the best design (S13370-3075CN device, *9a* collimator, 15 mm to LXe surface, and finer gate and anode grids) and obtained square root fit.

As stated in the beginning of this chapter, the results presented were obtained considering 6 million S2 photons, meaning the resolutions are relative to one slice of the NDBD track. From the inverse square root fit in Figure 6.18, we can now extract the result for the total of 60 million photons corresponding to the resolution for the entire track: the radial resolution would be 79 μm and the linear resolution for x and y would be 56 μm.

Chapter 7

An End-to-End Simulation Tool

In order to study the detector response to different interactions, a complete simulation tool was developed capable of generating realistic waveforms that we would expect to obtain with Xenia. These simulated waveforms will allow us to understand other performance aspects and predict the behaviour of the detector before its construction and operation, for instance on the minimum vertical vertex separation of an event, test the effect that different drift velocities have on position resolution, and even study calibration sources that might be used in the real detector.

As mentioned at the end of Chapter 5, the foundation for this was the ANTS2 software with Geant4 integration, complemented by the use of NEST. This tool can be used to study other dual phase TPC detectors other than Xenia by changing some physics parameters (e.g. electric fields, temperature, pressure, factor g_1[1] and g_2 is calculated internally by NEST from the aforementioned parameters) and defining the proper geometry in ANTS2. In the following sections, the operation of the main blocks of the simulation are explained, and a complete flowchart summarising the code can be found in the Appendix.

7.1 Event Processing

The initial configuration of the simulation includes, for instance, the random seed generator, number of events, primary particle specification, size of time bins for waveforms digitalisation, the interaction type and electric field regions. To speed up the computing time for photon propagation there is an option to choose the number of threads and an option to perform down-sampling and rescaling on the S2 pulse.

Each event presented here was simulated in time-resolved mode with 10 ns digitalisation and the interaction type used for all events was ER β interactions, including Comptons. NEST requires initialising a detector class which emulates the same characteristics of the ANTS2 geometry, and additionally allows to add other methods and variables not contemplated in ANTS2. More details on the function of this NEST class are given further ahead.

7.1.1 Particle sources

The user can define particle sources and choose the type, energy, position, direction and number of particles. The information for each source is written to a file which ANTS2 uses for primary particle generation. Afterwards, the information in the file is sent to Geant4 where the sources

---

[1] Number of photons detected per S1 photons produced.

are propagated; the coordinates, time stamp and energy for each of the deposition sites is recorded and returned to ANTS2 to be grouped into clusters (see next subsection).

7.1.2 Clustering of energy depositions

Clusters are determined with the DBSCAN[2] algorithm, which is very efficient in finding arbitrarily shaped clusters based on their local density. The implementation of DBSCAN used here is from *scikit-learn* and takes two arguments: the minimum number of samples (n) required to construct a cluster, and the maximum radial distance between each sample (ϵ). Considering a point P from a set, if there are n or more samples within the area delineated by ϵ centered at P, they are considered core samples, or neighbours of P. Consequently, a cluster is a set of core samples together with a set of non-core samples located at the edges of the high density region [Kha+14]. The points that do not fit these conditions are labeled as noise (considered as a cluster made of a single interaction point). Figure 7.1 shows a visual representation of data clustering by DBSCAN.
In the simulations presented here, the $\epsilon = 0.025$ mm and $n = 3$ and each point is weighed by its deposited energy. The average centre, timing and total energy of each cluster is calculated and saved in an object, as well as the information on noise samples, so that they are all simulated and analysed.

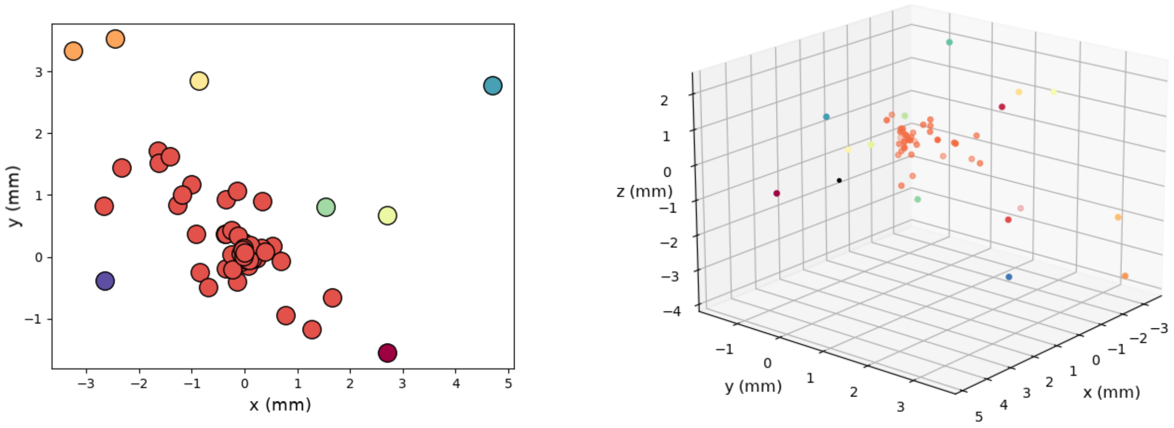

Figure 7.1: Example of data clustering by DBSCAN shown in the *(x,y)* plane (left) and in 3D (right). Points represented with the same colour belong together in a cluster and points with single colours are considered noise.

7.1.3 Identification of bremsstrahlung interactions

Bremsstrahlung is a problem in NDBD and β interactions of the MeV energy range. This happens when a charged particle is deflected from its path due to the influence of another charge, losing kinetic energy that is released in the form of a γ photon. As a consequence, this leads to the appearance of a secondary track (originating from the bremsstrahlung γ-ray capture), disjointed from the primary track, which can increase the uncertainty when reconstructing the event. As seen in Figure 7.2, the yields depend on the incident energy, so to obtain the correct yields it is necessary to subtract the energy deposited in the medium from the incident energy, doing so for all consecutive interactions. However, if there is a bremsstrahlung interaction along the way, this breaks up the chain of calculation, so we need to distinguish which interactions come from this process. Therefore, a method was created in an attempt to separate β ER from

---

[2] Density-Based Spatial Clustering of Applications with Noise

bremsstrahlung ER before clustering.

Ideally, this could have been done by using the ANTS2 built-in functions that give information on the particle history (retrieved from Geant4). However, this was not possible to achieve due to the way the simulation is structured. Therefore, the solution arranged for this consisted in searching for the minimum distance between every two clusters obtained previously. If the minimum distance is larger than 0.2 mm, then that far away cluster is considered to be an interaction from a bremsstrahlung photon, and another method will check if this is part of a series of interactions by said photon by iteratively comparing if the minimum distance is smaller than 2 mm for the remaining clusters.

These values were determined by plotting a histogram with the distances between clusters of 400 different events. There were two distinct populations, which allowed to define the distance from a bremsstrahlung interaction to the main track and the distance between bremsstrahlung neighbours located far from the track. The minimum distance between two clusters in the main track cannot exceed 0.2 mm, and the distance between bremsstrahlungs close to each other should be smaller than 2 mm. With this information it is now possible to reconstruct the trajectories and calculate the energy of the particles before each interaction.

7.1.4 Light and charge Yields

After gathering all energy depositions within each cluster, the number of photon and electron quanta as well as the emission times of photons is obtained using NEST. The final light and charge yields for an individual cluster are calculated by subtracting the NEST yields with the initial energy from the NEST yields with the remaining energy after an interaction.

The propagation of S1 light is done using ANTS2 methods: an optical photon is added for each photon quanta, positioned at the centre coordinates of its parent cluster, with its characteristic emission time. ANTS2 then runs the photon sources for one cluster, propagates light isotropically and computes the number of photons detected by SiPMs and PMTs, which constitute the timed light signals. ANTS2 built-in functions are called to properly retrieve the time resolved signals from each photosensor which are then summed over all the clusters. Simulation and collection of S2 light is achieved in the same manner: after drift and diffusion of the electron cloud, extraction to the gas phase and calculating the amount of photons produced per extracted electron, the emission times of photons and coordinates can be obtained and electroluminescence can be simulated isotropically (explaned further in the next subsection).

NEST calculates the yields through a simplified Platzmann equation $E_{dep} = N_i(\alpha W_{ex} + W_i)$, derived from Chapter 4. Since S1 and S2 yields are anti-correlated, accurately modelling the recombination probability of ionisation electrons is crucial for simulating realistic yields. The plots representing the yields modelled by NEST for ER β interactions are in Figure 7.2.
Recombination physics is modelled in two parts: for long particle tracks and smaller LET, the derivation of Birk's Law [Dok+88] is applied; while for tracks shorter than the mean electron-ion thermalization distance, the Thomas-Imel Box model [SD11] is more appropriate. The exception is for low energy particles (high LET), where the box model applies at all times. A detailed explanation of the models and adjustments made can be found in [Szy+11].

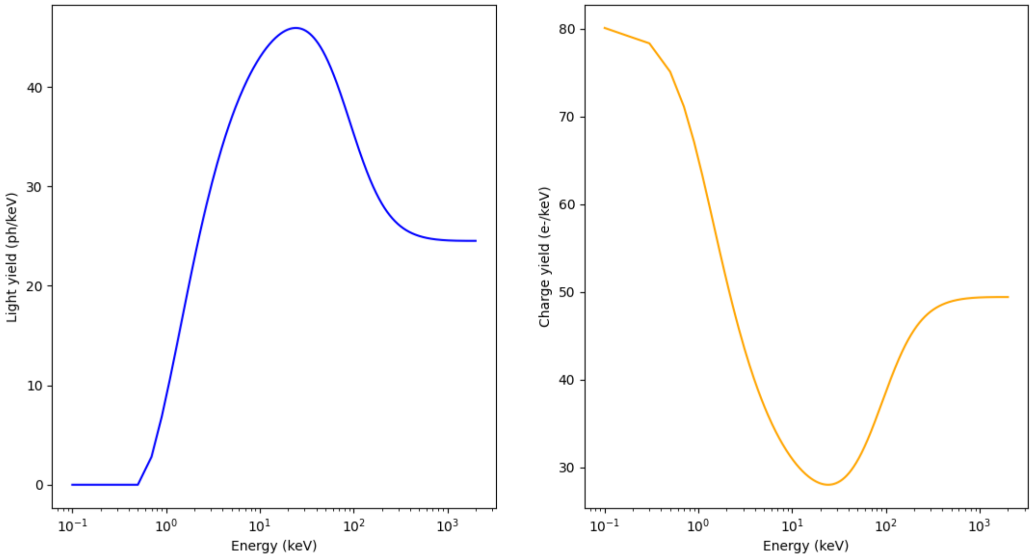

Figure 7.2: Light yield (left) and charge yield (right) as a function of incident energy for the primary particle source. These plots are relative to ER β interactions in Xenon for a drift field of 380 V/cm, the nominal conditions used in XENIA simulations.

To simulate a realistic pulse, information on the photon emission times is necessary, and NEST models this as well. The shape of the S1 signal is limited by singlet and triplet lifetimes, recombination time and ratio of single to triplet states. The lifetimes in the NEST model are 3.1 ± 0.7 ns and 24 ± 1 ns for singlet and triplet states respectively, and come from an error-weighted world average of published results. The ratio between the two states has been measured empirically [Moc+14]. The bigger the energy density per unit length transferred to a medium, the more ionized it becomes and as a consequence, the easier it is for an electron to recombine. This indicates that recombination time should be inversely proportional to LET, and although this is not fully accurate, NEST ignores other effects that contribute to this as they are not necessary to correctly adjust the data [Moc+14]. Recombination time is calculated from (7.1), the exponential factor is introduced to accommodate the quenching effect caused by the presence of an electric field [Moc+14]:

$$\tau_r = \left(\hat{\tau} \times \frac{1 + B \times LET}{A \times LET}\right) \times e^{-0.009E_f} = \tau_{r,0} \times e^{-0.009E_f} \ (ns) \tag{7.1}$$

where A and B are free parameters of the recombination probability, E_f is the electric field and $\hat{\tau}$ is a normalization factor which was determined to be 3.5 ns for electron recoils.

7.1.5 Diffusion of electrons

The diffusion of electrons implemented is a simplified model adapted from the NEST code, considering three uniform electric fields in the drift (liquid phase), the electroluminescence and extraction regions (gas phase). NEST models the coefficients for both transversal and longitudinal diffusion, in both LXe and GXe, as power law fits dependent on the applied electric field. The longitudinal component in the drift region has a predominant effect on the shape of the S2 pulse because it dictates the temporal distribution of electrons and hence the detection time of photons as well.

Under the 380 V/cm field, each ionisation electron is diffused from its current position on the cluster centre upwards to the LXe surface. The new location of the electron is obtained by adding small diffusion steps to its x, y and z coordinates as indicated in Equations (7.2), (7.3) and (7.4). The travel time of each electron is updated and summed at each step, dividing the distance travelled along the z direction by the electron drift velocity in that region, as shown in Equation (7.5). This iterative process models a realistic spread of the electron cloud. Between the gate and LXe surface, the same process is followed with the proper velocity and diffusion coefficients under the 5 kV/cm electric field.

$$x_{new} = x_{previous} + D_T cos(\phi) \tag{7.2}$$

$$y_{new} = y_{previous} + D_T sin(\phi) \tag{7.3}$$

$$z_{new} = z_{previous} + D_L \tag{7.4}$$

$$t_{drift} = \frac{\Delta z}{v_d} \tag{7.5}$$

The time it takes for an electron to overcome the energy barrier at the liquid/gas interface, and be extracted to the gas phase is reproduced through an exponential distribution, for which the time constant is taken from a quantum tunnelling probability [Moc+14]. This is also added to the electron travel time.

After recording the coordinates and times for when electrons reach the gas, the number of photons produced by each electron via electroluminescence is taken from a normal distribution with the yield as the mean, and the Fano factor[3] corrected yield as the standard deviation. NEST allows to obtain the values for gas extraction efficiency, electroluminescence yield[4], single electron size[5] and the factor g_2[6] Once more, a new set of electron coordinates and the travel times are determined, but now with velocity and diffusion coefficients for GXe in the 10 kV/cm field. For drift velocity in gas, NEST uses a constant velocity provided by look-up tables from the Magboltz package [Bia11].

The emission times of S2 photons are collected from NEST, the *(x,y)* position where they are emitted from corresponds to the last recorded coordinates of the electron and this information is passed on to ANTS2 optical photon nodes. After all photon sources are recorded, the light is propagated and the signal from the photosensors is retrieved and added iteratively until all S2 signals have been summed, as described in subsection 7.1.4.

7.1.6 Signals from SiPMs and PMTs

After photons are emitted, ANTS2 takes care of propagating them, from their initial coordinates and orientation, the distance to the next geometry interface is calculated. The processes taken into account by ANTS2 during photon propagation are absorption and scattering in the bulk volumes and absorption, specular or diffuse reflection at the material interfaces. The propagation process ends if the photon is absorbed, leaves the detector geometry, enters a photosensor or a maximum number of tracing cycles is reached. In ANTS2, the detection probability of a photosensor is given by the product of its quantum efficiency for the photon wavelength, the angular dependence and area dependence of the detection probability[7]. The number of detected photons is accumulated over consecutive time bins of 10 ns duration for each detector. The sequence of these time bins forms a time resolved waveform which is exported for each individual photosensor as well as the sum for the top and bottom arrays.

---

[3] Calculated by NEST.

[4] Number of photons produced per ionisation electron.

[5] Number of photons detected per electron extracted to the gas phase.

[6] Number of photons detected deriving from one ionisation electron removed from the interaction site.

[7] The angular response was not taken into account in these simulations.

All of the information on the event is flushed to 3 main output files: one with details on interaction points and clusters, another with waveform data and untimed signals for light maps, and most importantly a JSON file which contains all necessary data for analysis to be used in the MiDAQ[8] and MiDAS[9] tools, developed by the Dark Matter group from LIP-Coimbra [Ara+22]. The waveform can be plotted with ROOT[10] [BR97] graphing tools inside ANTS2 or using a separate script/tool to read the data in the files.

In order to assess the validity of waveforms generated by ANTS2, a few simulations were run independently with NEST and then compared to the equivalent event simulated with ANTS2 (performed with the same chamber geometry, same particle type, energy and position). Even though NEST allows to obtain waveforms for a specific interaction, it does not offer information on the signal of individual photosensors, crucial for position reconstruction. The result is in Figure 7.3, where the S2 signal for both waveforms is overlapped and shows good agreement between the two separate runs.

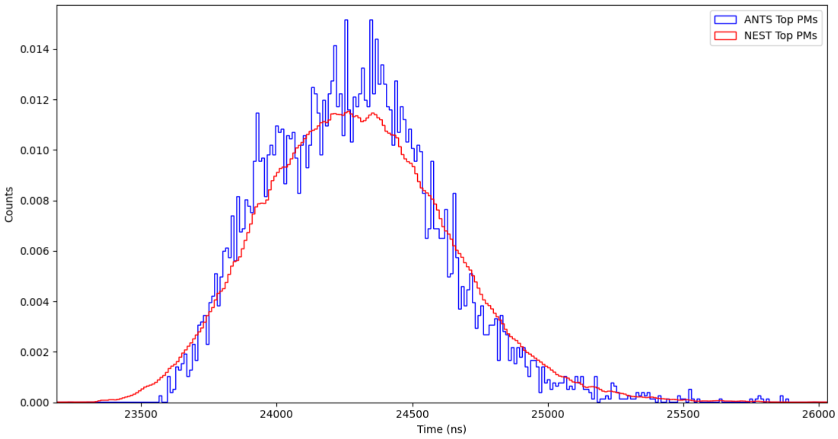

Figure 7.3: S2 signal of a 90 keV electron at the centre of the TPC, simulated by ANTS (blue) and by NEST (red). The counts in the y axis are normalised because simulations processed only in NEST consider PMTs as their sensors, as opposed to the SiPMs used in ANTS2.

7.2 Waveform Examples

Many events of interest to this work were simulated, and a few examples are presented here, namely an ideal NDBD event, a NDBD with Bremsstrahlung, and a single electron of 2.5 MeV.

7.2.1 $0\nu\beta\beta$

This event was generated by simulating two electrons of 1.25 MeV each, emitted from the same point and travelling in opposite directions. In this particular case, the event was set at the centre of the chamber, at $(x, y, z) = (0, 0, 0)$, which corresponds to a depth of 42.5 mm below the LXe surface, and direction vectors were $\vec{d}_{e_1^-} = (0, 0, 1)$ and $\vec{d}_{e_2^-} = (0, 0, -1)$).
Figure 7.4 shows the correspondent simulated pulse, in which the S2 signal displays two peaks corresponding to the two electrons: this pulse shape occurs due to the vertical direction of propagation as they have a large enough difference in arrival time to create separate peaks. Figure 7.6 shows the spatial visualisation of this event, where a black star marks the initial

---

[8] Migdal data acquisition software.

[9] Migdal data analysis software.

[10] ROOT is a data analysis framework developed by CERN.

position and the arrows indicate the directions of the two electrons along the tracks. The colour scale shows the intensity of energy deposition.

By taking the time difference between peaks in Figure 7.4 and the velocity in the drift region ($v_d = 1.69$ mm/μs), we can infer that the two major depositions took place approximately 1.2 mm away from each other. This is observed in the 3D plot of Figure 7.6, where the two zones with the densest energy depositions are at $z \approx \pm 0.6$ mm.

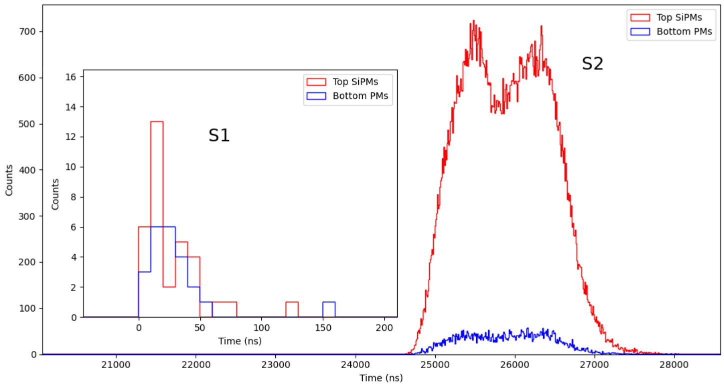

Figure 7.4: Waveform for a simulated NDBD event. The inset shows the S1 signal zoomed in.

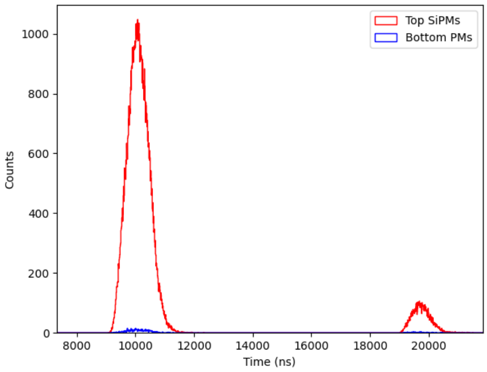

Figure 7.5: Waveform of the S2 signal for a simulated event of NDBD with bremsstrahlung.

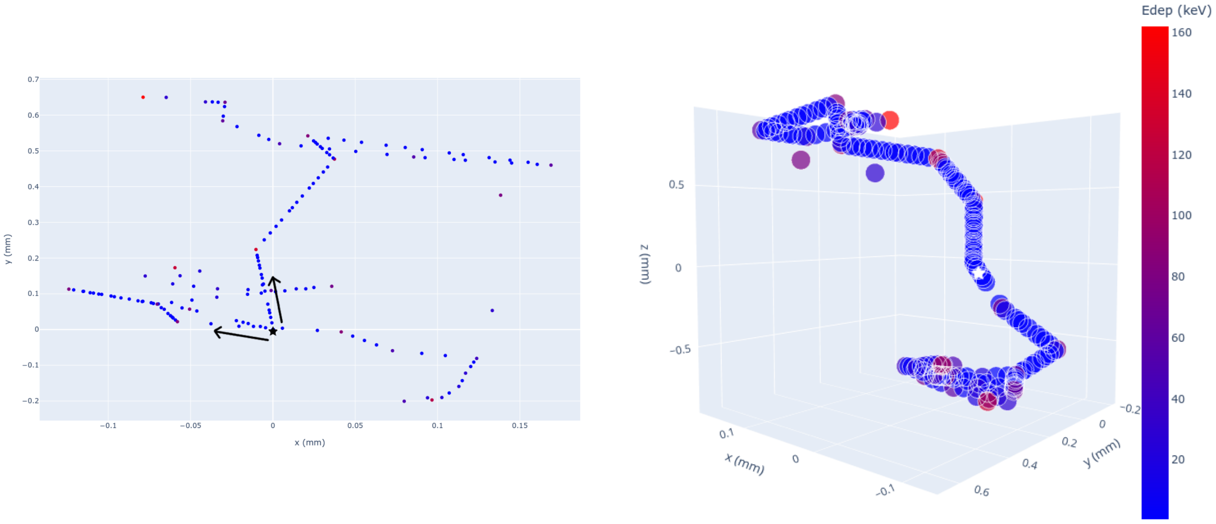

Figure 7.6: Spatial view of the simulated event for NDBD in the *(x,y)* plane (left) and in 3D (right).

Although a NDBD event can be easily identifiable like the one in Figure 7.4, it can also take the shape of a single peak, as the one in Figure 7.5. This event was simulated with origin at $(x, y, z) = (0, 0, 25)$ mm. The smaller peak on the right corresponds to a bremsstrahlung interaction that occurred far from the main track, which can be seen in Figure 7.7, where there are two outliers about 11 mm and 13 mm away from the source point. A light map of this event is shown in Figure 7.8, this is a downward view from the top of the TPC, which displays the number of detected photons in each SiPM (small squares) and PMT (large squares). The SiPMs with the stronger signals (red and orange) correspond to the region where the main track is located at $(x, y) = (0, 0)$ and the deviation of the signal intensity towards SiPM number 42 at $(x, y) = (-12, -12)$ (in light blue) is due to the bremsstrahlung interactions.

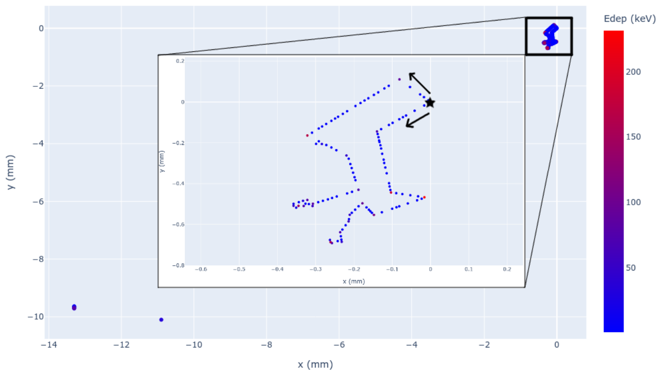

Figure 7.7: Spatial view of the simulated event of NDBD with bremsstrahlung in the *(x,y)* plane. The inset shows an expanded view of the main track in the upper right corner.

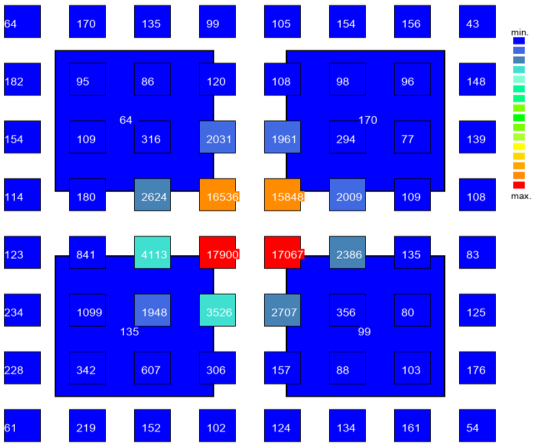

Figure 7.8: View of the light map from the simulated event of NDBD with bremsstrahlung.

7.2.2 Single Electron of 2.5 MeV

A single electron with the total energy of our $Q_{\beta\beta}$ of interest can also be a source of background. An example of the S2 signal for this event is shown in Figure 7.9, simulated at coordinates $(x, y, z) = (0, 0, -10)$ mm. A subtle bremsstrahlung peak can be seen in the waveform and clearly identified in the 3D visualisation from Figure 7.10. The *(x,y)* plane in the same figure shows a cleaner track followed by a single electron.

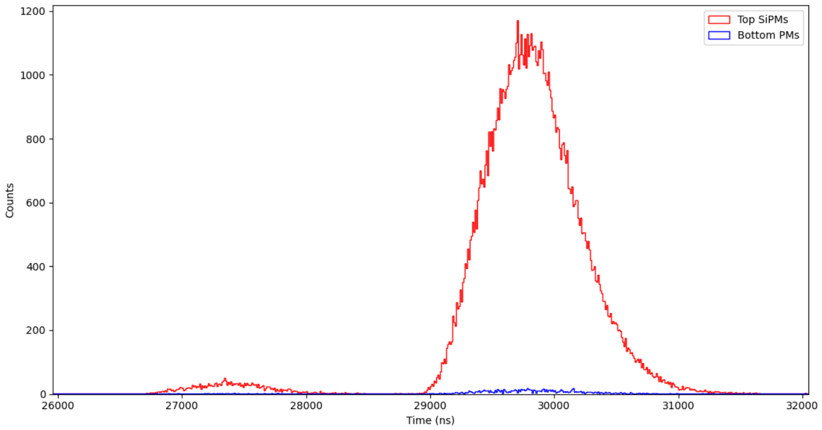

Figure 7.9: Waveform of the S2 signal for a simulated event with an electron of 2.5 MeV.

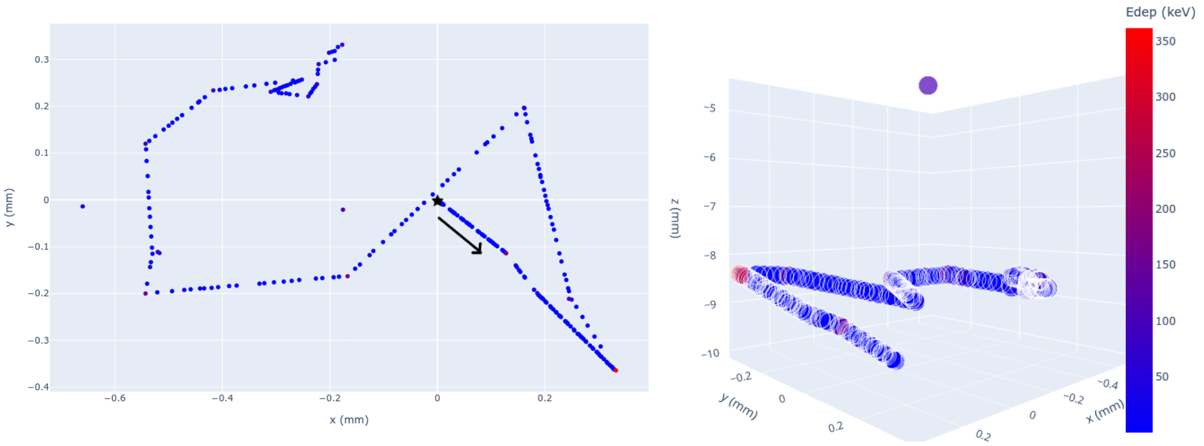

Figure 7.10: Spatial view of the simulated event for an electron of 2.5 MeV in the *(x,y)* plane (left) and in 3D where the dot at the top is the deposition point of the bremsstrahlung (right).

7.2.3 Downsampling

With the purpose of further testing the feasibility of the simulation tool developed here and to produce a more complete study of the simulated waveforms, the next step would be to generate thousands of events and perform a statistical analysis. However, this was not possible to accomplish for this work as it was found that this process was computationally intensive and required more computational resources than currently available as well as improvements to the ANTS2 software.

A possible solution to lighten the computational process was to reduce the amount of simulated S2 photons for each cluster via a downsampling probability. This was implemented by determining that for a larger amount of photons produced per S2 electron, ANTS2 would simulate a smaller number of photons, in such a way that ANTS2 would only trace a percentage of the photon yield for each electron. This was implemented by assigning a downsampling probability for the photons, as described in Equation (7.6)[11]. N_{ph} is the number of original photons and $N_{sim} = N_{ph} \times P_{DS}$ is the amount of simulated photons by ANTS2. After S2 light propagation, the waveform is rescaled to match one where all of the light would have been simulated.

$$P_{DS} = 43.04\ N_{ph}^{-0.503},\ for\ N_{ph} > 1 \times 10^4 \tag{7.6}$$

The downsampling option was tested in a simplified geometry and it is possible to run the simulation with or without this feature. Figure 7.11 shows an example of an event simulated with both options and it is clear that the two waveforms overlap and are relative to the same event although there is a slight offset in the amplitude during rising time, which could be investigated by applying a smoothing function over the pulse. The biggest difference is the expected increase in fluctuations which translates as noise.

Figure 7.12 shows the histogram of the pulse areas for a collection of 2000 events with downsampling (red solid line) and 2000 without downsampling (blue solid line). The two samples clearly belong to the same population, which indicates that the downsampling algorithm could work and be used comfortably to reduce computational time. Although these results are promising, similar tests such as this performed with the Xenia geometry did not show such an agreement. Therefore, we deem these preliminary results inconclusive and in need of further investigation and improvement of the downsampling process.

---

[11] The numeric values in the formula were obtained by making a fit to the desired values (e.g. for 1×10^4 photons, have the downsampling be ∼40%, for 5×10^4 photons reduce to ∼20% and so forth).

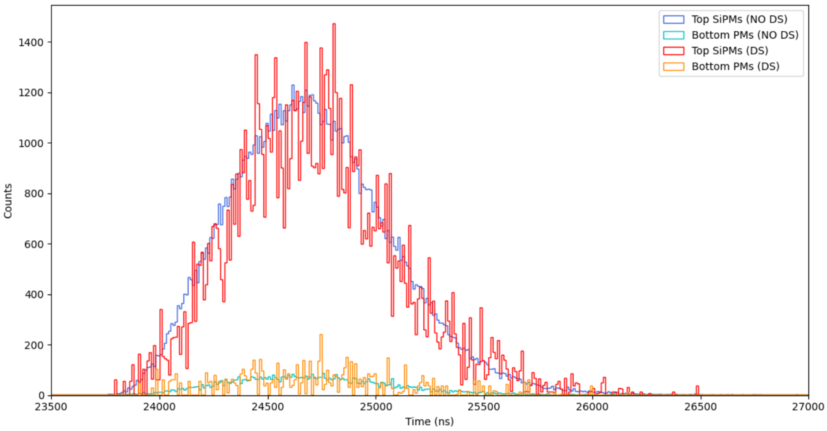

Figure 7.11: Comparison of an S2 pulse without downsampling (NO DS) plot in blue and cyan and with downsampling (DS) plot in red and orange. The waveform is for a simulated electron of 1.25 MeV in the centre of the chamber.

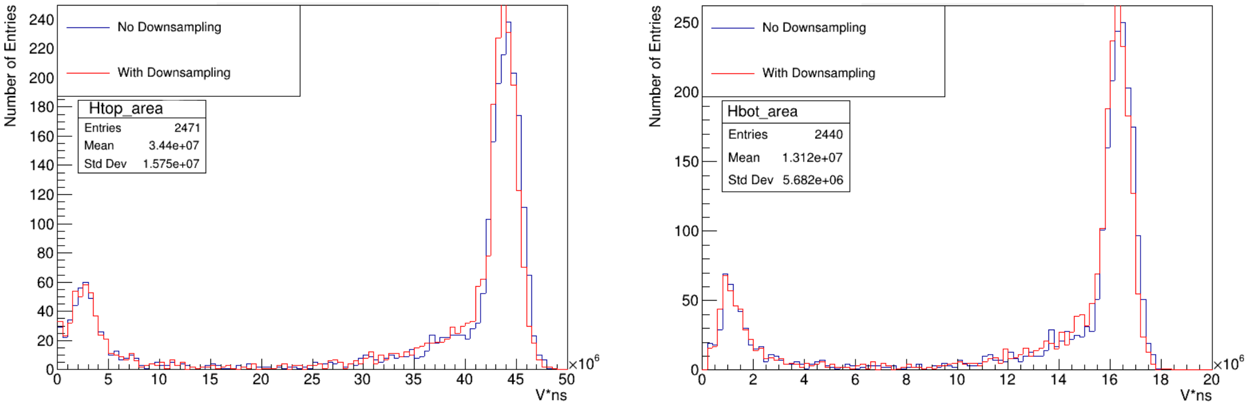

Figure 7.12: Total pulse areas for the signals obtained from the top photosensor array (left) and for the bottom array. The blue line corresponds to the sample without reducing the number of photons and the red line represents the sample where downsampling and rescaling were performed.

Despite the drawbacks, the simulation tool is functional and was still tested within the possibilities and resources at hand. For instance, the data analysis framework of MiDAQ and MiDAS were briefly used to process data and explore pulse separation in simulated waveforms. This was intended for studying separation of single and multiple scatters, minimum vertical vertex separation and more. Events simulated with this tool have already been used for studies like the one from Figure 5.7 in Chapter 5. The way this simulation is structured allows it to be used in future works regarding LXe dual phase TPCs.

Chapter 8

Conclusions

Rare event searches such as neutrinoless double beta decay are some of the most interesting subjects being studied in particle physics at the moment. Observation of the neutrinoless decay would truly revolutionise Standard Model physics and shift our understanding of the Universe, opening a path for a whole new field of study. Even though their decay lifetime is extremely slow and the experimental requirements for a detector with enough sensitivity capable of detection at this energy range are extremely demanding and pushing the limits of engineering, there are promising preliminary studies that show detecting these rare events may be possible.

The state of the art experiments in the field have already reached sensitivities that are beginning to probe the inverted mass hierarchy region such as KamLAND-Zen and in 10 years time nEXO expects to completely exclude this region. The first science run of the dark matter experiment LZ has achieved an unprecedented energy resolution of 0.65% on the energy region of interest for NDBD searches in ^{136}Xe [Per22a]. One of the 3^{rd} generation experiments already underway in the planning stage is XLZD, which joins the expertise of 3 existing collaborations, XENON, LZ and DARWIN. As mentioned in Chapter 5, their preliminary sensitivity projections indicate that they could reach a sensitivity to NDBD of $T^{0\nu}_{1/2} = 8.9 \times 10^{27}$ years, ruling out the IH of neutrinos [Lin22].

The original goal of this project was to design, simulate and optimise a dual-phase Xenon TPC for NDBD R&D studies in ^{136}Xe, using SiPMs and PMTs as light detectors.
Throughout this work, an end-to-end simulation tool was developed using the ANTS2 package with Geant4 and NEST, capable of simulating various aspects of the detector response, from particle tracking to the generation of light maps and realistic waveforms. This tool was tested with a model geometry of Xenia (the Imperial College prototype TPC), including all relevant physics, namely: uniform electric fields, diffusion of charges, propagation of light, bremsstrahlung identification and response of SiPMs and PMTs. The tests confirmed the tool correctly mirrors the interactions of interest for NDBD and is ready to use in future works, albeit some adjustments are needed to the ANTS2 software.

The Xenia TPC was also optimised for using SiPMs and a collimator in order to check the possibility of reaching 100 μm in *(x,y)* spatial resolution. This was tested by running sets of simulations featuring geometries with slightly different parameters and assessing their impact on the resolution. The results revealed that a radial resolution of ~124 μm is possible with a parallel hole collimator with 5.2 to 4.2 mm conically shaped apertures and combined with 64 SiPMs from Hamamatsu in the model S13370-3075CN in an 8×8 arrangement with 8 mm pitch, located 10 mm above the anode plane. The electrode grids found to be more beneficial for the resolution were very fine and dense, the gate with 0.05 mm wires and 200 lines per inch, and the anode having 0.03 mm wires and 180 lines per inch. The resolution declines to $\sim$ 245 μm in H_2-doped Xenon.

Developing the simulation tool within ANTS2 presented several challenges during this thesis, the main one being the computational time spent to process a large number of events, even while using multi-threading. This delayed the development and prevented gathering enough simulated events to perform a statistical analysis of particle tracks and waveforms. This is partly due to the high amount of information recorded by ANTS2 for a single event, which demands very large memory consumption, putting a severe penalty on the computer performance. Downsampling was introduced as a way to mitigate this, but further improvements are necessary for the simulation to accurately reproduce the same waveform that would be generated without downsampling. For instance, the time spent processing (propagation and recording timed photosensor signals) 20 million photons in the prototype geometry takes 30 seconds but only $\sim$0.5 seconds with downsampling and rescaling. A larger geometry corresponding to a 3^{rd} generation detector was also tested and in this case, the same amount of photons took 10 minutes without downsampling and 5 minutes with the reduction.

Scaling the detector to a larger size is the subject of the future milestone of Xenia, along with the use of machine learning to develop signal/background discrimination algorithms and study event topology. The simulation tool should also be modified to include mapping of non-uniform electric field areas, by using a multiphysics toolkit such as COMSOL or Garfield.
After the Xenia detector is fully characterised through simulations, installation and calibrations will ensue at the Imperial laboratories, where data acquisition can finally take place and the analysis of real data can begin.

This work presents a small contribution to the Xenia project which is a relevant study for the enhancement of this detector technology and algorithms for data analysis. The qualifications acquired during this dissertation are extensive and valuable for future work in the field of engineering and physics, inside and outside academia. Broadly speaking, general programming skills were improved with Python and C++, along with learning to use Docker environments and Gitlab. Specific tools used in particle physics simulations like Geant4, NEST and ANTS2 were explored for the first time which allowed to learn how to navigate lengthy software documentation. The continuous use of ANTS2 meant that there was active participation in reporting issues and contributing to resolve them, including giving feedback for the newest version under development, ANTS3. There was also some experience with data processing and analysis using ROOT and MiDAS, important for scientific training. Working within a research group which is inserted in major scientific collaborations presented a great opportunity to develop soft skills and participate in outreach activities, contributing to better communication skills.

List of Figures

List of Tables

References

[AAa21] J. Aalbers, F. Agostini, and et al. "A 3rd generation liquid xenon TPC dark matter experiment sensitivity to neutrino properties: magnetic moment and $0\nu\beta\beta$ decay of 136Xe. Snowmass2021 - Letter of Interest". 2021. URL: `https://www.snowmass21.org/docs/files/summaries/NF/SNOWMASS21-NF5_NF0_Matthew_Szydagis-156.pdf`.

[Aal+16] J. Aalbers et al. "DARWIN: towards the ultimate dark matter detector". In: *Journal of Cosmology and Astroparticle Physics* 2016.11 (Nov. 2016), pp. 017–017. DOI: `10.1088/1475-7516/2016/11/017`. URL: `https://doi.org/10.1088%2F1475-7516%2F2016%2F11%2F017`.

[Aal+22] J. Aalbers et al. *A Next-Generation Liquid Xenon Observatory for Dark Matter and Neutrino Physics.* 2022. DOI: `10.48550/ARXIV.2203.02309`. URL: `https://arxiv.org/abs/2203.02309`.

[Aar+18] Mark Aartsen et al. "Multimessenger observations of a flaring blazar coincident with high-energy neutrino IceCube-170922A". In: *Science* 361.6398 (July 2018). ISSN: 1095-9203. DOI: `10.1126/science.aat1378`. URL: `http://dx.doi.org/10.1126/science.aat1378`.

[Aba+15] K.N. Abazajian et al. "Neutrino physics from the cosmic microwave background and large scale structure". In: *Astroparticle Physics* 63 (Mar. 2015), pp. 66–80. ISSN: 0927-6505. DOI: `10.1016/j.astropartphys.2014.05.014`. URL: `http://dx.doi.org/10.1016/j.astropartphys.2014.05.014`.

[Abb+10] R. Abbasi et al. "MEASUREMENT OF THE ANISOTROPY OF COSMIC-RAY ARRIVAL DIRECTIONS WITH ICECUBE". In: *The Astrophysical Journal* 718.2 (July 2010), pp. L194–L198. ISSN: 2041-8213. DOI: `10.1088/2041-8205/718/2/l194`. URL: `http://dx.doi.org/10.1088/2041-8205/718/2/L194`.

[Abb+11] R. Abbasi et al. "Measurement of the atmospheric neutrino energy spectrum from 100 GeV to 400 TeV with IceCube". In: *Physical Review D* 83.1 (Jan. 2011). ISSN: 1550-2368. DOI: `10.1103/physrevd.83.012001`. URL: `http://dx.doi.org/10.1103/PhysRevD.83.012001`.

[Abe+21] K. Abe et al. "Diffuse supernova neutrino background search at Super-Kamiokande". In: *Physical Review D* 104.12 (Dec. 2021). ISSN: 2470-0029. DOI: `10.1103/physrevd.104.122002`. URL: `http://dx.doi.org/10.1103/PhysRevD.104.122002`.

[AD10] E. Aprile and T. Doke. "Liquid xenon detectors for particle physics and astrophysics". In: *Reviews of Modern Physics* 82.3 (July 2010), pp. 2053–2097. ISSN: 1539-0756. DOI: `10.1103/revmodphys.82.2053`. URL: `http://dx.doi.org/10.1103/RevModPhys.82.2053`.

[Adh+21] G Adhikari et al. "nEXO: neutrinoless double beta decay search beyond 10^{28} year half-life sensitivity". In: *Journal of Physics G: Nuclear and Particle Physics* 49.1 (Dec. 2021), p. 015104. DOI: `10.1088/1361-6471/ac3631`. URL: `https://doi.org/10.1088%2F1361-6471%2Fac3631`.

[Ago+03] S. Agostinelli et al. “Geant4—a simulation toolkit”. In: *Nuclear Instruments and Methods in Physics Research Section A: Accelerators, Spectrometers, Detectors and Associated Equipment* 506.3 (2003), pp. 250–303. ISSN: 0168-9002. DOI: `https://doi.org/10.1016/S0168-9002(03)01368-8`. URL: `https://www.sciencedirect.com/science/article/pii/S0168900203013688`.

[Ago+13] M. Agostini et al. “Results on Neutrinoless Double-β Decay of ^{76}Ge from Phase I of the GERDA Experiment”. In: *Phys. Rev. Lett.* 111 (12 Sept. 2013), p. 122503. DOI: `10.1103/PhysRevLett.111.122503`. URL: `https://link.aps.org/doi/10.1103/PhysRevLett.111.122503`.

[Ago+20] M. Agostini et al. “Final Results of GERDA on the Search for Neutrinoless Double-β Decay”. In: *Phys. Rev. Lett.* 125 (25 Dec. 2020), p. 252502. DOI: `10.1103/PhysRevLett.125.252502`. URL: `https://link.aps.org/doi/10.1103/PhysRevLett.125.252502`.

[Ago+22] Matteo Agostini et al. *Toward the discovery of matter creation with neutrinoless double-beta decay.* 2022. DOI: `10.48550/ARXIV.2202.01787`. URL: `https://arxiv.org/abs/2202.01787`.

[Ago15] M. Agostini. “Results on $\beta\beta$ decay with emission of two neutrinos or Majorons in ^{76}Ge from GERDA Phase I”. In: *Eur. Phys. J.* C75 (Sept. 2015), p. 416. DOI: `10.1140/epjc/s10052-015-3627-y`.

[AH02] I.J.R. Aitchison and A.J.G. Hey. *Gauge Theories in Particle Physics. From Relativistic Quantum Mechanics to QED.* 3rd edition. Vol. 1. Graduate Student Series in Physics. CRC Press, 2002. ISBN: 9780849387753. URL: `https://books.google.pt/books?id=vLP7XN2pWlEC`.

[AH04] I.J.R. Aitchison and A.J.G. Hey. *Gauge Theories in Particle Physics. Non-Abelian Gauge Theories: QCD and the Electroweak Theory.* Ed. by DPhil Professor Douglas F Brewer MA. 3rd edition. Vol. 2. Bristol and Philadelphia: INSTITUTE OF PHYSICS PUBLISHING, 2004. Chap. 12.3.2, 20.3, 20.4. ISBN: 0 7503 0950 4.

[Ahm+02] Q. R. Ahmad et al. “Direct Evidence for Neutrino Flavor Transformation from Neutral-Current Interactions in the Sudbury Neutrino Observatory”. In: *Phys. Rev. Lett.* 89 (1 June 2002), p. 011301. DOI: `10.1103/PhysRevLett.89.011301`. URL: `https://link.aps.org/doi/10.1103/PhysRevLett.89.011301`.

[Aji+21] S. Ajimura et al. “Low background measurement in CANDLES-III for studying the neutrinoless double beta decay of Ca48”. In: *Physical Review D* 103.9 (May 2021). ISSN: 2470-0029. DOI: `10.1103/physrevd.103.092008`. URL: `http://dx.doi.org/10.1103/PhysRevD.103.092008`.

[Ake+13] D.S. Akerib et al. “The Large Underground Xenon (LUX) experiment”. In: *Nuclear Instruments and Methods in Physics Research Section A: Accelerators, Spectrometers, Detectors and Associated Equipment* 704 (Mar. 2013), pp. 111–126. DOI: `10.1016/j.nima.2012.11.135`. URL: `https://doi.org/10.1016%2Fj.nima.2012.11.135`.

[Ake+16] D. S. Akerib et al. “Tritium calibration of the LUX dark matter experiment”. In: *Physical Review D* 93.7 (Apr. 2016). DOI: `10.1103/physrevd.93.072009`. URL: `https://doi.org/10.1103%2Fphysrevd.93.072009`.

[Ake+17] D. S. Akerib et al. “Signal yields, energy resolution, and recombination fluctuations in liquid xenon”. In: *Physical Review D* 95.1 (Jan. 2017). DOI: `10.1103/physrevd.95.012008`. URL: `https://doi.org/10.1103%2Fphysrevd.95.012008`.

[Ake+20a] D. S. Akerib et al. “Discrimination of electronic recoils from nuclear recoils in two-phase xenon time projection chambers”. In: *Phys. Rev. D* 102 (11 Dec. 2020), p. 112002. DOI: `10.1103/PhysRevD.102.112002`. URL: `https://link.aps.org/doi/10.1103/PhysRevD.102.112002`.

[Ake+20b] D. S. Akerib et al. “Projected sensitivity of the LUX-ZEPLIN experiment to the neutrinoless double beta decay of Xe136”. In: *Physical Review C* 102.1 (July 2020). ISSN: 2469-9993. DOI: `10.1103/physrevc.102.014602`. URL: `http://dx.doi.org/10.1103/PhysRevC.102.014602`.

[Ake+20c] D. S. Akerib et al. “Projected WIMP sensitivity of the LUX-ZEPLIN dark matter experiment”. In: *Physical Review D* 101.5 (Mar. 2020). DOI: `10.1103/physrevd.101.052002`. URL: `https://doi.org/10.1103%2Fphysrevd.101.052002`.

[Alb+21] V. Albanese et al. “The SNO+ experiment”. In: *Journal of Instrumentation* 16.08 (Aug. 2021), P08059. ISSN: 1748-0221. DOI: `10.1088/1748-0221/16/08/p08059`. URL: `http://dx.doi.org/10.1088/1748-0221/16/08/P08059`.

[Ali+09] G. Alimonti et al. “The Borexino detector at the Laboratori Nazionali del Gran Sasso”. In: *Nuclear Instruments and Methods in Physics Research Section A: Accelerators, Spectrometers, Detectors and Associated Equipment* 600.3 (Mar. 2009), pp. 568–593. ISSN: 0168-9002. DOI: `10.1016/j.nima.2008.11.076`. URL: `http://dx.doi.org/10.1016/j.nima.2008.11.076`.

[All+06] J. Allison et al. “Geant4 developments and applications”. In: *IEEE Transactions on Nuclear Science* 53.1 (2006), pp. 270–278. DOI: `10.1109/TNS.2006.869826`.

[Alv+12] V. Alvarez et al. “NEXT-100 Technical Design Report (TDR). Executive summary”. In: *Journal of Instrumentation* 7.06 (June 2012), T06001–T06001. ISSN: 1748-0221. DOI: `10.1088/1748-0221/7/06/t06001`. URL: `http://dx.doi.org/10.1088/1748-0221/7/06/T06001`.

[An+12] F. P. An et al. “Observation of Electron-Antineutrino Disappearance at Daya Bay”. In: *Physical Review Letters* 108.17 (Apr. 2012). ISSN: 1079-7114. DOI: `10.1103/physrevlett.108.171803`. URL: `http://dx.doi.org/10.1103/PhysRevLett.108.171803`.

[Ant+19] G. Anton et al. “Search for Neutrinoless Double-Beta Decay with the Complete EXO-200 Dataset”. In: *Physical Review Letters* 123.16 (Oct. 2019). DOI: `10.1103/physrevlett.123.161802`. URL: `https://doi.org/10.1103%2Fphysrevlett.123.161802`.

[Apr+00] Elena Aprile et al. “Spectroscopy and imaging performance of the Liquid Xenon Gamma-Ray Imaging Telescope (LXeGRIT)”. In: *X-Ray and Gamma-Ray Instrumentation for Astronomy XI.* Ed. by Kathryn A. Flanagan and Oswald H. W. Siegmund. Vol. 4140. International Society for Optics and Photonics. SPIE, 2000, pp. 333–343. DOI: `10.1117/12.409129`. URL: `https://doi.org/10.1117/12.409129`.

[Apr+06a] E. Aprile et al. “Simultaneous Measurement of Ionization and Scintillation from Nuclear Recoils in Liquid Xenon for a Dark Matter Experiment”. In: *Physical Review Letters* 97.8 (Aug. 2006). DOI: `10.1103/physrevlett.97.081302`. URL: `https://doi.org/10.1103%2Fphysrevlett.97.081302`.

[Apr+06b] Elena Aprile et al. “Noble Fluids as Detector Media”. In: *Noble Gas Detectors.* John Wiley & Sons, Ltd, 2006. Chap. 2, pp. 7–32. ISBN: 9783527610020. DOI: `https://doi.org/10.1002/9783527610020.ch2`. eprint: `https://onlinelibrary.wiley.com/doi/pdf/10.1002/9783527610020.ch2`. URL: `https://onlinelibrary.wiley.com/doi/abs/10.1002/9783527610020.ch2`.

[Ara+22] H. M. Araújo et al. *The MIGDAL experiment: Measuring a rare atomic process to aid the search for dark matter.* 2022. DOI: `10.48550/ARXIV.2207.08284`. URL: `https://arxiv.org/abs/2207.08284`.

[Arm+20] E. Armengaud et al. "Precise measurement of $2\nu\beta\beta$ decay of ^{100}Mo with the CUPID-Mo detection technology". In: *The European Physical Journal C* 80.7 (July 2020). ISSN: 1434-6052. DOI: `10.1140/epjc/s10052-020-8203-4`. URL: `http://dx.doi.org/10.1140/epjc/s10052-020-8203-4`.

[Arn+16a] R. Arnold et al. "Measurement of the $2\nu\beta\beta$ decay half-life of ^{150}Nd and a search for $0\nu\beta\beta$ decay processes with the full exposure from the NEMO-3 detector". In: *Physical Review D* 94.7 (Oct. 2016). ISSN: 2470-0029. DOI: `10.1103/physrevd.94.072003`. URL: `http://dx.doi.org/10.1103/PhysRevD.94.072003`.

[Arn+16b] R. Arnold et al. "Measurement of the double-beta decay half-life and search for the neutrinoless double-beta decay of ^{48}Ca with the NEMO-3 detector". In: *Physical Review D* 93.11 (June 2016). ISSN: 2470-0029. DOI: `10.1103/physrevd.93.112008`. URL: `http://dx.doi.org/10.1103/PhysRevD.93.112008`.

[Ava+21] A. Avasthi et al. "Kiloton-scale xenon detectors for neutrinoless double beta decay and other new physics searches". In: *Physical Review D* 104.11 (Dec. 2021). DOI: `10.1103/physrevd.104.112007`. URL: `https://doi.org/10.1103%2Fphysrevd.104.112007`.

[Bal+13] A. B. Balantekin et al. *Neutrino mass hierarchy determination and other physics potential of medium-baseline reactor neutrino oscillation experiments.* 2013. arXiv: `1307.7419 [hep-ex]`.

[Bar+18] E. Baracchini et al. *PTOLEMY: A Proposal for Thermal Relic Detection of Massive Neutrinos and Directional Detection of MeV Dark Matter.* 2018. arXiv: `1808.01892 [physics.ins-det]`.

[Bar11] A. S. Barabash. "Experiment double beta decay: Historical review of 75 years of research". In: *Physics of Atomic Nuclei* 74.4 (Apr. 2011), pp. 603–613. ISSN: 1562-692X. DOI: `10.1134/s1063778811030070`. URL: `http://dx.doi.org/10.1134/S1063778811030070`.

[Bau+18] L. Baudis et al. "Characterisation of Silicon Photomultipliers for liquid xenon detectors". In: *Journal of Instrumentation* 13.10 (Oct. 2018), P10022–P10022. DOI: `10.1088/1748-0221/13/10/p10022`. URL: `https://doi.org/10.1088%2F1748-0221%2F13%2F10%2Fp10022`.

[BB89] A. Barabash and A. Bolozdynya. "How to detect the dark matter of te galaxy if it is made up of weakly interacting neutral particles with masses 1-10 GeV/c2". In: *JETP Leters* (1989). URL: `http://jetpletters.ru/ps/1117/article_16910.pdf`.

[Bel+14] G. Bellini et al. "Final results of Borexino Phase-I on low-energy solar neutrino spectroscopy". In: *Physical Review D - Particles, Fields, Gravitation and Cosmology* 89.11 (2014). ISSN: 1550-7998. DOI: `10.1103/PhysRevD.89.112007`.

[Ber+10] M.J. Berger et al., eds. *XCOM: Photon Cross Sections Database.* 2010.

[Ber+17] M.J. Berger et al., eds. *ESTAR database: Stopping Powers and Ranges for Electrons.* 2017.

[Bet+13] S. Betts et al. "Development of a Relic Neutrino Detection Experiment at PTOLEMY: Princeton Tritium Observatory for Light, Early-Universe, Massive-Neutrino Yield". In: (July 2013).

[Bha+12] Hyoung Chan Bhang et al. “AMoRE experiment: a search for neutrinoless double beta decay of 100Mo isotope with 40Ca100MoO4 cryogenic scintillation detector”. In: 2012.

[Bia11] Stephen Biagi. *Magboltz - transport of electrons in gas mixtures*. Version v11.11. 2011. URL: `https://magboltz.web.cern.ch/magboltz/`.

[Bia17] M. Biassoni. “Review of neutrinoless double beta decay experiments”. In: Neutrino Oscillation Workshop (NOW). (2016). Vol. 238.Session IV. 2017. DOI: `doi.org/10.22323/1.283.0059`.

[BR97] Rene Brun and Fons Rademakers, eds. *ROOT - An Object Oriented Data Analysis Framework*. A 389. Proceedings AIHENP’96 Workshop. Lausanne: Nucl. Inst. & Meth. in Phys. Res., 1997, pp. 81–86. URL: `https://root.cern/`.

[Brá16] P. Brás. *New physics phenomenology and development of data processing tools for the LZ Dark Matter direct search experiment. Ph.D. Thesis Proposal DAEPHYS doctoral programme in Physics*. Coimbra, 2016.

[Brá20] Paulo Brás. “Sensitivity to the NDBD of 136Xe and development of machine learning tools for pulse classification for the LUX-ZEPLIN Experiment”. In: 2020.

[CA13] V Chepel and H Araújo. “Liquid noble gas detectors for low energy particle physics”. In: *Journal of Instrumentation* 8.04 (Apr. 2013), R04001–R04001. DOI: `10.1088/1748-0221/8/04/r04001`. URL: `https://doi.org/10.1088/1748-0221/8/04/r04001`.

[Car+96] G Carugno et al. “A large liquid xenon time projection chamber for the study of the radiative pion decay”. In: *Nuclear Instruments and Methods in Physics Research Section A: Accelerators, Spectrometers, Detectors and Associated Equipment* 376.2 (1996), pp. 149–154. ISSN: 0168-9002. DOI: `https://doi.org/10.1016/0168-9002(96)00245-8`. URL: `https://www.sciencedirect.com/science/article/pii/0168900296002458`.

[Car18] L. Cardani. *Neutrinoless Double Beta Decay Overview*. 2018. arXiv: `1810.12828 [nucl-ex]`.

[CHa+68] G. CHarpak et al. “The use of Multiwire Proportional Counters to Select and Localize Charged Particles”. In: *Nuclear Instruments and Methods* (1968). URL: `https://home.cern/sites/default/files/2018-06/Charpak_MultiwireProportionalCounters.pdf`.

[Che+02] Vitaly Chepel et al. “Development of liquid xenon detectors for medical imaging”. In: (Dec. 2002). DOI: `10.1142/9789812705075_0003`.

[Chr+64] J. H. Christenson et al. “Evidence for the 2π Decay of the K_2^0 Meson”. In: *Phys. Rev. Lett.* 13 (4 July 1964), pp. 138–140. DOI: `10.1103/PhysRevLett.13.138`. URL: `https://link.aps.org/doi/10.1103/PhysRevLett.13.138`.

[Cle+98] Bruce T. Cleveland et al. “Measurement of the Solar Electron Neutrino Flux with the Homestake Chlorine Detector”. In: 496.1 (Mar. 1998), pp. 505–526. DOI: `10.1086/305343`. URL: `https://doi.org/10.1086/305343`.

[Col+16] NEXT Collaboration et al. *First proof of topological signature in the high pressure xenon gas TPC with electroluminescence amplification for the NEXT experiment*. 2016. arXiv: `1507.05902 [physics.ins-det]`.

[Col+17] nEXO Collaboration et al. “Sensitivity and Discovery Potential of nEXO to Neutrinoless Double Beta Decay”. In: (Oct. 2017).

[Col+18] nEXO Collaboration et al. *nEXO Pre-Conceptual Design Report*. 2018. arXiv: `1805.11142 [physics.ins-det]`.

[Col+21] NEXT Collaboration et al. *Measurement of the ^{136}Xe two-neutrino double beta decay half-life via direct background subtraction in NEXT*. 2021. arXiv: `2111.11091 [nucl-ex]`.

[Col14] EXO-200 Collaboration. "Search for Majorana neutrinos with the first two years of EXO-200 data". In: *Nature* 510.7504 (June 2014), pp. 229–234. ISSN: 1476-4687. DOI: `10.1038/nature13432`. URL: `http://dx.doi.org/10.1038/nature13432`.

[Col17] GERDA Collaboration. "Background-free search for neutrinoless double - β decay of ^{76}Ge with GERDA". In: *Nature* 544.7648 (Apr. 2017), pp. 47–52. ISSN: 1476-4687. DOI: `10.1038/nature21717`. URL: `http://dx.doi.org/10.1038/nature21717`.

[Col20] Borexino Collaboration. "Experimental evidence of neutrinos produced in the CNO fusion cycle in the Sun". In: *Nature* 587.7835 (Nov. 2020), pp. 577–582. ISSN: 1476-4687. DOI: `10.1038/s41586-020-2934-0`. URL: `http://dx.doi.org/10.1038/s41586-020-2934-0`.

[Cow+56] C. L. Cowan et al. "Detection of the Free Neutrino: a Confirmation". In: *Science* 124.3212 (1956), pp. 103–104. ISSN: 0036-8075. DOI: `10.1126/science.124.3212.103`. eprint: `https://science.sciencemag.org/content/124/3212/103.full.pdf`. URL: `https://science.sciencemag.org/content/124/3212/103`.

[CP13] O. Cremonesi and M. Pavan. *Challenges in Double Beta Decay*. 2013. arXiv: `1310.4692 [physics.ins-det]`.

[CSP12] Simon R. Cherry, James A. Sorenson, and Michael E. Phelps. "chapter 14 - The Gamma Camera: Performance Characteristics". In: *Physics in Nuclear Medicine (Fourth Edition)*. Ed. by Simon R. Cherry, James A. Sorenson, and Michael E. Phelps. Fourth Edition. Philadelphia: W.B. Saunders, 2012, pp. 209–231. ISBN: 978-1-4160-5198-5. DOI: `https://doi.org/10.1016/B978-1-4160-5198-5.00014-9`. URL: `https://www.sciencedirect.com/science/article/pii/B9781416051985000149`.

[DAk+21] D.Akerib et al. "HydroX- Using hydrogen doped in liquid xenon to search for dark matter. Snowmass2021 - Letter of Interest". 2021. URL: `https://www.snowmass21.org/docs/files/summaries/CF/SNOWMASS21-CF1_CF0_Hugh_Lippincott-106.pdf`.

[Dan+62] G. Danby et al. "Observation of High-Energy Neutrino Reactions and the Existence of Two Kinds of Neutrinos". In: *Phys. Rev. Lett.* 9 (1 July 1962), pp. 36–44. DOI: `10.1103/PhysRevLett.9.36`. URL: `https://link.aps.org/doi/10.1103/PhysRevLett.9.36`.

[Del+16] Stefano Dell'Oro et al. "Neutrinoless Double Beta Decay: 2015 Review". In: *Advances in High Energy Physics* 2016 (2016), pp. 1–37. ISSN: 1687-7365. DOI: `10.1155/2016/2162659`. URL: `http://dx.doi.org/10.1155/2016/2162659`.

[DLR67] B. Dolgoshein, V. Lebedenko, and B. Rodionov. "Luminescence Induced By Alpha Particle in Liquid Xenon in an Electric Field". In: *JETP Leters* (1967). URL: `http://jetpletters.ru/ps/1671/article_25479.pdf`.

[Dok+02] Tadayoshi Doke et al. "Absolute Scintillation Yields in Liquid Argon and Xenon for Various Particles". In: *Japanese Journal of Applied Physics* 41.Part 1, No. 3A (Mar. 2002), pp. 1538–1545. DOI: `10.1143/jjap.41.1538`. URL: `https://doi.org/10.1143/jjap.41.1538`.

[Dok+88] Tadayoshi Doke et al. "Let dependence of scintillation yields in liquid argon". In: *Nuclear Instruments and Methods in Physics Research Section A: Accelerators, Spectrometers, Detectors and Associated Equipment* 269.1 (1988), pp. 291–296. ISSN: 0168-9002. DOI: `https://doi.org/10.1016/0168-9002(88)90892-3`. URL: `https://www.sciencedirect.com/science/article/pii/0168900288908923`.

[DP18] A. De Angelis and M. Pimenta. *Introduction to Particle and Astroparticle Physics.* 2018.

[Dye+14] S. Dye et al. "Geo-neutrinos and Earth Models". In: *Physics Procedia* (May 2014). DOI: `10.1016/j.phpro.2014.12.050`.

[Edu11] Berkley Edu. *Nuclear Forensic Search Project.* Image by Wikipedia contributor BatesIsBack. 2011. URL: `https://metadata.berkeley.edu/nuclear-forensics/Decay%20Chains.html`.

[ESS12] Patrick Eckert, Rainer Stamen, and Hans-Christian Schultz-Coulon. "Study of the response and photon-counting resolution of silicon photomultipliers using a generic simulation framework". In: *Journal of Instrumentation - J INSTRUM* 7 (June 2012). DOI: `10.1088/1748-0221/7/08/P08011`.

[EV02] Steven R. Elliott and Petr Vogel. "DOUBLE BETA DECAY". In: *Annual Review of Nuclear and Particle Science* 52.1 (2002), pp. 115–151. DOI: `10.1146/annurev.nucl.52.050102.090641`. eprint: `https://doi.org/10.1146/annurev.nucl.52.050102.090641`. URL: `https://doi.org/10.1146/annurev.nucl.52.050102.090641`.

[Fer18] P. Ferrario. "Liquid xenon in nuclear medicine: state-of-the-art and the PETALO approach". In: *Journal of Instrumentation* 13.01 (Jan. 2018), pp. C01044–C01044. DOI: `10.1088/1748-0221/13/01/c01044`. URL: `https://doi.org/10.1088%2F1748-0221%2F13%2F01%2Fc01044`.

[FHL09] Pavel Fileviez Pérez, Tao Han, and Tong Li. "Testability of the type I seesaw mechanism at the CERN LHC: Revealing the existence of the $B - L$ symmetry". In: *Phys. Rev. D* 80 (7 Oct. 2009), p. 073015. DOI: `10.1103/PhysRevD.80.073015`. URL: `https://link.aps.org/doi/10.1103/PhysRevD.80.073015`.

[Fir49] E. L. Fireman. "A Measurement of the Half-Life of Double Beta-Decay from ${}_{50}\mathrm{Sn}^{124}$". In: *Phys. Rev.* 75 (2 Jan. 1949), pp. 323–324. DOI: `10.1103/PhysRev.75.323`. URL: `https://link.aps.org/doi/10.1103/PhysRev.75.323`.

[Fis12] Istituto Nazionale di Fisica Nucleare. *neutrini.* 2012. URL: `https://www.asimmetrie.it/en/tags/tag/52?start=40`.

[Fis18] Vincent Fischer. *Search for neutrinoless double-beta decay with SNO+.* 2018. arXiv: `1809.05986 [physics.ins-det]`.

[Fuk+98a] Y. Fukuda et al. "Evidence for Oscillation of Atmospheric Neutrinos". In: *Phys. Rev. Lett.* 81 (8 Aug. 1998), pp. 1562–1567. DOI: `10.1103/PhysRevLett.81.1562`. URL: `https://link.aps.org/doi/10.1103/PhysRevLett.81.1562`.

[Fuk+98b] Y. Fukuda et al. "Measurements of the Solar Neutrino Flux from Super-Kamiokande's First 300 Days". In: *Phys. Rev. Lett.* 81 (6 Aug. 1998), pp. 1158–1162. DOI: `10.1103/PhysRevLett.81.1158`. URL: `https://link.aps.org/doi/10.1103/PhysRevLett.81.1158`.

[Fur39] W. H. Furry. "On Transition Probabilities in Double Beta-Disintegration". In: *Phys. Rev.* 56 (12 Dec. 1939), pp. 1184–1193. DOI: `10.1103/PhysRev.56.1184`. URL: `https://link.aps.org/doi/10.1103/PhysRev.56.1184`.

[Gal+14] L. Galli et al. "Research and Development activities at INFN Pisa on a new drift chamber for the MEG experiment upgrade". In: *Nuclear Physics B - Proceedings Supplements* 248-250 (2014). 1st Conference on Charged Lepton Flavor Violation, pp. 112–114. ISSN: 0920-5632. DOI: `https://doi.org/10.1016/j.nuclphysbps.2014.02.020`. URL: `https://www.sciencedirect.com/science/article/pii/S0920563214000218`.

[Gan+16] A. Gando et al. "Search for Majorana Neutrinos Near the Inverted Mass Hierarchy Region with KamLAND-Zen". In: *Physical Review Letters* 117.8 (Aug. 2016). ISSN: 1079-7114. DOI: `10.1103/physrevlett.117.082503`. URL: `http://dx.doi.org/10.1103/PhysRevLett.117.082503`.

[Giu+14] Elena Giusarma et al. "Relic neutrinos, thermal axions, and cosmology in early 2014". In: *Physical Review D* 90.4 (Aug. 2014). ISSN: 1550-2368. DOI: `10.1103/physrevd.90.043507`. URL: `http://dx.doi.org/10.1103/PhysRevD.90.043507`.

[GM15] J. J. Gómez-Cadenas and Justo Martín-Albo. *Phenomenology of neutrinoless double beta decay.* 2015. arXiv: `1502.00581 [hep-ex]`.

[Goe35] M. Goeppert-Mayer. "Double Beta-Disintegration". In: *Phys. Rev.* 48 (6 Sept. 1935), pp. 512–516. DOI: `10.1103/PhysRev.48.512`. URL: `https://link.aps.org/doi/10.1103/PhysRev.48.512`.

[Gou+13] A. de Gouvea et al. *Neutrinos.* 2013. arXiv: `1310.4340 [hep-ex]`.

[Gru+14] L. Gruber et al. "Over saturation behavior of SiPMs at high photon exposure". In: *Nuclear Instruments and Methods in Physics Research Section A: Accelerators, Spectrometers, Detectors and Associated Equipment* 737 (2014), pp. 11–18. ISSN: 0168-9002. DOI: `https://doi.org/10.1016/j.nima.2013.11.013`. URL: `https://www.sciencedirect.com/science/article/pii/S0168900213015520`.

[Hil10] H J Hilke. "Time projection chambers". In: *Reports on Progress in Physics* 73.11 (Oct. 2010), p. 116201. DOI: `10.1088/0034-4885/73/11/116201`. URL: `https://doi.org/10.1088/0034-4885/73/11/116201`.

[Hir+87a] K. Hirata et al. "Observation of a neutrino burst from the supernova SN1987A". In: *Phys. Rev. Lett.* 58 (14 Apr. 1987), pp. 1490–1493. DOI: `10.1103/PhysRevLett.58.1490`. URL: `https://link.aps.org/doi/10.1103/PhysRevLett.58.1490`.

[Hir+87b] K. Hirata et al. "Observation of a neutrino burst from the supernova SN1987A". In: *Phys. Rev. Lett.* 58 (14 Apr. 1987), pp. 1490–1493. DOI: `10.1103/PhysRevLett.58.1490`. URL: `https://link.aps.org/doi/10.1103/PhysRevLett.58.1490`.

[IID18] Takashi IIDA. *First result of the CANDLES III experiment searching for double beta decay of 48Ca.* June 2018. DOI: `10.5281/zenodo.1300737`. URL: `https://doi.org/10.5281/zenodo.1300737`.

[Ind21] "Introduction to the Silicon Photomultiplier (SiPM)". In: AND9770/D (2021). Ed. by Semiconductor Components Industries. URL: `https://m.onsemi.jp/pub/collateral/and9770-d.pdf`.

[IR50] Mark G. Inghram and John H. Reynolds. "Double Beta-Decay of Te^{130}". In: *Phys. Rev.* 78 (6 June 1950), pp. 822–823. DOI: `10.1103/PhysRev.78.822.2`. URL: `https://link.aps.org/doi/10.1103/PhysRev.78.822.2`.

[Jac22] Elisa Elena Jacquet. Master Thesis. Imperial College of London, 2022.

[Jak20] Petr Jakubcik. *UROP Report/ANTS2 Manual.* Internship Report. Imperial College of London, 2020.

[Jam+18] A. Jamil et al. “VUV-Sensitive Silicon Photomultipliers for Xenon Scintillation Light Detection in nEXO”. In: *IEEE Transactions on Nuclear Science* 65.11 (Nov. 2018), pp. 2823–2833. DOI: `10.1109/tns.2018.2875668`. URL: `https://doi.org/10.1109%2Ftns.2018.2875668`.

[JK03] Stephen Joe and Frances Y. Kuo. “Remark on Algorithm 659: Implementing Sobol’s Quasirandom Sequence Generator”. In: *ACM Trans. Math. Softw.* 29.1 (Mar. 2003), pp. 49–57. ISSN: 0098-3500. DOI: `10.1145/641876.641879`. URL: `https://doi.org/10.1145/641876.641879`.

[KAJ10] Takaaki KAJITA. “Atmospheric neutrinos and discovery of neutrino oscillations”. In: *Proceedings of the Japan Academy, Series B* 86.4 (2010), pp. 303–321. DOI: `10.2183/pjab.86.303`.

[Kha+14] K. Khan et al. “DBSCAN: Past, present and future”. In: *The Fifth International Conference on the Applications of Digital Information and Web Technologies (ICADIWT 2014)*. 2014, pp. 232–238. DOI: `10.1109/ICADIWT.2014.6814687`.

[Kim+17] Inwook Kim et al. “Application of metallic magnetic calorimeter in rare event search”. In: *Superconductor Science and Technology* 30 (June 2017). DOI: `10.1088/1361-6668/aa7c73`.

[KL52] Marvin I. Kalkstein and W. F. Libby. “An Investigation of the Double Beta-Decay of ${}_{50}\mathrm{Sn}^{124}$”. In: *Phys. Rev.* 85 (2 Jan. 1952), pp. 368–369. DOI: `10.1103/PhysRev.85.368`. URL: `https://link.aps.org/doi/10.1103/PhysRev.85.368`.

[Kod+01] K. Kodama et al. “Observation of tau neutrino interactions”. In: *Physics Letters B* 504.3 (Apr. 2001), pp. 218–224. ISSN: 0370-2693. DOI: `10.1016/s0370-2693(01)00307-0`. URL: `http://dx.doi.org/10.1016/S0370-2693(01)00307-0`.

[Kut03] M.L. Kutner. *Astronomy: A Physical Perspective*. Cambridge University Press, 2003. ISBN: 9780521529273. URL: `https://books.google.pt/books?id=2QVmiMWOOOMC`.

[LAH17] Hugh Lippincott, Thomas Alexander, and Andrew Hime. “Increasing the sensitivity of LXe TPCs to dark matter by doping with helium or neon”. In: Feb. 2017, p. 285. DOI: `10.22323/1.282.0285`.

[Lan13] K.R. Lang. *Essential Astrophysics*. Undergraduate Lecture Notes in Physics. Springer Berlin Heidelberg, 2013. ISBN: 9783642359644. URL: `https://books.google.pt/books?id=CJfhsgEACAAJ`.

[Lin22] Alexandre Lindote. *XLZD: Towards a Global Rare Event Observatory*. Jornadas do LIP. Coimbra: University of Coimbra, 2022. URL: `https://indico.lip.pt/event/1183/contributions/4371/attachments/3472/5381/XLZD.pdf`.

[LO22] Alexandre Lindote and Ibles Olcina. *Sensitivity to neutrinoless double beta decay of Xe-136 with a third generation TPC dark matter experiment*. July 2022. DOI: `10.5281/zenodo.6805322`. URL: `https://doi.org/10.5281/zenodo.6805322`.

[Luq+17] A. Luqman et al. “Simulations of background sources in AMoRE-I experiment”. In: *Nuclear Instruments and Methods in Physics Research Section A: Accelerators, Spectrometers, Detectors and Associated Equipment* 855 (2017), pp. 140–147. ISSN: 0168-9002. DOI: `https://doi.org/10.1016/j.nima.2017.01.070`. URL: `https://www.sciencedirect.com/science/article/pii/S0168900217301602`.

[LY56] T. D. Lee and C. N. Yang. “Question of Parity Conservation in Weak Interactions”. In: *Phys. Rev.* 104 (1 Oct. 1956), pp. 254–258. DOI: `10.1103/PhysRev.104.254`. URL: `https://link.aps.org/doi/10.1103/PhysRev.104.254`.

[Maj08] Ettore Majorana. “Teoria simmetrica dell’elettrone e del positrone”. In: *Il Nuovo Cimento (1924-1942)* 14.4 (Sept. 2008), p. 171. ISSN: 1827-6121. DOI: `10.1007/BF02961314`. URL: `https://doi.org/10.1007/BF02961314`.

[Mer16] Susanne Mertens. “Direct Neutrino Mass Experiments”. In: 718 (May 2016), p. 022013. DOI: `10.1088/1742-6596/718/2/022013`. URL: `https://doi.org/10.1088/1742-6596/718/2/022013`.

[Mes] Balázs. Meszéna. *Neutrino Oscillations.* These images were created with Mathematica. The demonstration allows exploration of the parameters. URL: `https://demonstrations.wolfram.com/NeutrinoOscillations/`.

[Mes+02] Alex Meshik et al. “Double Beta Decay of Tellurium-130: Current Status”. In: (May 2002).

[MH06] D.-M. Mei and A. Hime. “Muon-induced background study for underground laboratories”. In: *Phys. Rev. D* 73 (5 Mar. 2006), p. 053004. DOI: `10.1103/PhysRevD.73.053004`. URL: `https://link.aps.org/doi/10.1103/PhysRevD.73.053004`.

[MH17] Albert Metz and Alfred Hogenbirk. “Optimal Shape of a Gamma-ray Collimator: single vs double knife edge”. In: *EPJ Web of Conferences* 153 (Jan. 2017), p. 07018. DOI: `10.1051/epjconf/201715307018`.

[MN78] Jay N. Marx and David R. Nygren. “The Time Projection Chamber”. In: *Phys. Today* 31N10 (1978), pp. 46–53. DOI: `10.1063/1.2994775`. URL: `https://escholarship.org/content/qt6w36n25j/qt6w36n25j.pdf`.

[Moc+14] J Mock et al. “Modeling pulse characteristics in Xenon with NEST”. In: *Journal of Instrumentation* 9.04 (Apr. 2014), T04002–T04002. ISSN: 1748-0221. DOI: `10.1088/1748-0221/9/04/t04002`. URL: `http://dx.doi.org/10.1088/1748-0221/9/04/T04002`.

[Moe14] Michael Moe. “The First Direct Observation of Double-Beta Decay”. In: *Annual Review of Nuclear and Particle Science* 64 (Oct. 2014), pp. 247–267. DOI: `10.1146/annurev-nucl-102313-025411`.

[Mon] Alissa Monte. *HydroX: Hydrogen Doped LXe.* New Directions in the Search for Light Dark Matter Particles. Fermilab, UChicago. URL: `https://indico.fnal.gov/event/20385/contributions/57350/attachments/35924/43780/NDitSfLSMP_HydroX.pdf`.

[Mor+16] A. Morozov et al. “ANTS2 package: simulation and experimental data processing for Anger camera type detectors”. In: *Journal of Instrumentation* 11.04 (Apr. 2016), P04022–P04022. ISSN: 1748-0221. DOI: `10.1088/1748-0221/11/04/p04022`. URL: `http://dx.doi.org/10.1088/1748-0221/11/04/P04022`.

[Mou+17] B. J. Mount et al. *LUX-ZEPLIN (LZ) Technical Design Report.* 2017. arXiv: `1703.09144 [physics.ins-det]`.

[Mys18] Jordan Myslik. *LEGEND: The Large Enriched Germanium Experiment for Neutrinoless Double-Beta Decay.* 2018. arXiv: `1810.00849 [physics.ins-det]`.

[Nev+17] F. Neves et al. “Measurement of the absolute reflectance of polytetrafluoroethylene (PTFE) immersed in liquid xenon”. In: *Journal of Instrumentation* 12.01 (Jan. 2017), P01017–P01017. DOI: `10.1088/1748-0221/12/01/p01017`. URL: `https://doi.org/10.1088/1748-0221/12/01/p01017`.

[Njo+20] O. Njoya et al. “Measurements of electron transport in liquid and gas Xenon using a laser-driven photocathode”. In: *Nuclear Instruments and Methods in Physics Research Section A: Accelerators, Spectrometers, Detectors and Associated Equipment* 972 (2020), p. 163965. ISSN: 0168-9002. DOI: `https://doi.org/10.1016/j.nima.2020.163965`. URL: `https://www.sciencedirect.com/science/article/pii/S0168900220304320`.

[Nut+20] Irene Nutini et al. "The CUORE Detector and Results". In: *Journal of Low Temperature Physics* 199 (Apr. 2020). DOI: `10.1007/s10909-020-02402-9`.

[Nyg74] David R Nygren. "Proposal to investigate the feasibility of a novel concept in particle detection". In: *Lawrence Berkeley National Laboratory internal report, Berkeley, CA, USA* (1974).

[OHa21] Ciaran A. J. O'Hare. "New Definition of the Neutrino Floor for Direct Dark Matter Searches". In: *Physical Review Letters* 127.25 (Dec. 2021). DOI: `10.1103/physrevlett.127.251802`. URL: `https://doi.org/10.1103%2Fphysrevlett.127.251802`.

[OO16] Igor Ostrovskiy and Kevin O'Sullivan. "Search for neutrinoless double beta decay". In: *Modern Physics Letters A* 31.18, 1630017 (June 2016). ISSN: 1793-6632. DOI: `10.1142/s0217732316300172`. URL: `http://dx.doi.org/10.1142/S0217732316300172`.

[Org12] Giovanni Organtini. "Unveiling the Higgs mechanism to students". In: *European Journal of Physics* 33.5 (July 2012), pp. 1397–1406. DOI: `10.1088/0143-0807/33/5/1397`. URL: `https://doi.org/10.1088%2F0143-0807%2F33%2F5%2F1397`.

[Pal+15] Nathalie Palanque-Delabrouille et al. "Neutrino masses and cosmology with Lyman-alpha forest power spectrum". In: 2015.11 (Nov. 2015), pp. 011–011. DOI: `10.1088/1475-7516/2015/11/011`. URL: `https://doi.org/10.1088/1475-7516/2015/11/011`.

[Par+18] B. López Paredes et al. "Response of photomultiplier tubes to xenon scintillation light". In: *Astroparticle Physics* 102 (Nov. 2018), pp. 56–66. DOI: `10.1016/j.astropartphys.2018.04.006`. URL: `https://doi.org/10.1016%2Fj.astropartphys.2018.04.006`.

[Pat19] Josephine Paton. *Neutrinoless Double Beta Decay in the SNO+ Experiment.* 2019. arXiv: `1904.01418 [hep-ex]`.

[Per22a] Guilherme Pereira. *Energy resolution of the LZ detector for High-Energy Electronic Recoils.* 5th XeSAT conference. Coimbra: University of Coimbra, 2022. URL: `https://indico.in2p3.fr/event/20879/contributions/109640/attachments/70740/100409/GuilhermePereira_%20Energy%20resolution%20of%20LZ%20detector%20for%20High%20Energy%20Electronic%20Recoils.pdf`.

[Per22b] Ricado Peres. *SiPM readout of Xenoscope.* 5th XeSAT Conference. Coimbra: University of Zurich, 2022. URL: `https://indico.in2p3.fr/event/20879/contributions/109398/attachments/70762/100440/SiPM_readout_of_Xenoscope_v2.pdf`.

[Pet16] S.T. Petcov. "NEUTRINO MASSES, MIXING AND OSCILLATIONS". In: *Non-Accelerator Astroparticle Physics.* 2016. Chap. 14, pp. 21–40. DOI: `10.1142/9789812701893_0002`. eprint: `https://www.worldscientific.com/doi/pdf/10.1142/9789812701893_0002`. URL: `https://www.worldscientific.com/doi/abs/10.1142/9789812701893_0002`.

[Pho17] Hamamatsu Photonics. *VUV-MPPC 4th generation (VUV4).* Product Flyer. 2017. URL: `2017.03.31_KSX-I50133-E_VUV-MPPC(VUV4)`.

[Pho21] Hamamatsu Photonics. *Photomultiplier Tube: R8520-406/R8520-506.* Product Flyer. 2021. URL: `https://www.hamamatsu.com/content/dam/hamamatsu-photonics/sites/documents/99_SALES_LIBRARY/etd/R8520-406_TPMH1342E.pdf`.

[Pov+08] B. Povh et al. *Particles and Nuclei. An Introduction to the Physical Concepts.* Ed. by Springer. Trans. by Martin Lavelle. 6th edition. Springer, 2008. ISBN: 978-3-540-79367-0.

[Rig18] Catherine Rigollet. *Fusion in Stars.* Lecture Slides on Nuclear Energy. Groningen, 2018.

[ROB13] R. G. H. ROBERTSON. “EMPIRICAL SURVEY OF NEUTRINOLESS DOUBLE BETA DECAY MATRIX ELEMENTS”. In: *Modern Physics Letters A* 28.08 (Mar. 2013), p. 1350021. ISSN: 1793-6632. DOI: `10.1142/s0217732313500211`. URL: `http://dx.doi.org/10.1142/S0217732313500211`.

[Rub77] C. Rubbia. “The Liquid Argon Time Projection Chamber: A New Concept for Neutrino Detectors”. In: (May 1977).

[Saa13] Ruben Saakyan. “Two-Neutrino Double-Beta Decay”. In: *Annual Review of Nuclear and Particle Science* 63.1 (2013), pp. 503–529. DOI: `10.1146/annurev-nucl-102711-094904`. eprint: `https://doi.org/10.1146/annurev-nucl-102711-094904`. URL: `https://doi.org/10.1146/annurev-nucl-102711-094904`.

[Sch12] Kate Scholberg. “Supernova Neutrino Detection”. In: *Annual Review of Nuclear and Particle Science* 62.1 (2012), pp. 81–103. DOI: `10.1146/annurev-nucl-102711-095006`. eprint: `https://doi.org/10.1146/annurev-nucl-102711-095006`. URL: `https://doi.org/10.1146/annurev-nucl-102711-095006`.

[SD11] Peter Sorensen and Carl Eric Dahl. “Nuclear recoil energy scale in liquid xenon with application to the direct detection of dark matter”. In: *Phys. Rev. D* 83 (6 Mar. 2011), p. 063501. DOI: `10.1103/PhysRevD.83.063501`. URL: `https://link.aps.org/doi/10.1103/PhysRevD.83.063501`.

[Sol+04] V.N Solovov et al. “Measurement of the refractive index and attenuation length of liquid xenon for its scintillation light”. In: *Nuclear Instruments and Methods in Physics Research Section A: Accelerators, Spectrometers, Detectors and Associated Equipment* 516.2 (2004), pp. 462–474. ISSN: 0168-9002. DOI: `https://doi.org/10.1016/j.nima.2003.08.117`. URL: `https://www.sciencedirect.com/science/article/pii/S0168900203024331`.

[Sol+12] V. N. Solovov et al. “Position Reconstruction in a Dual Phase Xenon Scintillation Detector”. In: *IEEE Transactions on Nuclear Science* 59.6 (2012), pp. 3286–3293. DOI: `10.1109/TNS.2012.2221742`.

[Sol21] Andrey Solovov. “Exploration of Machine learning tecniques for discrimination of neutrinoless double beta decay of 136Xe”. University of Coimbra, 2021.

[Szy+11] M Szydagis et al. “NEST: a comprehensive model for scintillation yield in liquid xenon”. In: *Journal of Instrumentation* 6.10 (Oct. 2011), P10002–P10002. ISSN: 1748-0221. DOI: `10.1088/1748-0221/6/10/p10002`. URL: `http://dx.doi.org/10.1088/1748-0221/6/10/P10002`.

[Szy+18] M. Szydagis et al. *Noble Element Simulation Technique v2.0.* Version v2.0.0. July 2018. DOI: `10.5281/zenodo.1314669`. URL: `https://doi.org/10.5281/zenodo.1314669`.

[Tay20] Robert Taylor. “Neutrinoless Double Beta Decay in Dual-phase Xenon Time Projection Chambers: LUX, LZ and Prospects for G3”. PhD Thesis. Imperial College of London, 2020. Chap. 4.

[Tez+04] C. Tezuka et al. “Electron diffusion and scintillation in xenon doped with hydrogen for high-pressure xenon time projection chamber”. In: vol. 2. Nov. 2004, 1157–1159 Vol. 2. ISBN: 0-7803-8700-7. DOI: `10.1109/NSSMIC.2004.1462407`.

[Wie+04] H. Wieczorek et al. “Analytical model for pixellated SPECT detector concepts”. In: vol. 4. Nov. 2004, 2584–2588 Vol. 4. ISBN: 0-7803-8700-7. DOI: `10.1109/NSSMIC.2004.1462781`.

[Wie+05] H. Wieczorek et al. “Collimator spatial resolution”. In: vol. 3. Nov. 2005, 5 pp. ISBN: 0-7803-9221-3. DOI: `10.1109/NSSMIC.2005.1596651`.

[Wri07] Edward Wright. *Sachs-Wolfe Effect.* 2007. URL: `https://www.astro.ucla.edu/~wright/Sachs-Wolfe.html`.

[Wu+57] C. S. Wu et al. “Experimental Test of Parity Conservation in Beta Decay”. In: *Phys. Rev.* 105 (4 Feb. 1957), pp. 1413–1415. DOI: `10.1103/PhysRev.105.1413`. URL: `https://link.aps.org/doi/10.1103/PhysRev.105.1413`.

[Xu+14] Yihong Xu et al. “Determination of plutonium isotopes (238Pu, 239Pu, 240Pu, 241Pu) in environmental samples using radiochemical separation combined with radiometric and mass spectrometric measurements”. In: *Talanta* 119 (2014), pp. 590–595. ISSN: 0039-9140. DOI: `https://doi.org/10.1016/j.talanta.2013.11.061`. URL: `https://www.sciencedirect.com/science/article/pii/S0039914013009491`.

[Zen22] Zen Collaboration. *First Search for the Majorana Nature of Neutrinos in the Inverted Mass Ordering Region with KamLAND-Zen.* 2022. DOI: `10.48550/ARXIV.2203.02139`. URL: `https://arxiv.org/abs/2203.02139`.

Appendix

Solar Reaction Chain

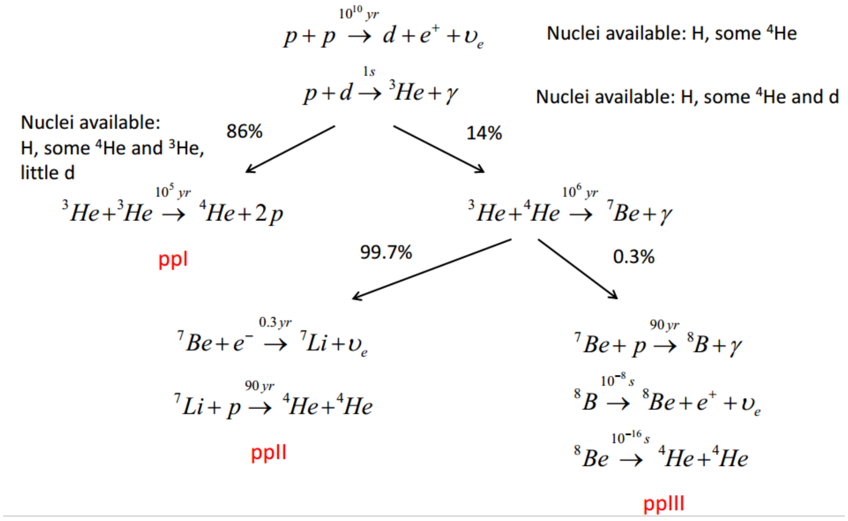

Summary of the *pp chain* reaction [Rig18].

Decay Schemes

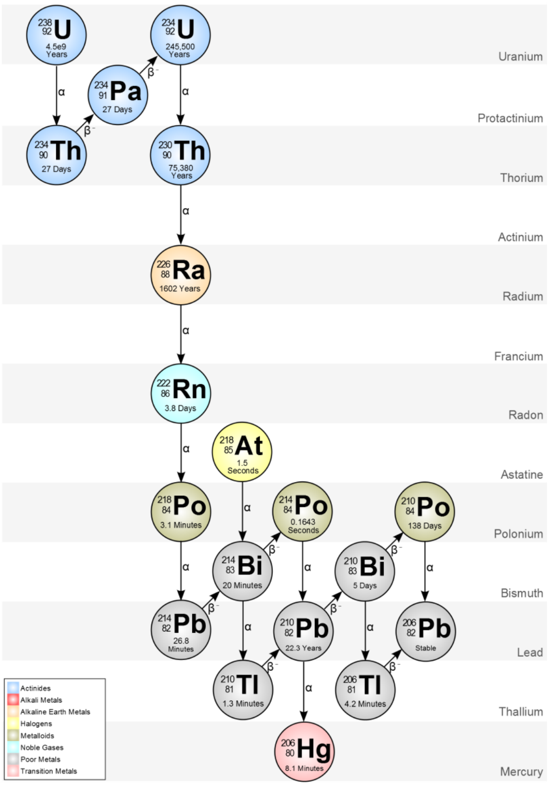

Decay chain of ^{238}U [Edu11].

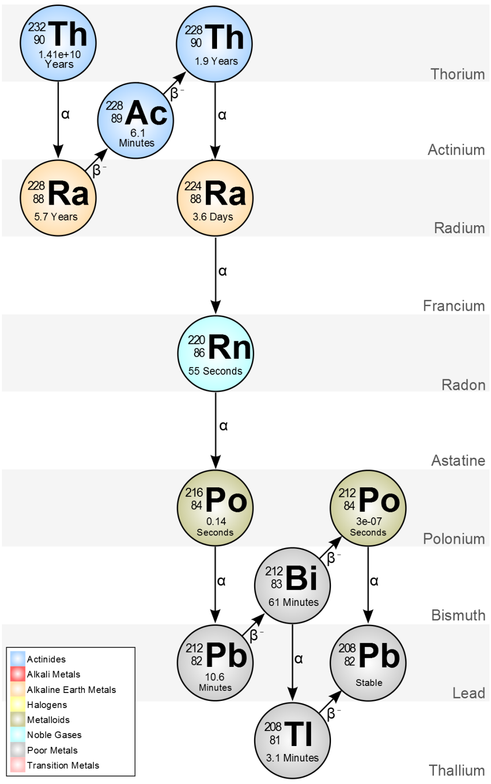

Decay chain of ^{232}Th [Edu11].

The following pages contain the **Code Flowchart** from Chapter 7.

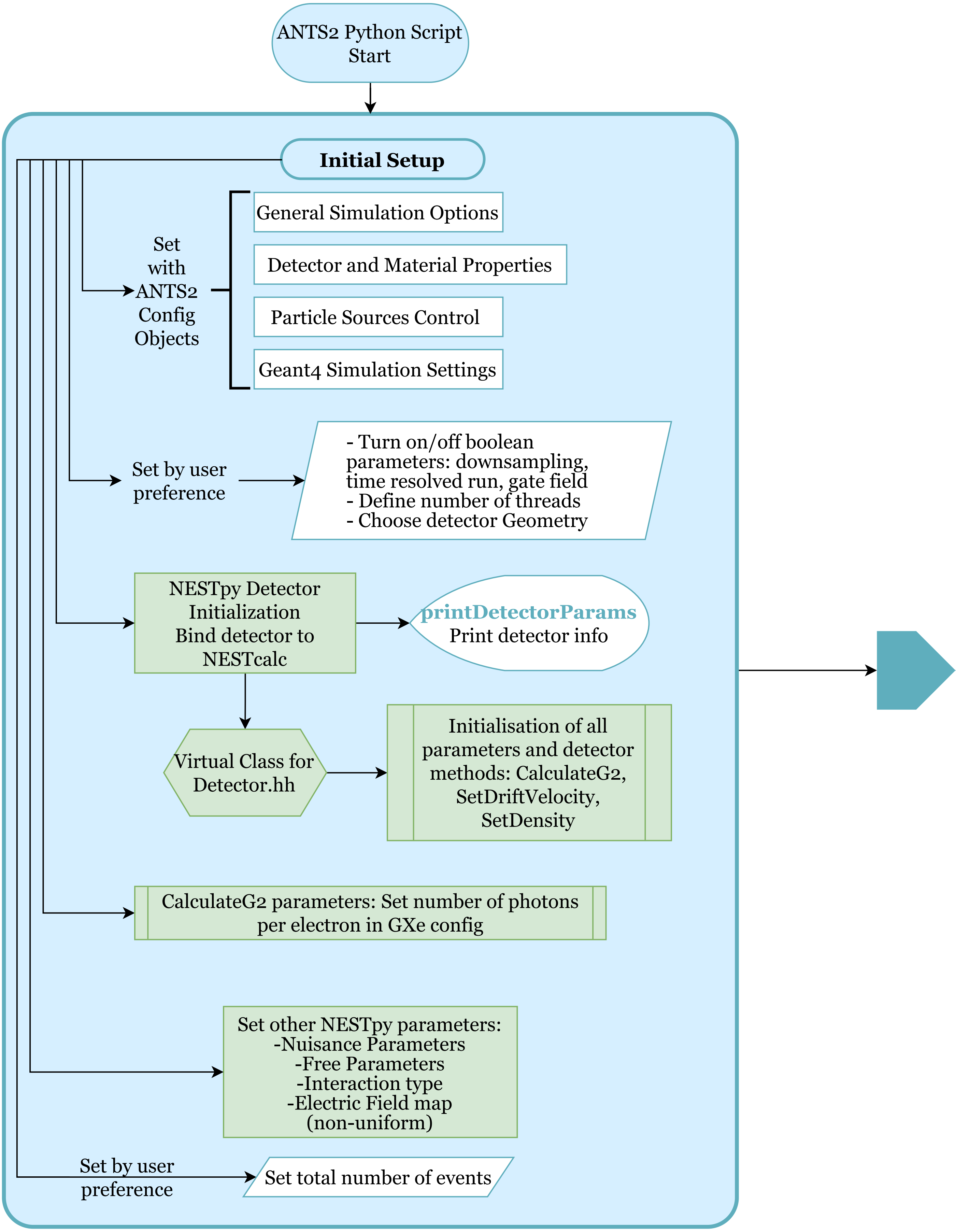
ANTS2 Python Script Start
Initial Setup
Set with ANTS2 Config Objects
General Simulation Options
Detector and Material Properties
Particle Sources Control
Geant4 Simulation Settings
Set by user preference
- Turn on/off boolean parameters: downsampling, time resolved run, gate field
- Define number of threads
- Choose detector Geometry
NESTpy Detector Initialization Bind detector to NESTcalc
printDetectorParams
Print detector info
Virtual Class for Detector.hh
Initialisation of all parameters and detector methods: CalculateG2, SetDriftVelocity, SetDensity
CalculateG2 parameters: Set number of photons per electron in GXe config
Set other NESTpy parameters:
-Nuisance Parameters
-Free Parameters
-Interaction type
-Electric Field map (non-uniform)
Set by user preference
Set total number of events

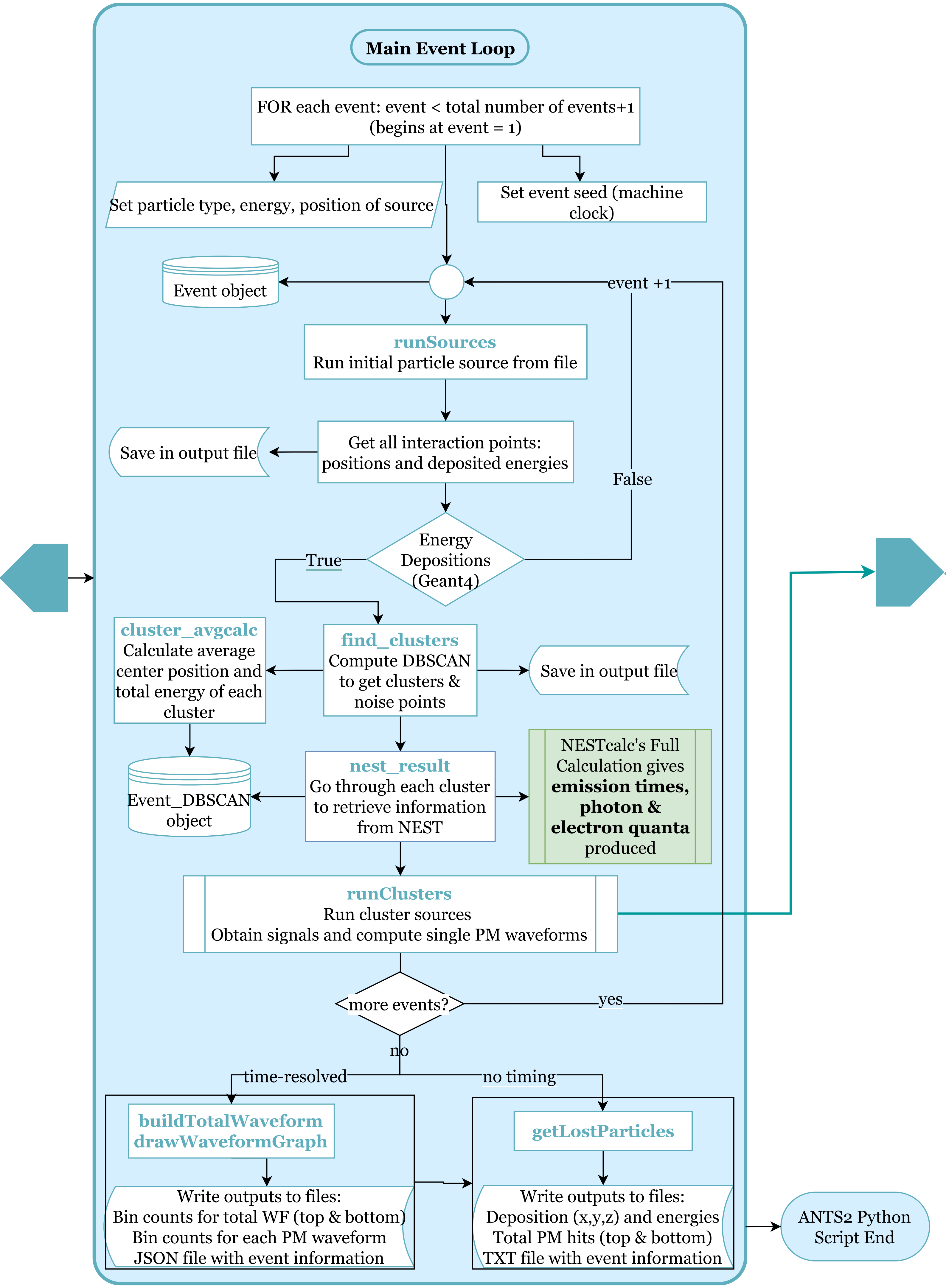
Main Event Loop
FOR each event: event < total number of events+1
(begins at event = 1)
Set particle type, energy, position of source
Set event seed (machine clock)
Event object
event +1
runSources
Run initial particle source from file
Save in output file
Get all interaction points: positions and deposited energies
False
True
Energy Depositions (Geant4)
cluster_avgcalc
Calculate average center position and total energy of each cluster
find_clusters
Compute DBSCAN to get clusters & noise points
Save in output file
Event_DBSCAN object
nest_result
Go through each cluster to retrieve information from NEST
NESTcalc's Full Calculation gives emission times, photon & electron quanta produced
runClusters
Run cluster sources
Obtain signals and compute single PM waveforms
more events?
yes
no
time-resolved
no timing
buildTotalWaveform
drawWaveformGraph
Write outputs to files:
Bin counts for total WF (top & bottom)
Bin counts for each PM waveform
JSON file with event information
getLostParticles
Write outputs to files:
Deposition (x,y,z) and energies
Total PM hits (top & bottom)
TXT file with event information
ANTS2 Python Script End

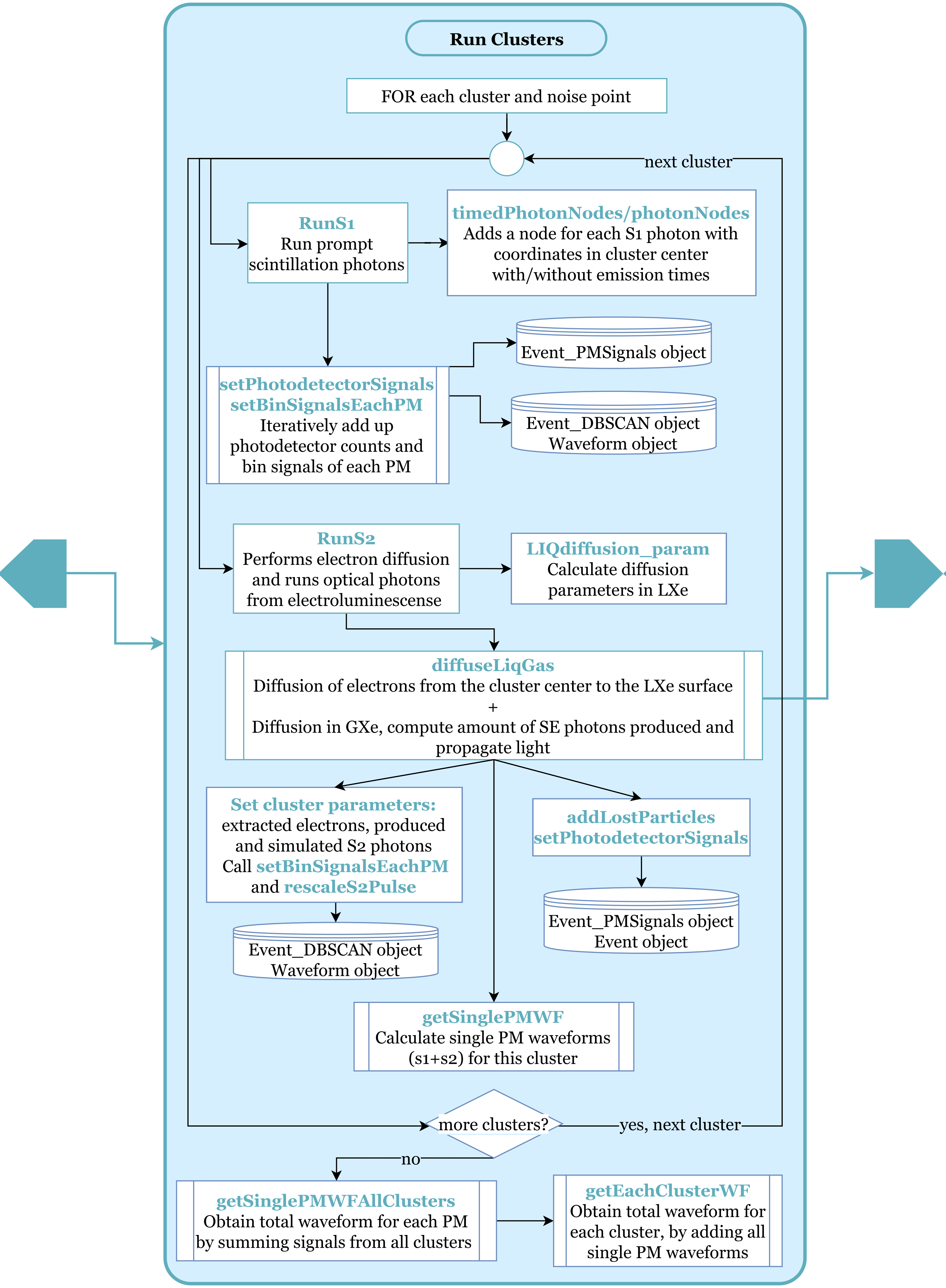
Run Clusters
FOR each cluster and noise point
next cluster
RunS1
Run prompt scintillation photons
timedPhotonNodes/photonNodes
Adds a node for each S1 photon with coordinates in cluster center with/without emission times
Event_PMSignals object
setPhotodetectorSignals
setBinSignalsEachPM
Iteratively add up photodetector counts and bin signals of each PM
Event_DBSCAN object
Waveform object
RunS2
Performs electron diffusion and runs optical photons from electroluminescense
LIQdiffusion_param
Calculate diffusion parameters in LXe
diffuseLiqGas
Diffusion of electrons from the cluster center to the LXe surface
+
Diffusion in GXe, compute amount of SE photons produced and propagate light
Set cluster parameters:
extracted electrons, produced and simulated S2 photons
Call setBinSignalsEachPM and rescaleS2Pulse
Event_DBSCAN object
Waveform object
addLostParticles
setPhotodetectorSignals
Event_PMSignals object
Event object
getSinglePMWF
Calculate single PM waveforms (s1+s2) for this cluster
more clusters?
yes, next cluster
no
getSinglePMWFAllClusters
Obtain total waveform for each PM by summing signals from all clusters
getEachClusterWF
Obtain total waveform for each cluster, by adding all single PM waveforms

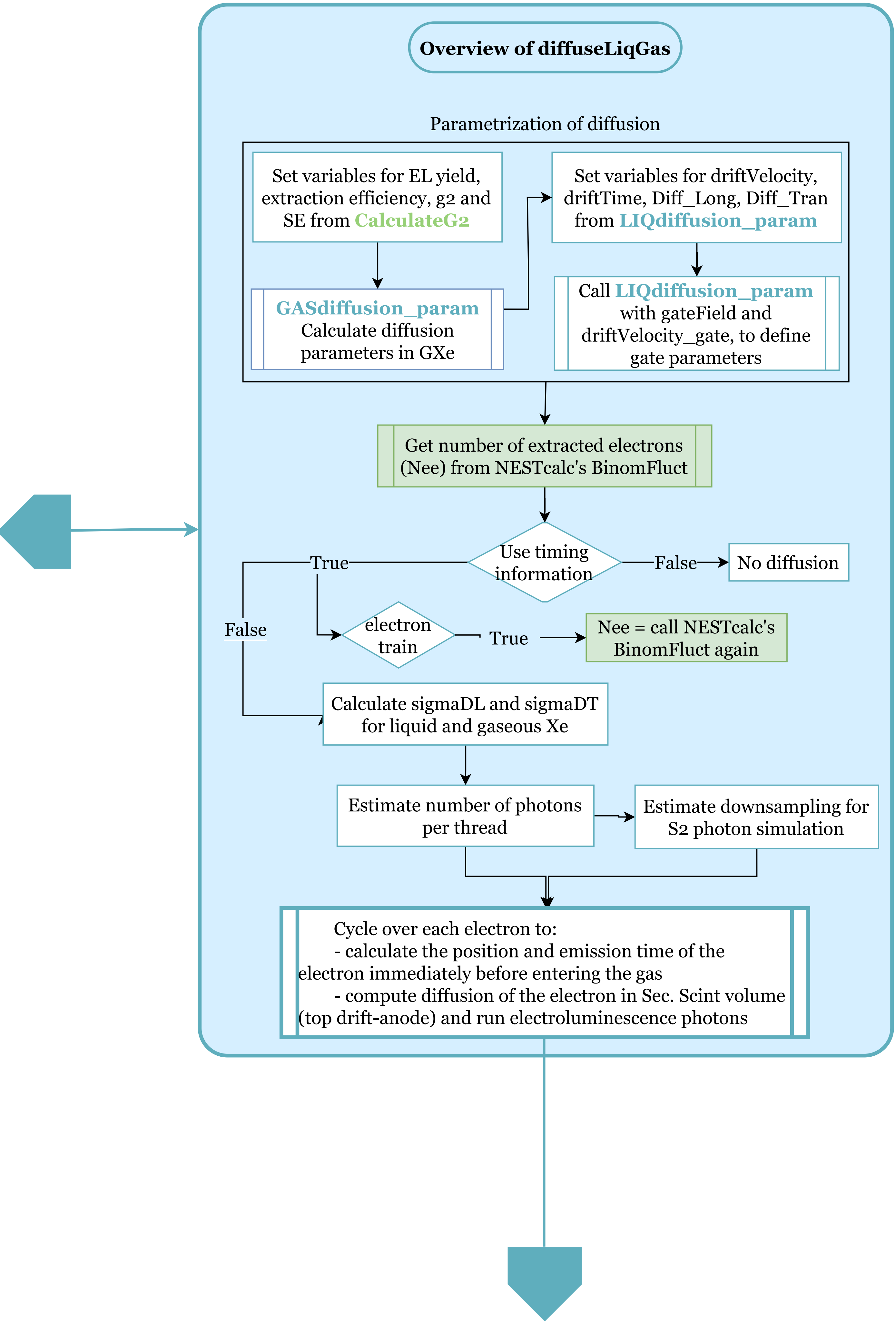
Overview of diffuseLiqGas
Parametrization of diffusion
Set variables for EL yield, extraction efficiency, g2 and SE from CalculateG2
GASdiffusion_param Calculate diffusion parameters in GXe
Set variables for driftVelocity, driftTime, Diff_Long, Diff_Tran from LIQdiffusion_param
Call LIQdiffusion_param with gateField and driftVelocity_gate, to define gate parameters
Get number of extracted electrons (Nee) from NESTcalc's BinomFluct
Use timing information
False
No diffusion
True
False
electron train
True
Nee = call NESTcalc's BinomFluct again
Calculate sigmaDL and sigmaDT for liquid and gaseous Xe
Estimate number of photons per thread
Estimate downsampling for S2 photon simulation
Cycle over each electron to:
- calculate the position and emission time of the electron immediately before entering the gas
- compute diffusion of the electron in Sec. Scint volume (top drift-anode) and run electroluminescence photons

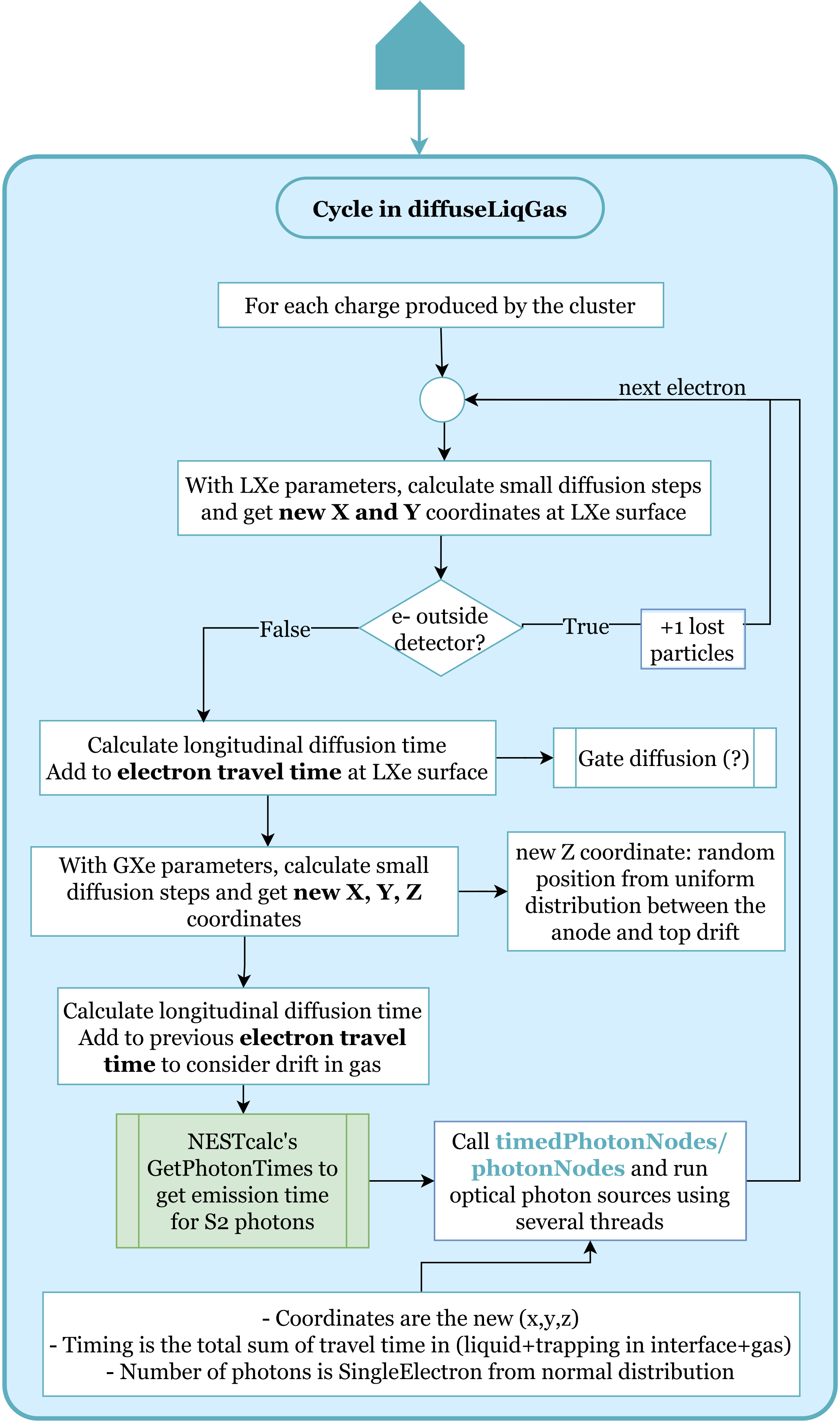
Cycle in diffuseLiqGas
For each charge produced by the cluster
next electron
With LXe parameters, calculate small diffusion steps and get new X and Y coordinates at LXe surface
e- outside detector?
False
True
+1 lost particles
Calculate longitudinal diffusion time Add to electron travel time at LXe surface
Gate diffusion (?)
With GXe parameters, calculate small diffusion steps and get new X, Y, Z coordinates
new Z coordinate: random position from uniform distribution between the anode and top drift
Calculate longitudinal diffusion time Add to previous electron travel time to consider drift in gas
NESTcalc's GetPhotonTimes to get emission time for S2 photons
Call timedPhotonNodes/ photonNodes and run optical photon sources using several threads
- Coordinates are the new (x,y,z)
- Timing is the total sum of travel time in (liquid+trapping in interface+gas)
- Number of photons is SingleElectron from normal distribution